AD NUMBER

ADB017206

LIMITATION CHANGES

TO:

Approved for public release; distribution is unlimited. Document partially illegible.

FROM:

Distribution authorized to U.S. Gov't. agencies only; Test and Evaluation; JAN 1977. Other requests shall be referred to Air Force Avioincs Laboratory, AFAL/RWI, Wright-Patterson AFB, OH 45433. Document partially illegible.

AUTHORITY

afwal ltr, 8 oct 1981

AFAL-TR-76-214
Volume II

SHIP IDENTIFICATION STUDY

Volume II. Appendix A. ATMOSPHERIC EFFECTS AT OPTICAL WAVELENGTHS

SYSTEMS RESEARCH LABORATORIES, INC.
2800 INDIAN RIPPLE ROAD
DAYTON, OH 45440

JANUARY 1977

TECHNICAL REPORT AFAL-TR-76-214, Volume II
FINAL REPORT FOR PERIOD JUNE 1975 - MARCH 1976

AIR FORCE AVIONICS LABORATORY
AIR FORCE WRIGHT AERONAUTICAL LABORATORIES
AIR FORCE SYSTEMS COMMAND
WRIGHT-PATTERSON AIR FORCE BASE, OHIO 45433

NOTICE

When Government drawings, specifications, or other data are used for any purpose other than in connection with a definitely related Government procurement operation, the United States Government thereby incurs no responsibility nor any obligation whatsoever; and the fact that the government may have formulated, furnished, or in any way supplied the said drawings, specifications, or other data, is not to be regarded by implication or otherwise as in any manner licensing the holder or any other person or corporation, or conveying any rights or permission to manufacture, use, or sell any patented invention that may in any way be related thereto.

This technical report has been reviewed and is approved for publication.

William L. Harmon
Signature
Name
Project Engineer/Scientist

Ronald M. Hubbard
Signature
Name
Supervisor

FOR THE COMMANDER

Harold E. Calhoun
Signature and Title

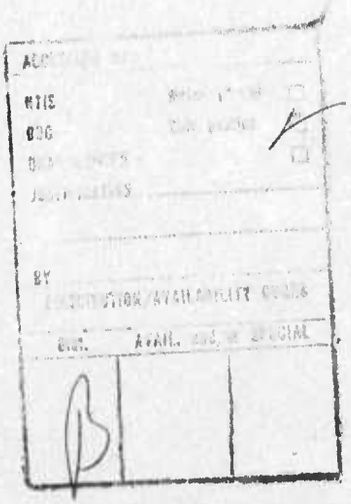

Copies of this report should not be returned unless return is required by security considerations, contractual obligations, or notice on a specific document.

AIR FORCE - 7 MARCH 77 - 100

SECURITY CLASSIFICATION OF THIS PAGE *(When Data Entered)*

REPORT DOCUMENTATION PAGE

READ INSTRUCTIONS BEFORE COMPLETING FORM

1. REPORT NUMBER: AFAL-TR-76- 214, Volume II

2. GOVT ACCESSION NO.

3. RECIPIENT'S CATALOG NUMBER

4. TITLE (and Subtitle): SHIP IDENTIFICATION STUDY, Volume II. Appendix A. Atmospheric Effects at Optical Wavelengths.

5. TYPE OF REPORT & PERIOD COVERED: Final report, covering period 23 June 75 — 2 March 76.

6. PERFORMING ORG. REPORT NUMBER: 6870

7. AUTHOR(s): E. F. Starr, Jr., Ira H. Bowker, Frank X. Jeskie, George A. Whiteside.

8. CONTRACT OR GRANT NUMBER(s): F33615-75-C-1260

9. PERFORMING ORGANIZATION NAME AND ADDRESS: Systems Research Laboratories, Inc., 2800 Indian Ripple Road, Dayton, Ohio 45440

10. PROGRAM ELEMENT, PROJECT, TASK AREA & WORK UNIT NUMBERS: Project 2004, Work Unit 20040609

11. CONTROLLING OFFICE NAME AND ADDRESS: Air Force Avionics Laborat-ry, AFAL/RWI, Wright-Patterson AFB, OH 45433

12. REPORT DATE: January 1977

13. NUMBER OF PAGES: 168

14. MONITORING AGENCY NAME & ADDRESS *(if different from Controlling Office)*: SRL-6870

15. SECURITY CLASS. (of this report): UNCLASSIFIED

15a. DECLASSIFICATION/DOWNGRADING SCHEDULE

16. DISTRIBUTION STATEMENT *(of this Report)*

Distribution limited to US Government Agencies only; test and evaluation results reported; June 1975. Other requests for this document must be referred to AFAL/RWI, WPAFB, OH 45433.

17. DISTRIBUTION STATEMENT *(of the abstract entered in Block 20, if different from Report)*

18. SUPPLEMENTARY NOTES: TR-76-214-Vol-2

19. KEY WORDS *(Continue on reverse side if necessary and identify by block number)*

20. ABSTRACT *(Continue on reverse side if necessary and identify by block number)*

The study was composed of an investigation of means to detect a very broad range of discriminants which were developed by a study of the characteristics of the ships of the navies of the world. The study also encompassed a thorough investigation of atmospheric effects on the potential performance of the various sensor techniques. Detection techniques addressed include optical, passive EO, active EO, laser imaging, laser pattern recognition, microwave pattern recognition, microwave imaging, ELINT, photographic and acoustic. The EO techniques covered

over

DD FORM 1 JAN 73 1473 EDITION OF 1 NOV 65 IS OBSOLETE

SECURITY CLASSIFICATION OF THIS PAGE *(When Data Entered)*

340400

both the visible and IR spectrums. The hardware demonstration and development recommendations for each of the two time periods required (availability to SAC in two years and by 1985) is presented. Missions capability of recommended sensor systems for the scenario situations developed are presented.

FOREWORD

This ship identification study program was sponsored by the Air Force Avionics Laboratory, Wright-Patterson Air Force Base, Ohio. The work was performed by the Optronics Division of Systems Research Laboratories, Inc. (SRL), Dayton, Ohio, under Contract F33615-75-C-1260, SRL Project No. 6870. The contract monitor on behalf of the Avionics Laboratory was Mr. William Harmon (AFAL/RWI-1) and the work was in support of Work Unit 20040609.

This final report is submitted in three volumes. The first volume is an executive summary (an overview of the study effort), and the main technical report containing the details of the study. The second volume, Appendix A, is a compilation of the atmospheric calculations conducted for this effort. The third volume, Appendix B, is a collection of the subcontractor reports.

The research reported herein was initiated in June 1975 and completed in June 1976.

The author of this report gratefully acknowledges the considerable contributions of Mr. I. Bowker, Mr. J. Fraggiotti, Mr. H. Iffland, Mr. F. Jeskie, Dr. G. Little, Mr. J. Johnson, and Mr. G. Whiteside, the principal SRL engineers assigned to the program, and to Mr. J. Doctor, programmer, and Ms. Sharon Cox, operator for the computer calculations completed in support of this effort. The contributions of Mr. William Harmon, AFAL/RWI, to this program are also acknowledged.

This report was submitted by the author in September 1976.

TABLE OF CONTENTS

Vol. II. Appendix A. Atmospheric Effects at Optical Wavelengths (U)

LIST OF ILLUSTRATIONS

LIST OF ILLUSTRATIONS (cont.)

LIST OF ILLUSTRATIONS (cont.)

LIST OF TABLES

LIST OF TABLES (cont.)

Appendix A

ATMOSPHERIC EFFECTS AT OPTICAL WAVELENGTHS

Section A-1
INTRODUCTION

A substantial portion of the Ship Identification Study (SIS) effort was devoted to an investigation of atmospheric optical effects likely to be encountered in the long slant paths required for ship identification at acceptable stand-off ranges. Potentially troublesome atmospheric effects can occur to a laser beam utilized for illumination in an active system, and to reflected energy returned to the observation aircraft from the target area. (In some respects the significant effects for the illuminating beam are different from those for the returned energy.)

There were three principal reasons for the large effort expended in the investigation of atmospheric phenomena in the optical wavelength* region:

(1) It was anticipated that atmospheric phenomena would play a large role in determining the potential merits of the many candidate sensor concepts to be considered;

(2) Atmospheric molecular absorption coefficients for laser frequencies in a potentially attractive portion of the optical spectrum (3.5 to 4.0 micrometer) were not well-established, to the extent that any calculated estimate was considered suspect and controversial; and

(3) A potentially troublesome effect, optical turbulence (both ambient and aircraft-induced), was but poorly known and little understood for long air-to-ground slant paths.

It was known that the problems indicated by (2) and (3) above were subjects of rather intensive research at several laboratories. Researchers at those laboratories were consulted during the course of the study, and very significant advance unpublished results were thereby obtained for application to the SIS effort. Thus the findings of this report depended heavily upon

*As used herein, the term "optical wavelengths" encompasses electromagnetic waves having free-space wavelengths in the region from 0.3 to 15.0 micrometers.

information supplied by the Optical Physics Laboratory of the Air Force Cambridge Research Laboratories, the Optical Sciences Division of the Naval Research Laboratory, Air Force Weapons Laboratory divisions under the Advanced Radiation Technology Office, the Electro Science Laboratory of Ohio State University, and Science Applications Incorporated. (Information from the latter two organizations resulted from efforts sponsored by Defense Research Projects Agency under Rome Air Development Center contracts, and release of advance data from those efforts was arranged through RADC.) Our thanks to the many individuals involved who shared their expertise with us for this project.

References 1 through 10 of this appendix are formal published reports in the open literature which constitute an excellent starting point and package of data sources for beginning a study of atmospheric effects upon an electro-optical (EO) system. These references were so employed in the SIS effort. A few papers from technical journals also proved helpful, and these are listed. A characteristic of this study, however, is the large use that was made of advance unpublished data obtained from researchers in the field. Many of the listed references relate to such data. A bibliography is provided for sources not cited specifically.

As various aspects of the atmospheric transmission problem were investigated, draft papers were written to document the individual efforts. Sections A-3 through A-11 of this appendix consist essentially of those draft papers, with some revision and updating where appropriate.

A "66-kilometer slant path" is referred to throughout this appendix in the context of a nominal atmospheric path over which SIS must be applicable. This nominal slant path is defined in the sketch below.

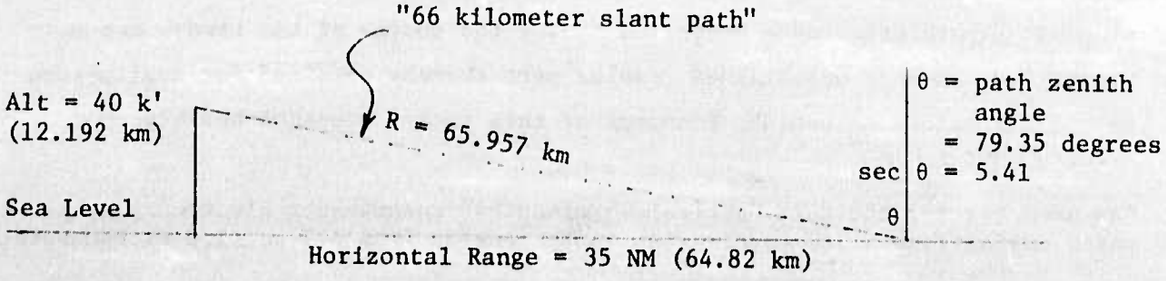

Section A-2
ATMOSPHERIC EFFECTS SYNOPSIS

GENERAL

Optical energy reflected or emitted from a target element and received by a sensor element at a distant location is affected in numerous ways by transmission through the atmosphere. Phenomena of major importance in the visible and/or IR wavelength regions are (1) attenuation of the target energy by path absorption and scattering out of the path, (2) scattering of extraneous background energy into the transmission path, (3) thermal radiance of the air mass in the path, and (4) optical turbulence within the path air mass. For a collimated or focused laser beam used for target illumination, (1) and (4) are the atmospheric phenomena of major importance.

Atmospheric absorption, scattering, and thermal radiance may be calculated approximately by the use of appropriate atmospheric models, together with mathematical models representing the atmospheric effects phenomena. SRL mainly uses models and coefficient tables developed by the Optical Physics Laboratory of AFCRL, as documented in several of the cited references. We also employ computer programs and data tables developed by AFCRL for computer calculation of spectral band atmospheric transmittance, manual calculation of which is tedious and costly.

The several scattering and absorption coefficients are strong functions of altitude, and this factor must be accounted for in an appropriate fashion in transmittance, path radiance, and optical turbulence calculations for air-to-surface slant paths.

The effects of some adverse weather conditions (e.g., rain and fog) are predictable to a limited extent if the relevant parameters (e.g., rainfall rate and extent) can be measured or estimated. A USAF Project RAND report, R-1523-PR (Ref. 11), provides information for calculating attenuation through rain, and the calculated results appear to be in reasonable agreement with

measured values. It should be noted that rain attenuation calculations based upon the approach in Middleton's classic text (Ref. 12) give totally erroneous results, and should not be used.

The McClatchey models (AFCRL) (Refs 1-8) do not take path optical turbulence into account, and this phenomenon must be accounted for separately to obtain quantitative estimates of the effects of this factor. The theoretical basis in this area is in a primitive state of development; however, quasi-empirical mathematical models are available for making engineering estimates, and such computed estimates appear to agree reasonably well with experimental results over a nominal range of atmospheric conditions and target-to-receiver geometries.

Extensive use was made of a recent RAND Corporation work (Ref. 13) in this area, supplemented by basic data from Tatarski (Ref. 14) and other researchers. Experimental data relating to ambient altitude variations and aircraft-induced turbulence were obtained from the AFWL Airborne Laser Laboratory program and applied to the SIS investigation. More data are expected to be available from AFWL during 1976.

VISIBLE AND NEAR-IR WAVELENGTH REGION

In this wavelength region, optical attenuation and path radiance are mainly attributable to scattering of energy by air molecules and by atmospheric haze caused by suspended dust, smoke and other foreign matter (collectively termed "aerosols").

At the shorter wavelengths, Rayleigh scattering (by air molecules) and Mie scattering (by atmospheric aerosols) are of somewhat comparable significance in the lower atmosphere on a relatively clear day. On a relatively hazy day, aerosol scattering greatly predominates and becomes the limiting factor in visible wavelength transmission. Aerosol absorption is marginally

significant (but is often ignored), while molecular absorption is negligible, except as noted in the following paragraph, and may be ignored for band calculations in the visible wavelength region.

Water vapor molecules are not important scatterers or absorbers of visible wavelengths; hence, visible transmittance is not affected significantly by atmospheric humidity. That situation changes at the red end of the visible band, however, with significant water vapor absorption starting at about 0.69 micrometer, as illustrated in Sets I and IV of the transmittance graphs in Section A-6. Those graphs show computer-calculated band transmittance over an SIS air-to-ground slant path, for the visible to near-IR wavelength region of 0.3 to 1.8 micrometers, for a wide range of atmospheric conditions.

With daylight illumination, path radiance at visible wavelengths consists mainly of sky background energy which is scattered into the sensor field of view (FOV). With artificial illumination in darkness, backscattered energy from the illuminator is the principal source of path radiance.

In this wavelength region optical turbulence can cause a substantial increase in the imaging point spread function, with a concomitant degradation in the image quality achievable in high-resolution photography and television. For active night-time systems employing laser illuminators, optical turbulence induces beam wander and beam spread into the collimated laser beam, effectively placing a minimum diameter limit upon the useful size (and associated intensity) of the beam. Optical turbulence effects vary over a wide range in the lower atmosphere, depending upon the thermal dynamics of the air and adjacent surfaces.

8-13 MICROMETER IR BAND

In this wavelength region optical attenuation is chiefly attributable to molecular absorption by carbon dioxide and water vapor, and path radiance is mainly due to thermal emission of the air mass in the transmission path. Absorption and scattering by atmospheric aerosols are of some significance

but are minor contributors to the total except under conditions of relatively heavy haze and/or low atmospheric temperature and water vapor content.

Under most atmospheric conditions the predominant factor influencing transmittance in this wavelength region is atmospheric water vapor content (absolute, not relative, humidity). Also, since water vapor absorption is strongly temperature dependent, the air temperature of the transmission path is a significant secondary factor. (A warm, humid atmosphere provides poorest transmittance.)

In this wavelength region optical turbulence appears to be much less significant than at visible wavelengths. Minor degradations in the imaging point spread function and illumination beam parameters may occur under conditions of moderate to strong turbulence.

3-5 MICROMETER IR BAND

In this wavelength region the atmosphere exhibits optical properties which are a composite of those previously cited for shorter and longer wavelength bands. Molecular and aerosol absorption and aerosol scattering are all significant in the attenuation equation, and both scattering and air mass thermal radiation should be considered in estimating path radiance. The effects of atmospheric optical turbulence upon imaging and laser beam transmission are significantly less than they are in the visible region, but somewhat greater than they are in the 8-13 micrometer band.

Portions of this band (in the vicinity of 2.2 and 3.8 micrometers) exhibit optimum optical transmission over a wide range of atmospheric variables. Optical energy in these wavelength regions penetrates atmospheric haze much better than shorter (e.g., visible) wavelengths, and is much less affected by atmospheric water vapor than longer wavelengths (e.g., the 8-13 micrometer IR region).

ATMOSPHERIC IMPACT UPON LASER BEAM ILLUMINATORS

Atmospheric attenuation directly decreases the illumination energy available in the target region. Atmospheric turbulence, whether aircraft-induced or ambient, breaks up the smoothly-varying spatial pattern of a collimated or focused beam and produces "scintillation" or rapidly varying intensity fluctuations within the beam. A random wandering of the beam about a central point, together with skew, astigmatism, and spreading, are additional beam distortions produced by optical turbulence. The end result is a spread, wandering, fluctuating beam whose average intensity on target can be much reduced compared to that predicted by diffraction limit theory for vacuum transmissions. This degradation in beam quality can be very significant over long atmospheric paths (particularly if sharp, efficient illuminating beams are desired) and must be accounted for in system design.

ATMOSPHERIC IMPACT UPON SENSORS

Atmospheric attenuation decreases the optical signal at the receiver, while path radiance introduces a background "noise" level. These factors directly influence the available contrast in a sensor (such as photographic film) which detects total energy content. In an electro-optical sensor (such as TV or FLIR) the path radiance can be largely suppressed by filtering, with mainly the video or ac component recorded or displayed. Scene contrast at the sensor (and signal-to-noise ratio) are then influenced mainly by atmospheric attenuation and sensor detectivity. Atmospheric turbulence over the transmission path can be expected to produce radiometer/photometer reading fluctuations and noticeable TV or FLIR image distortion and resolution degradation some significant percentage of the time.

SOME OBSERVATIONS ABOUT CALCULATION ACCURACIES AND SCALING

The molecular scattering coefficient, σ_m, exhibits a λ^{-4} dependence upon wavelength, and the coefficient scales linearly with the number of molecules in the path (and hence approximately with air density). Thus attenuation attributable to molecular scattering is easily and accurately calculable.

For a given constituency of materials and particle sizes making up an atmospheric aerosol model, the aerosol scattering coefficient, σ_a, and aerosol absorption coefficient, k_a, scale linearly with the number of particles in the path, and the variation with wavelength is reasonably well behaved. Hence, aerosol scattering and attenuation are easily calculated for model atmospheres for which σ_a and k_a tables have been established for a specified constituency and concentration of aerosol particles (including variation with altitude). The accuracy of particular atmospheric aerosol path transmittance estimates based upon such calculations is likely to be rather poor, however, because the actual aerosol constituency and distributions present are not likely to be known very well and hence will not fit the model very well. This factor is probably the principal source of error in estimating long path atmospheric effects at visible wavelengths.

The molecular absorption coefficient, k_m, is a complicated function of the total pressure, partial pressures, temperature, and specific constituency of the atmospheric gases in the transmission path, and of optical wavelength. Calculation of this factor in atmospheric transmittance is difficult and often the results are, at best, rough estimates. A published atmospheric absorption coefficient for one temperature, pressure, and constituency is not simply scalable to another set of conditions because individual air molecule constituents scale differently with partial pressure, total pressure, and temperature, while wavelength dependence is sharply structured and relatively unpredictable (except by machine computation). Figures A-1 through A-4 (from Ref. 15) illustrate the complexity of this factor in atmospheric transmittance. See also, typical high-resolution spectral transmittance curves in the 3.8 micrometer region (Figure A-22 of Section A-7) and in the 10.6 micrometer region (Figure A-31 of Section A-8).

It is because of the problem indicated in the foregoing paragraph, that a large body of spectral line absorptior coefficients and a band transmittance model (LOWTRAN) for a family of model atmospheres have been developed by AFCRL. Engineering estimates for practical application purposes can be

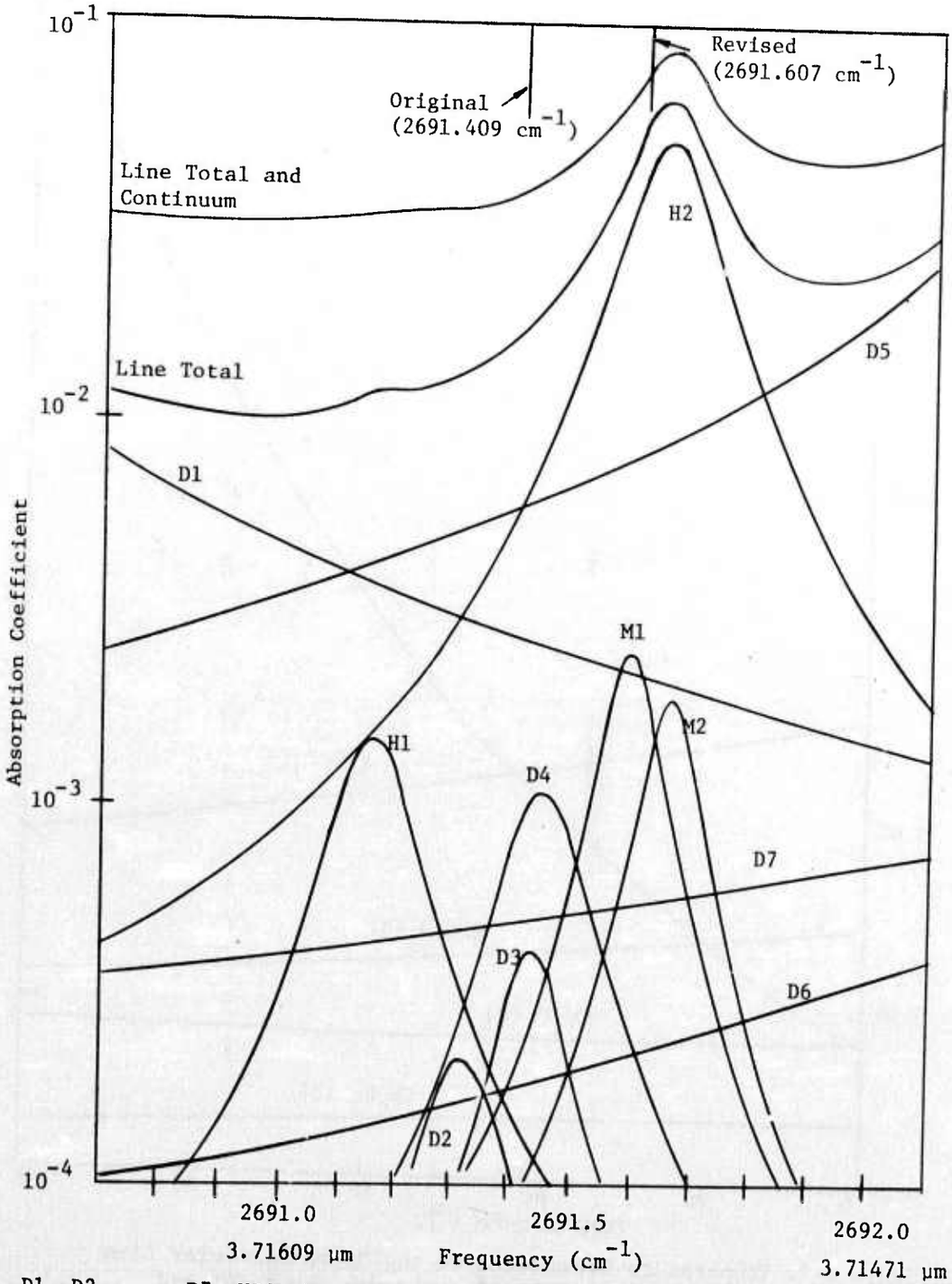

D1, D2 . . . D7: HDO absorption lines. H1, H2: H_2O absorption lines.
M1, M2: Methane absorption lines.

Figure A-1. Contributors to the Molecular Absorption of the $P_1(9)$ DF Line (Mid-Latitude Summer, Sea Level)

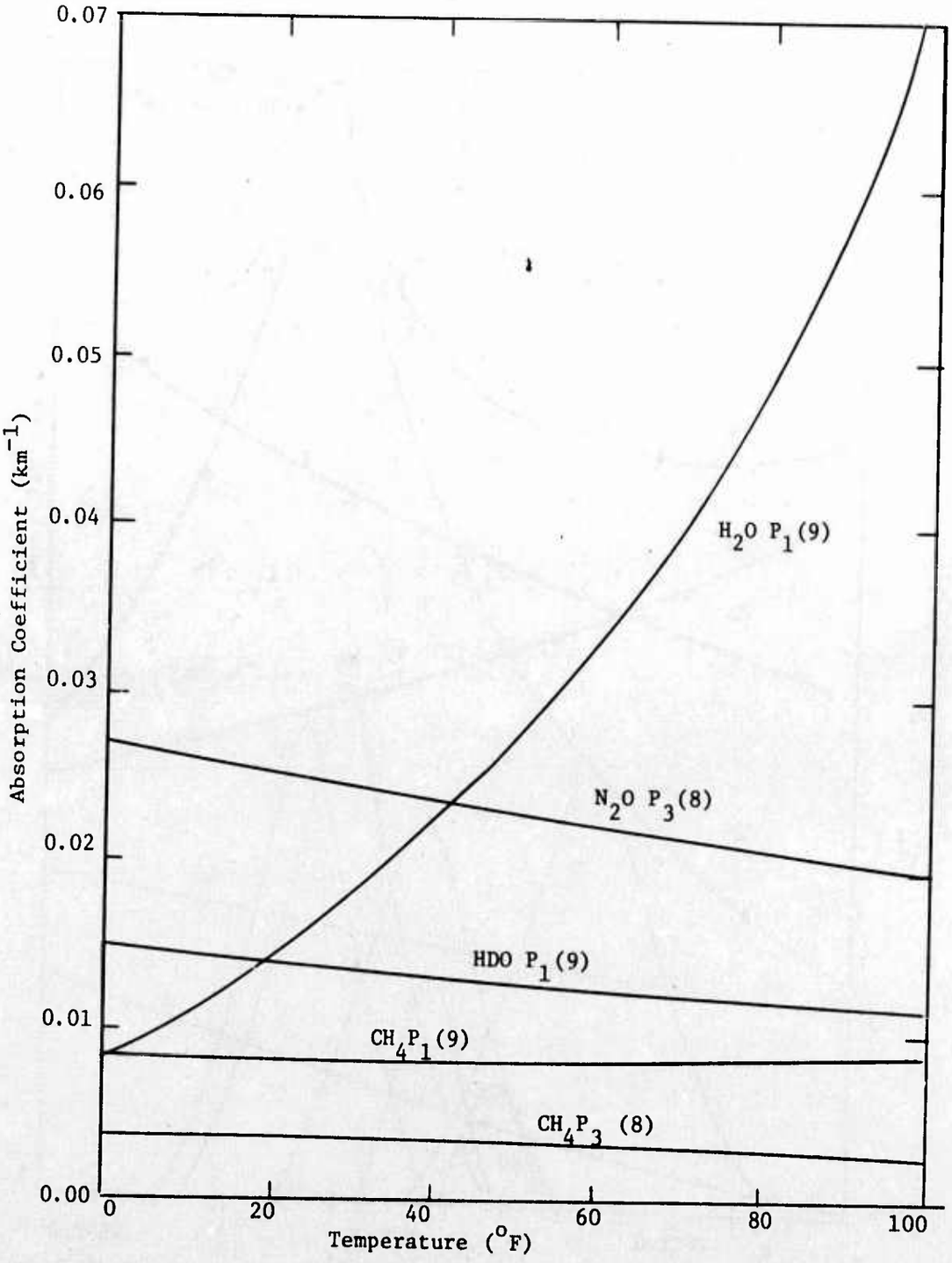

Figure A-2. Temperature Dependence of the Major Molecular Line Absorption Coefficient Contributors for the $P_1(9)$ and $P_3(8)$ DF Lines

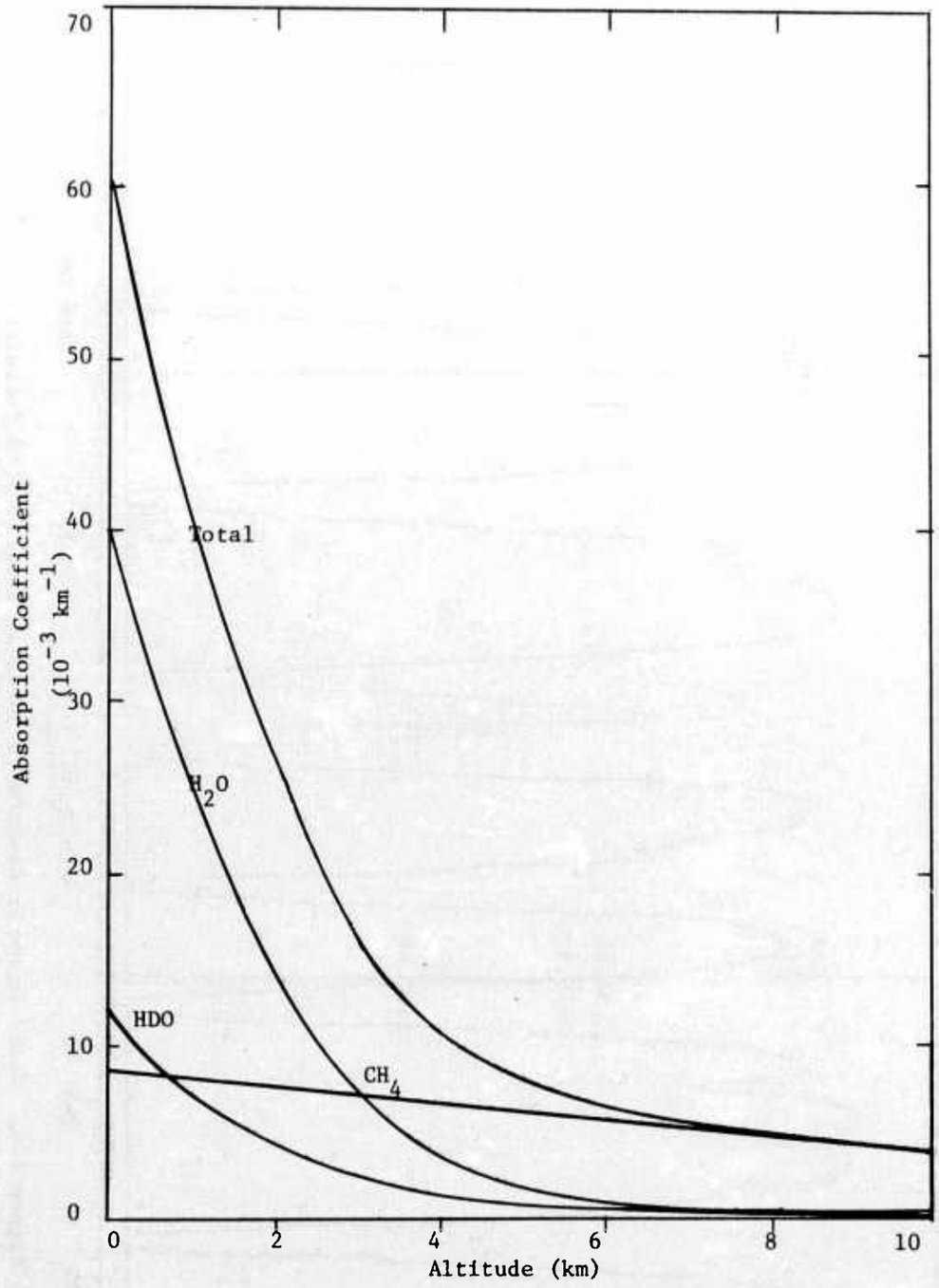

Figure A-3. Altitude Dependence of the Molecular Line Absorption Coefficient for the $P_1(9)$ DF Line Showing the Major Contributors (Mid-Latitude Summer)

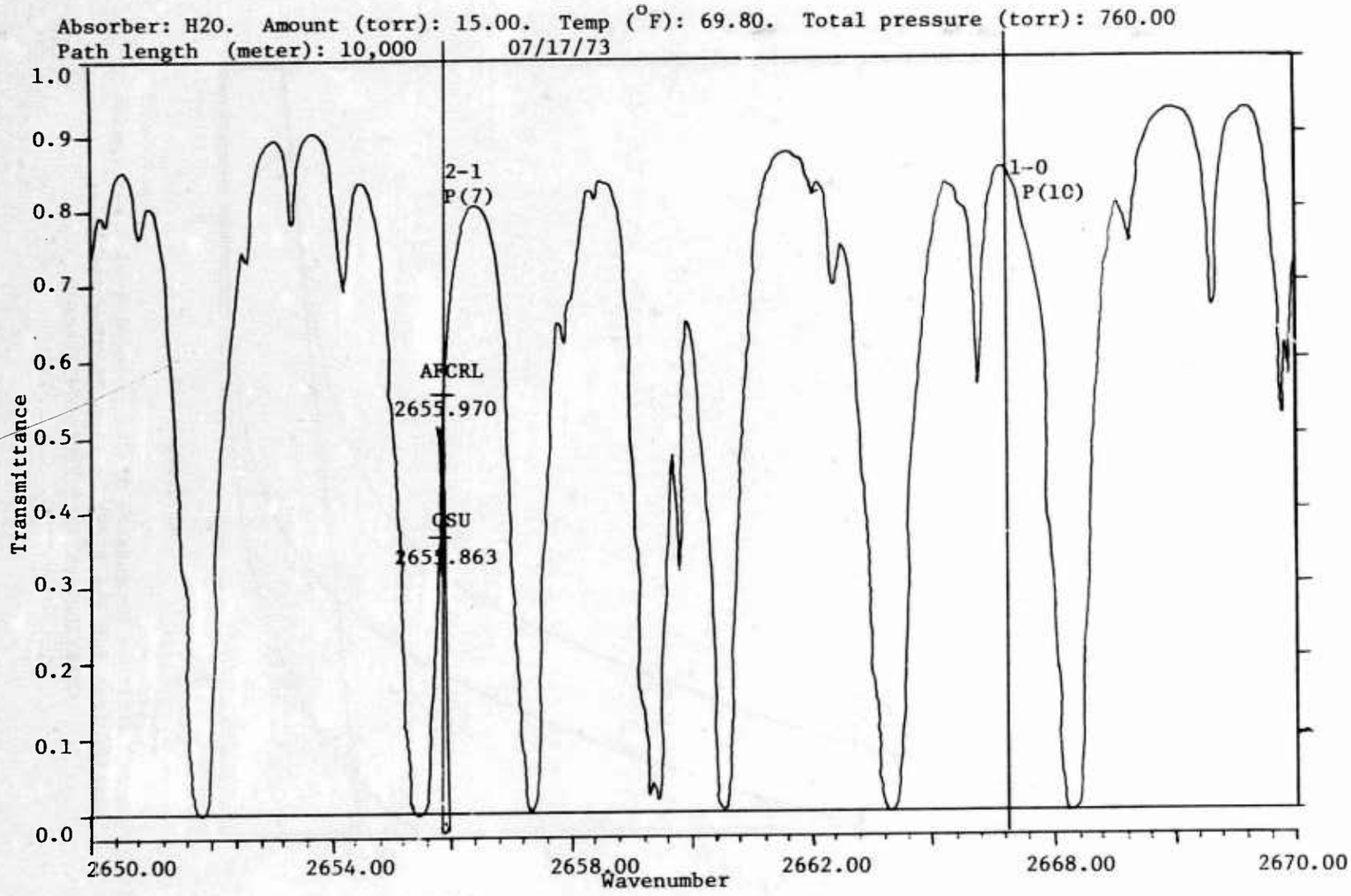

Figure A-4. Water Vapor Transmittance Spectral Structure in Vicinity of 3.76 μm, Showing Influence of Small Errors in Frequency

computed for "typical" atmospheric conditions over a rather wide range, by application of the AFCRL models and data (using either manual or machine computation).

DOPPLER SHIFT

The position of certain laser lines relative to high-resolution atmospheric transmittance spectra (e.g., Figure A-4) gave rise to this question: Is the doppler shift in frequency significant with respect to atmospheric attenuation of a laser beam transmitted from an airplane in flight?

A simple calculation showed that the maximum doppler shift (transmit direction at 0^{o} or 180^{o} to aircraft velocity) for an aircraft velocity of 500 knots is:

$$\Delta f = 8.574 \times 10^{-7} f_{o}$$

where f_{o} is laser frequency. For the DF 2-1 P7 line (for example) the doppler shift at 500 knots is:

$$\Delta f = 8.574 \times 10^{-7} \times 2655.863 \text{ per cm}$$

$$= 0.00228 \text{ waves/cm}$$

This is less than the order of accuracy (0.003/cm) stated for the best available DF laser frequency measurements (Ref. 16). Comparing this value with transmittance spectra available from OSU, AFCRL, and SAI, it is concluded that the effect would be a marginal one, of no practical significance with respect to transmittance from a B-52. It appears that the shift would start to be significant (for a few DF laser lines) at about 0.01 cm^{-1} Δf, or a velocity of about 2000 knots. Doppler shift would probably cause a small (but insignificant) improvement in the transmittance of most CO_2 laser lines, because the shift would be away from the peak of the related CO_2 absorption line in the atmosphere.

Section A-3
PATH RADIANCE AND TRANSMITTANCE

PATH EQUATION FOR RECEIVED POWER

Assume that emitted or reflected energy from a target element of uniform radiance is focused upon a sensor surface or detector element of a photometer, radiometer, or other receiver which is at some distance from the target. For a horizontal path of uniform characteristics, the power received by the sensor element can be written as follows:

$$P_R = N_t T_a (K) + N_b (SF)\ (K) + N_m\ \varepsilon_m\ (K) \qquad \text{(A-1)}$$

where P_R = effective received power, watts

N_t = target element radiance, watts/m^2-ster.

K = $\Omega(\pi/4)\ d^2\eta$ (a "receiver factor")

N_b = effective average background radiance contributing to scattering, watts/m^2-ster.

SF = scattered fraction; the fraction of "average" background radiance scattered into the radiometer FOV. $SF = (\sigma/\gamma(1 - e^{-\gamma R})$

N_m = blackbody radiance at the air temperature of the transmission path

ε_m = the effective emissivity of the air mass within the radiometer FOV. The value of ε_m is

$$\frac{k}{\gamma}\ (1 - e^{-\gamma R})$$

Ω = detector element FOV, steradians

d = receiver effective clear aperture diameter, meters

η = detector quantum efficiency

σ = atmospheric scattering coefficient, per kilometer

k = atmospheric absorption coefficient, per kilometer

γ = atmospheric attenuation coefficient, per kilometer

T_a = path transmittance, = $e^{-\gamma R}$

PATH EQUATION NORMALIZED TO RADIANCES

Equation (A-1) shows the received power to be composed of a target component, an atmospheric scattering component, and an air mass radiance component, respectively. If the receiver factor, K, is factored out, Equation (A-1) may be written as:

$$\frac{P_R}{K} = N_a = N_t T_a + N_b (SF) + N_m \varepsilon_m \quad * \qquad (A\text{-}2)$$

where N_a is an "apparent" or measured radiance. Hence the measured radiance is composed of target, atmospheric scattering, and atmospheric emission radiance components.

SCOPE OF APPLICATION

Equations (A-1) and (A-2) apply strictly only to a uniform horizontal path and to narrow spectral regions over which the absorption and scattering coefficients are constant, so that exponential transmittance applies. Under other circumstances, more accurate estimates may be obtained through use of one of the available band transmittance models (e.g., LOWTRAN). Such models use experimentally-derived empirical relationships for calculating the average optical absorption of atmospheric constituents which have highly structured spectral characteristics.

With appropriate caution, and with due regard for the approximate nature of the results, Equations (A-1) and (A-2) have been found useful in estimating horizontal path transmittances and radiances and in pointing the way to calculation of slant path transmittances and radiances for wavelength bands.

VERTICAL AND SLANT PATH CALCULATIONS

For vertical and slant path calculations, the first term of Equation (A-2), $N_t T_a$, is relatively easy to calculate. The scattering and thermal

* This expression is a much-simplified version of La Rocca's general equation for "the atmospheric radiative transfer equation," Equation (1) of Ref. 17.

radiance terms, however, must ideally be calculated on a continuously variable or layer-by-layer basis, with the radiance of each differential thickness or layer attenuated to the observer location by the transmittance of the intervening path. Such computations can be tedious and time-consuming, even when layers of one-kilometer thickness are assumed, as in using the McClatchey coefficient tables from References 1, 4, and 5.

It was determined, however, that the integrated scattering fraction, SF, and the integrated air mass emissivity, ε_m, over a vertical or slant path are independent of the variation of σ and k with altitude. Hence, if N_b and N_m were reasonably constant with altitude, the layer-by-layer computation would be unnecessary. This simplification is reasonable for N_b, but not for N_m, hence its applicability is essentially limited to the visible band.

DERIVATION OF SIMPLE PATH RADIANCE FORMULA FOR VISIBLE WAVELENGTHS

Taking the layer-by-layer approach, the path radiance, looking vertically downward from a point above the earth, is given by:

$$N_a = \sum_{\text{all } \Delta r_i} \left[N_{b(\Delta r_i)} \frac{\sigma_{(\Delta r_i)}}{\gamma_{(\Delta r_i)}} \left(1 - e^{-\gamma(\Delta r_i)} \right) \left(e^{-\Sigma\gamma(r_i)} \right) \right.$$

$$\left. + N_{m(\Delta r_i)} \frac{k_{(\Delta r_i)}}{\gamma_{(\Delta r_i)}} \left(1 - e^{-\gamma(\Delta r_i)} \right) \left(e^{-\Sigma\gamma(r_i)} \right) \right] \qquad \text{(A-3)}$$

where the first term is the scattering component and the second is the thermal radiation component. The (Δr_i) subscript signifies the i^{th} layer of thickness Δr, and $\Sigma\gamma_{(r_i)}$ signifies the total optical depth from the observer to the i^{th} layer. For a slant path, each σ, k, and γ is multipled by sec θ, where θ = path zenith angle.

In the visible wavelength region, absorption is negligible in comparison to scattering, while in the 8-13 micrometer IR region, scattering is small

compared to absorption and resultant thermal emission. Hence Equation (A-3) can be considerably simplified for computation in either of these regions. In the visible region, for example, it can be reduced to

$$N_s \simeq \sum_{\text{all } \Delta r_i} \left[N_{b(\Delta r_i)} \left(1 - e^{-\sigma(\Delta r_i)} \right) \left(e^{-\Sigma\sigma(r_i)} \right) \right] \cdots \qquad \text{(A-4)}$$

Then, if N_b is considered constant with altitude, Equation (A-4) for the visible region reduces to

$$N_s \simeq N_b \sum_{\text{all } \Delta r_i} \left[\left(1 - e^{-\sigma(\Delta r_i)} \right) \left(e^{-\Sigma\sigma(r_i)} \right) \right] \cdots \qquad \text{(A-5)}$$

Dividing through by N_b and writing the summation term by term, Equation (A-5) becomes

$$\frac{N_s}{N_b} \simeq SF = \left(1 - e^{-\sigma_1}\right)\left(e^{-(\sigma_2 + \cdots \sigma_{12})}\right)$$

$$+\left(1 - e^{-\sigma_2}\right)\left(e^{-(\sigma_3 + \cdots \sigma_{12})}\right)$$

$$+\left(1 - e^{-\sigma_3}\right)\left(e^{-(\sigma_4 + \cdots \sigma_{12})}\right)$$

$$\vdots$$

$$+\left(1 - e^{-\sigma_{11}}\right)\left(e^{-\sigma_{12}}\right)$$

$$+\left(1 - e^{-\sigma_{12}}\right)\left(e^{-0}\right)$$

Scattered fraction contributions by layers, assuming each layer is 1 km thick and σ values are in km^{-1}. Also, that observer is 12 km above surface.

Performing the indicated multiplications:

$$
\begin{aligned}
SF = {} & e^{-(\sigma_2 + \cdots \sigma_{12})} - e^{-(\sigma_1 + \sigma_2 + \cdots \sigma_{12})} \\
& + e^{-(\sigma_3 + \cdots \sigma_{12})} - e^{-(\sigma_2 + \sigma_3 + \cdots \sigma_{12})} \\
& + e^{-(\sigma_4 + \cdots \sigma_{12})} - e^{-(\sigma_3 + \sigma_4 + \cdots \sigma_{12})} \\
& \cdot \\
& \cdot \\
& \cdot \\
& + e^{-\sigma_{12}} - e^{-(\sigma_{11} + \sigma_{12})} \\
& + 1 - e^{-\sigma_{12}} \\
= {} & 1 - e^{-(\sigma_1 + \sigma_2 + \cdots \sigma_{12})} = \underline{\underline{1 - T_a}}
\end{aligned}
$$

This is the simple formula for path radiance (scattered fraction) that is commonly used for horizontal path calculations at visible wavelengths. Switching to photometric terminology, the visible path brightness, B_s, is given by:

$B_s = B_b (1 - T_a)$ for any path over which the average background brightness, B_b, can be assumed reasonably constant.

A check on this result was performed using the layer-by-layer approach. The results are tabulated in Table A-1 (for the SIS 66-km slant path, and a mid-latitude/summer "clear" atmosphere). The reader is also referred to Boileau (Ref. 18) for tables of slant path radiances (luminances), measured from an aircraft in flight.

IR WAVELENGTH REGION OF 8-13 MICROMETERS

In this wavelength region, scattering is small compared to absorption and resultant thermal emission, so that Equation (A-3) can be reduced to:

$$
N_T \simeq \sum_{\text{all } \Delta r_i} \left[N_{m(\Delta r_i)} \left(1 - e^{-k(\Delta r_i)} \right) \left(e^{-\Sigma k(r_i)} \right) \right] \cdots \qquad \text{(A-6)}
$$

Table A-1. Example Layer Summation of Path Radiances at Visible Wavelengths; Clear Atmosphere, 66-km Slant Path

1	2	3	4	5	
Layer (km)	Ave σ_t* (km^{-1})	Layer SF = $1 - e^{-a\sigma_t}$**	$\Sigma \sigma_t$ to Layer	T to Layer $=e^{-\Sigma a\sigma_t}$	SF Contrib. = 3 x 5
0-1	0.1263	0.495	0.19893	0.341	0.169
1-2	0.0615	0.283	0.13743	0.475	0.134
2-3	0.0323	0.160	0.10513	0.566	0.091
3-4	0.02026	0.104	0.08487	0.632	0.066
4-5	0.01567	0.0813	0.06920	0.688	0.056
5-6	0.01305	0.0682	0.05615	0.738	0.050
6-7	0.01132	0.0594	0.04483	0.785	0.047
7-8	0.01045	0.0550	0.03438	0.830	0.046
8-9	0.00970	0.0511	0.02468	0.875	0.045
9-10	0.00892	0.0471	0.01576	0.918	0.043
10-11	0.00817	0.0432	0.00759	0.960	0.041
11-12	0.00759	0.0402	0	1	0.040
Totals	0.32523				0.827***

$T_a = e^{-5.41(0.32523)}$
$= 0.172$***

*: $\sigma_t = \sigma_m + \sigma_a$ at 0.5145 micrometer, from AFCRL-72-0497.

**: $a = \sec \theta = 5.41$

***: The resulting total SF = 0.827, which agrees with $1 - T_a$, = 1 - 0.172 = 0.828.

$N_{m(\Delta r_i)}$ is the equivalent blackbody radiance of the i^{th} Δr layer, and its value is a moderately strong function of altitude. Hence the simplification made at this point for visible wavelengths ($N_b \simeq$ constant with altitude) has no counterpart in this wavelength region, and the path radiance is <u>not</u> approximately given by a constant multiplied by $(1 - T_a)$.

Layer-by-layer summation of path thermal radiance (for the mid-latitude summer model) was calculated at 10.591 micrometers for the SIS 66-kilometer slant path, as shown by Table A-2. The results were

$$N_T = 15.9/\pi = 5.06 \text{ watts/m}^2\text{-ster-}\mu\text{m}, \underline{\text{looking down}},$$

and

$$N_T = 27.0/\pi = 8.59 \text{ watts/m}^2\text{-ster-}\mu\text{m}, \underline{\text{looking up}}.$$

It is clear from this example that the path radiance (thermal) can not be given by $N_m(1 - T_a)$ since the path radiance is different "looking up" and "looking down," even though T_a must be the same in both directions.

The layer-by-layer summation process was exercised to obtain approximate average values of path radiance and path transmittance, for the 8-12 micrometer band. The process was repeated, for "clear" and "hazy" atmospheres, for two latitude/season models, and for 5 horizontal ranges (0, 9, 18, 27, and 35 nautical miles), looking down from 40,000 feet altitude. The starting points for these calculations were estimated average values of 66-km slant path transmittances read from the computer-calculated graphs* (see Section A-6).

*Note: LOWTRAN 3 runs of August-September 1975 were used. Results as shown in Table A-3 and Figure A-9 would be modified somewhat if the computations were repeated using "Modified LOWTRAN 3" results. With respect to Figure A-9, a brief "eyeball" comparison of LOWTRAN 3 and Modified LOWTRAN 3 indicates approximate improvements as follows, for the 35 nm and 0 nm (vertical) transmittances of Figure A-9 using modified LOWTRAN 3: (note continued on page 22)

Table A-2. 66-km Slant Path Air Mass Thermal Radiance at Receiver, at 10.591 μm, Assuming Molecular Absorption Only

Total vertical OD = 0.94359; $T_a = e^{-5.41(0.94359)} = 0.0061$

Layer (km)	^oK Ave. Temp.	@ 10.6 N_{bb}* $W/m^2-\mu m$	Ave k_m (km^{-1})	Air Mass Emiss. Layer $\varepsilon = 1-e^{-5.41k_m}$	ΣOD to Layer	T_a to Layer $=e^{-5.41\Sigma OD}$	$W/m^2-\mu m$ N_s* Contrib.
Looking down: mid-latitude summer (very clear)							
0-1	292	27.8	0.3256	0.828	0.61799	0.035	0.806
1-2	287.5	25.7	0.1877	0.638	0.43029	0.098	1.60
2-3	282	23.7	0.1152	0.464	0.31509	0.182	2.00
3-4	276	21.3	0.07582	0.336	0.23927	0.274	1.96
4-5	270	19.1	0.05544	0.259	0.18383	0.370	1.83
5-6	264	16.9	0.04468	0.215	0.13915	0.471	1.71
6-7	258	15.0	0.03752	0.184	0.10163	0.577	1.59
7-8	251.5	13.3	0.03018	0.151	0.07145	0.679	1.36
8-9	245	11.7	0.02378	0.121	0.04767	0.773	1.09
9-10	238.5	9.72	0.01952	0.100	0.02815	0.859	0.83
10-11	232	8.40	0.01574	0.082	0.01241	0.935	0.64
11-12	225.5	7.18	0.01241	0.065	0	1	0.47
		Total =	0.94359			Total =	15.9*
Looking up: mid-latitude summer (very clear)							
0-1		27.8		0.828	0	1	23.02
1-2		25.7		0.638	0.3256	0.172	2.82
2-3		23.7		0.464	0.5133	0.0622	0.68
3-4		21.3		0.336	0.6285	0.0334	0.24
4-5		19.1		0.259	0.70432	0.0221	0.11
5-6		16.9		0.215	0.75976	0.0164	0.06
6-7		15.0		0.184	0.80444	0.0129	0.04
7-8		13.3		0.151	0.84196	0.0105	0.02
8-9		11.7		0.121	0.87214	0.00893	0.01
9-10		9.72		0.100	0.89592	0.00785	0.008
10-11		8.4		0.082	0.91544	0.00707	0.005
11-12		7.18		0.065	0.93118	0.00649	0.003
						Total =	27.0*

* Radiant emittances; divide N_s by π to get radiances.

Mid-latitude summer		Mid-latitude winter	
35 nm	vertical	35 nm	vertical
70-80%	10-12%	20-25%	3-5%

Correction of the path radiance curves has not been attempted; however, some decrease in values would result.

Estimated average values of total path and kilometer layer values of γ, σ, and k were derived from these computer-calculated transmittance values and previously calculated values of aerosol attenuation for this path. It is cautioned that this approach is an approximation, for the reason previously stated. However, experience has shown that the approximation is a reasonable one for the circumstances of this particular problem. (The alternate approach is a host of LOWTRAN runs to produce the layer-by-layer radiance and transmittance data required, or a new path radiance computer program which would compute path radiance more directly.)

Table A-3 is a sample tabulation (1 of 16) involved in the manual calculations. The model atmosphere air temperatures are from McClatchey (Ref. 1), and the associated blackbody radiance values were derived using the G.E. Radiation Calculator. Layer-by-layer average molecular absorption coefficient values, k_m, were taken as 0.303 of McClatchey's values at 10.591 micrometers, for mid-latitude summer, and 0.425 for mid-latitude winter, based upon the cited derivations, and altitude variations in the aerosol absorption coefficient were taken at the same ratio as in McClatchey.

IR WAVELENGTH REGION OF 3-5 MICROMETERS

In this wavelength region the atmosphere exhibits optical properties which are a composite of those for the shorter and longer wavelength bands. Molecular and aerosol absorption and aerosol scattering are all significant in the attenuation equation, and both scattering and thermal radiation should be considered in estimating path radiance. Portions of this band (in the vicinity of 2.2 and 3.8 micrometers) exhibit optimum optical transmission over a wide range of atmospheric variables. Optical energy in these wavelength regions penetrates atmospheric haze much better than shorter (e.g., visible) wavelengths, and is much less affected by atmospheric water vapor than longer wavelengths (e.g., the 8-13 micrometer IR region).

Table A-3. Estimated 66-km Slant Path Air Mass Thermal Radiance over 8-12 μm Wavelength Region Looking Down from 40 K' (12.192 km)

Horizontal range 35 nm, 64.82 km; $\theta = 79.35^{o}$; sec θ = 5.41 (=a)

Layer (km)	oK Ave. Temp.	N_{bb}* Watts/ m^2-ster-μm	Ave. γ_t (km^{-1})	Layer Emissivity = $\frac{k_t}{\gamma_t}\left(1-e^{-a\gamma_t}\right)$	OD to Layer	T to Layer = $e^{-a\Sigma OD}$	W/m^2-μm N_s* Contrib.
Mid-latitude summer (hazy)							
0-1	292	8.83	0.18454	0.544	0.29119	0.207	0.994
1-2	287.5	8.03	0.09668	0.368	0.19451	0.349	1.03
2-3	282	7.42	0.05515	0.242	0.13936	0.471	0.846
3-4	276	6.67	0.03449	0.164	0.10487	0.567	0.620
4-5	270	5.93	0.02439	0.121	0.08048	0.647	0.464
5-6	264	5.10	0.01941	0.098	0.06107	0.719	0.359
6-7	258	4.57	0.01629	0.083	0.04478	0.785	0.298
7-8	251.5	4.00	0.01316	0.068	0.03162	0.843	0.229
8-9	245	3.42	0.01044	0.054	0.02118	0.892	0.165
9-10	238.5	2.86	0.00862	0.045	0.01256	0.934	0.120
10-11	232	2.49	0.00699	0.036	0.00557	0.970	0.087
11-12	225.5	2.09	0.00557	0.029	0	1	0.061
		Totals =	0.47573	(T_a = 0.076)			5.27
Mid-latitude winter (hazy)							
0-1		8.83	0.06832	0.193	0.116415	0.533	0.908
1-2		8.03	0.03477	0.125	0.081645	0.643	0.645
2-3		7.42	0.02107	0.090	0.060575	0.721	0.481
3-4		6.67	0.01452	0.069	0.046055	0.779	0.359
4-5		5.93	0.01064	0.054	0.035415	0.826	0.265
5-6		5.10	0.008363	0.043	0.027052	0.864	0.189
6-7		4.57	0.006842	0.035	0.02021	0.896	0.143
7-8		4.00	0.005569	0.029	0.014641	0.924	0.107
8-9		3.42	0.004587	0.024	0.010054	0.947	0.078
9-10		2.86	0.003600	0.018	0.006454	0.966	0.050
10-11		2.49	0.003277	0.017	0.003177	0.983	0.042
11-12		2.09	0.003177	0.016	0	1	0.033
		Totals =	0.184735	(T_a = 0.368)			3.30

Columns 4 and 5 data are from a separate tabulation.

* Radiant emittances; divide N_s by π to get radiances; N_{bb}* (Layer ε) (T_a to layer).

Note: The note on page 20 regarding LOWTRAN 3 applies to this page also.

The path radiance in this region will be relatively small for two reasons: (1) the natural daylight illumination is much reduced compared to the visible, and (2) thermal radiance is much reduced compared to the 8-13 micrometer IR band. However, accurate calculations of path radiance are much more laborious because the simplifying approximations of those bands do not apply in the 3-5 micrometer region.

We have not attempted to make estimates of path radiance for the 66-kilometer SIS slant path in this wavelength region. However, computer calculated band transmittances and manually calculated transmittance values for many DF laser lines in this region have been accomplished, as reported in Sections A-6 and A-10.

AEROSOL MODELS

The aerosol model used in the calculations reported herein is AFCRL's "average continental aerosol model" (1974) supplied to SRL by Reference 19. (More recently, this model appears in the aerosol spectral data table of the LOWTRAN 3 computer code, Reference 8, p. 86. The LOWTRAN 3 report, dated 7 May 1975, was distributed in December 1975.) The vertical distribution of particle densities for this model is given on page 9 of Reference 1, for normalized "clear" (S.L. visibility = 23 km) and normalized "hazy" (S.L. visibility = 5 km) atmospheres. In SRL's normalized "light haze" atmosphere (S.L. visibility = 10.8 km) the particle density at each altitude is the geometric mean of the "clear" and "hazy" values.

AFCRL also has an "estimated marine aerosol model," an advance copy of which was supplied to SRL by Reference 20, and several other models (i.e., urban and rural) intended for near-future publication in a supplement to LOWTRAN 3. We have exercised the marine model to some extent on the SIS study, as reported in other sections of this appendix.

RESULTS

Some typical calculated results are illustrated in Figures A-5 through A-9, and others may be found elsewhere in this appendix.

Figures A-5 through A-7 show calculated values of slant path transmittance at wavelengths of 0.6525 micrometer, 0.55 micrometer, 3.73 micrometer, and 10.591 micrometer. The visible wavelength curves are nearly independent of latitude-season model. For example, the curves for 0.55 micrometer and 0.6525 micrometer apply within 0.002 for any of the five McClatchey latitude-season models. On the other hand, the large dependence upon haze level is clearly shown, for these wavelengths.

At the other extreme, the small dependence of 10.591 micrometer transmittance upon haze level, and the large dependence upon latitude-season model, are clearly shown. The 3.73 micrometer curves show an intermediate level of dependence upon both factors.

Figure A-8 illustrates slant path luminance at 0.55 micrometer, the mid-point of the visible band, calculated from the simple formula previously discussed.

Figure A-9 illustrates calculated band transmittance averages and path radiances for the 8-12 micrometer band, computed according to the layer-by-layer method previously described. Both sets of curves (transmittance and path radiance) show the cited strong dependence upon latitude-season model, with lesser dependence upon the haze level. Comparison of these curves with those of Figure A-7 shows the relatively better transmittance of the 8-12 micrometer band as compared to monochromatic transmittance of a CO_2 laser wavelength. (Also, see Note, page 20.)

While comparable curves comparing 3-5 micrometer band transmittance with DF laser monochromatic transmittances have not been developed, review of available data shows that most DF laser lines exhibit better atmospheric transmittance than the average band transmittance. This is opposite to what occurs in the 8-12 micrometer band with respect to band and CO_2 laser line transmittances.

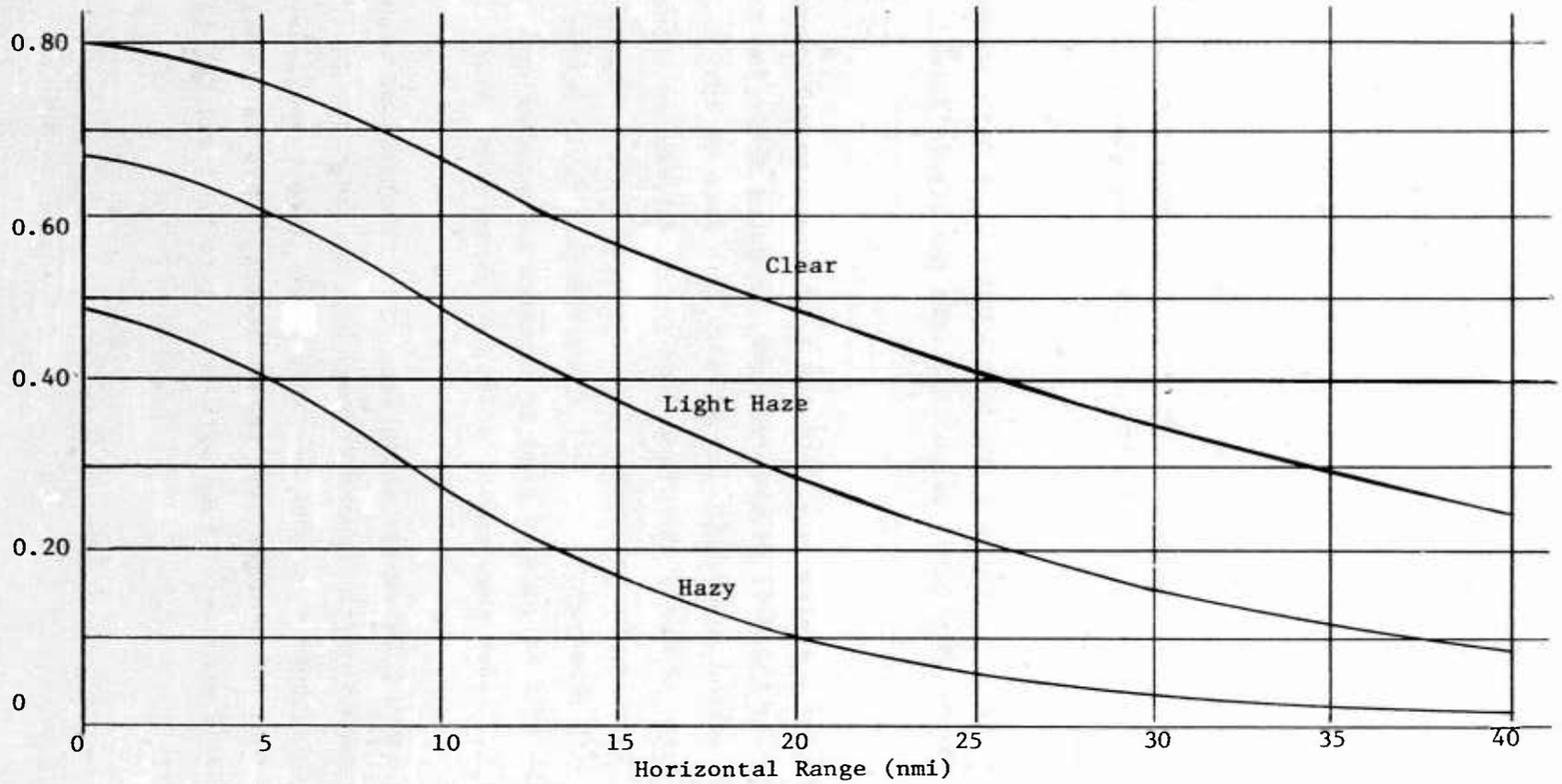

Figure A-5. Typical Calculated Slant Path Transmittances, 40,000 Feet to Sea Level, 0.6525 Micrometer

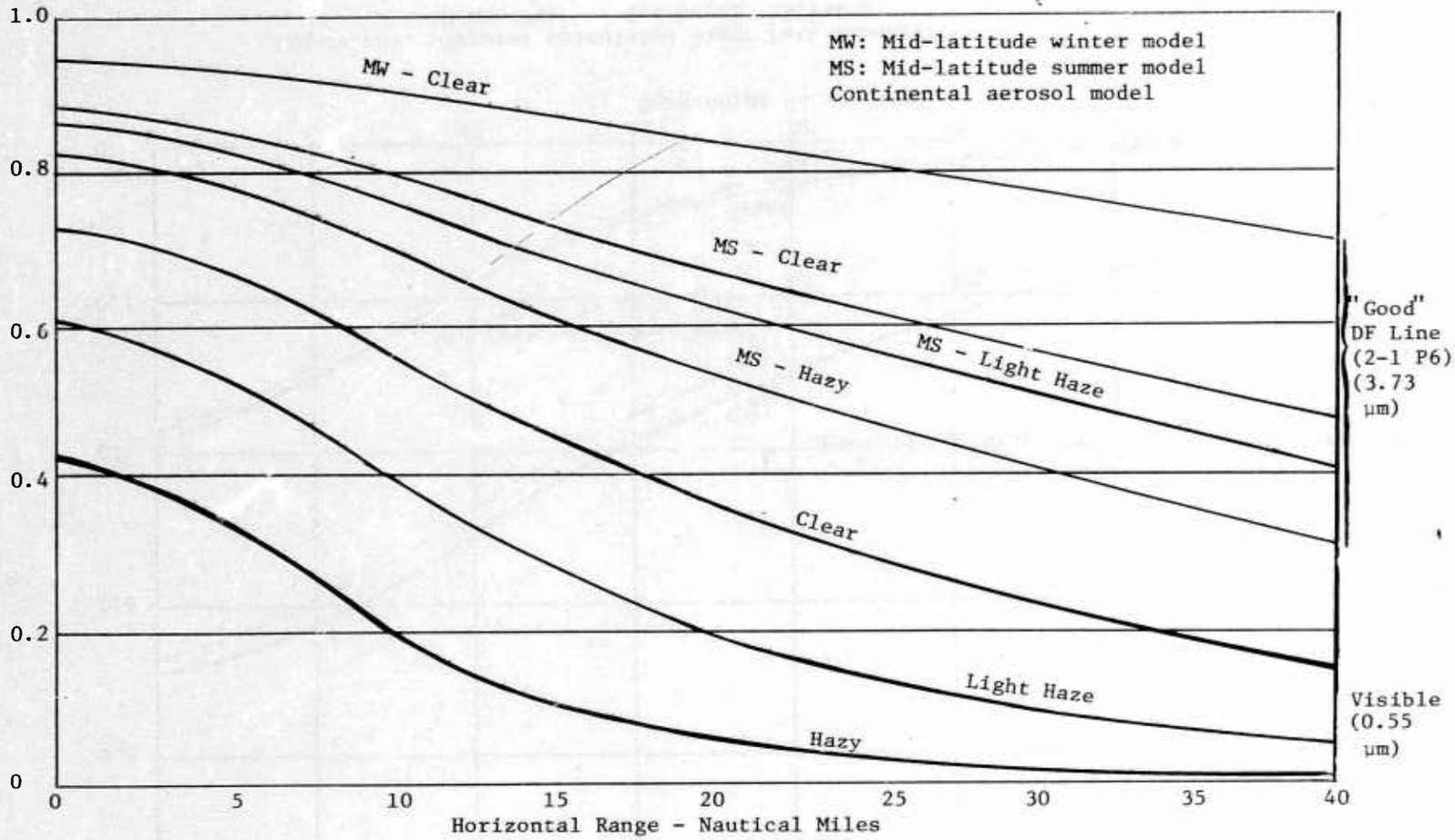

Figure A-6. Typical Calculated Slant Path Transmittances, 40,000 Feet to Sea Level, 3.73 and 0.55 Micrometer

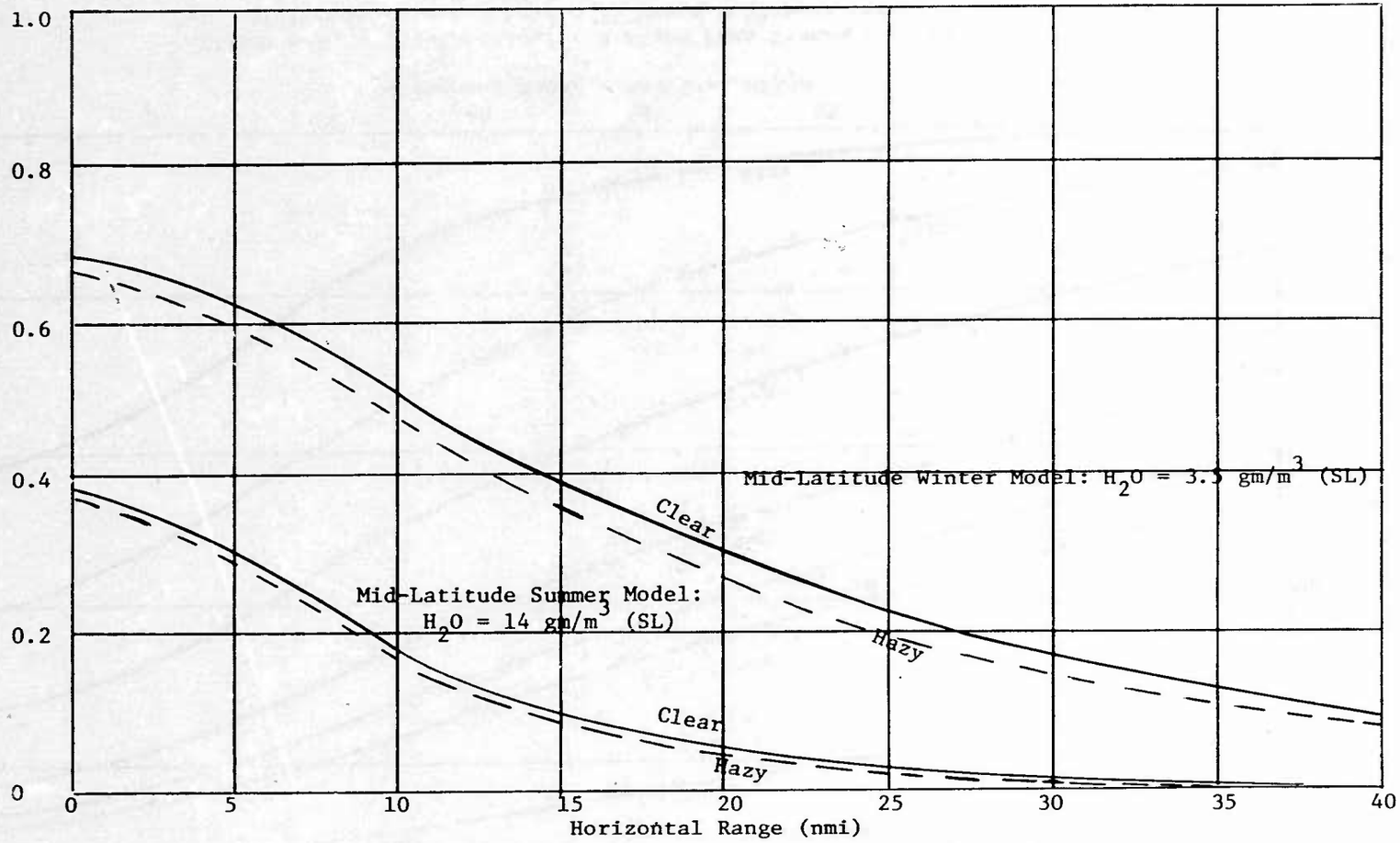

Figure A-7. Typical Calculated Slant Path Transmittances, 40,000 Feet to Sea Level, 10.591 μm

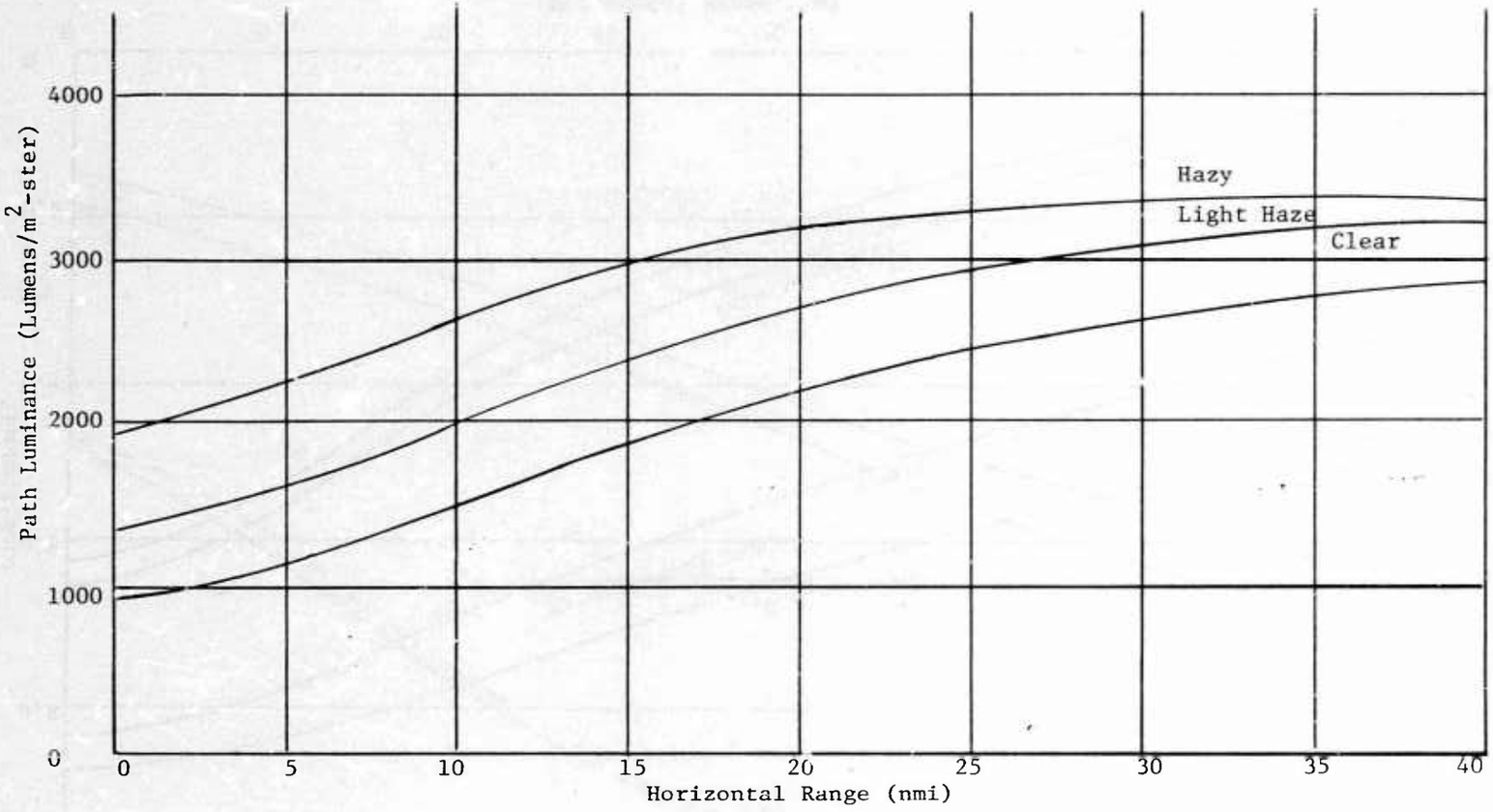

Figure A-8. Typical Calculated Path Luminance for 40,000 Feet to Sea Level Path (Sky Brightness = 3400 Lumens/m^2-ster, Visible Wavelength Region (0.55 μm), Mid-Latitude Summer

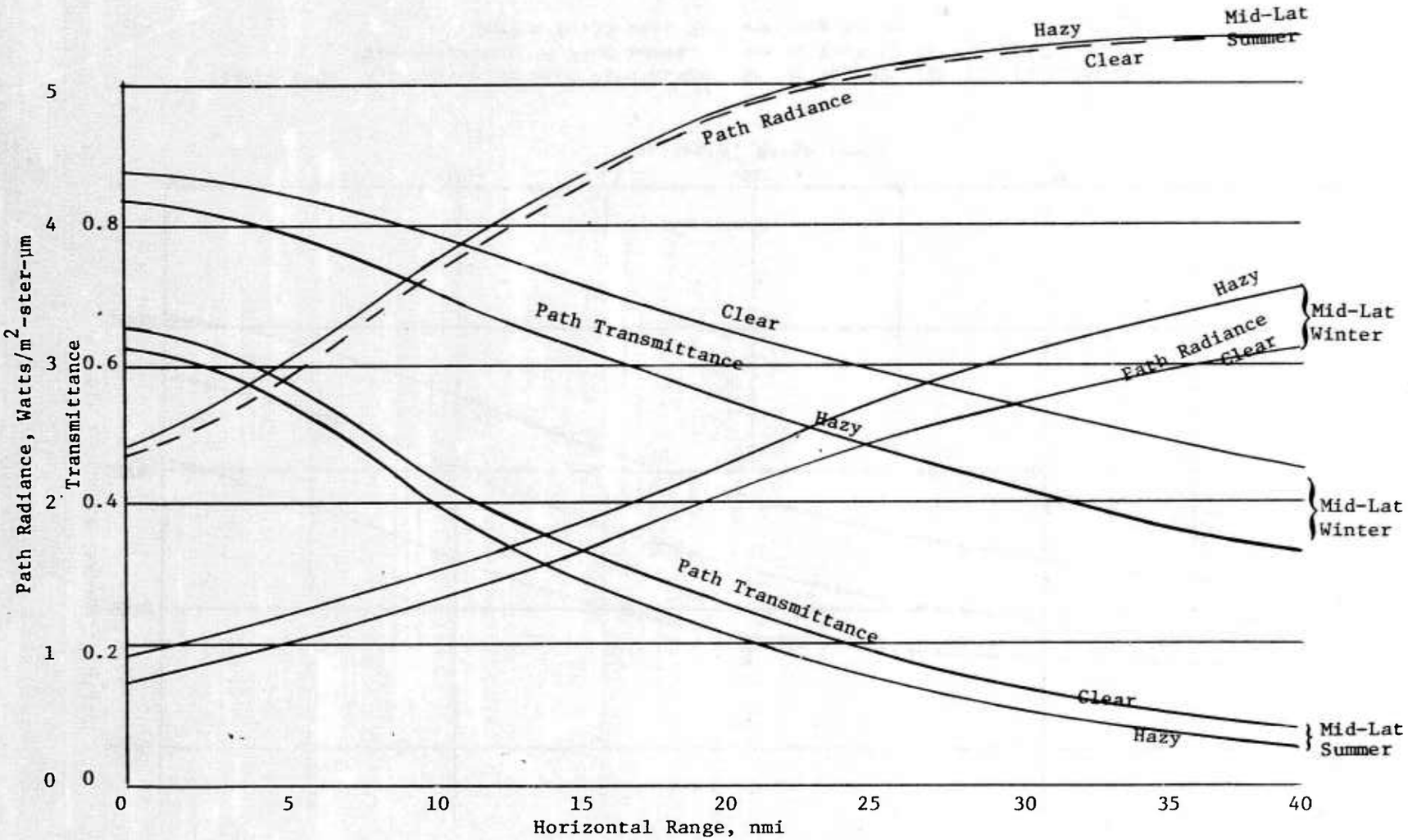

Figure A-9. Estimated Slant Path Transmittance and Air Mass Thermal Radiance, 40,000 Feet to Sea Level (Average for 8-12 µm Band)

Section A-4

ATMOSPHERIC OPTICAL TURBULENCE

INTRODUCTION

Identification schemes which utilize optical signals will be adversely affected by the propagation of these signals through a turbulent atmosphere. It is convenient to divide the propagation path into two parts, the turbulent aircraft boundary layer and the free atmosphere. The reason for this division is that the free atmosphere optical turbulence is caused primarily by thermally induced air density fluctuations, and is characterized by a Kolmogorov-type refractive index fluctuation spectrum, while the boundary layer optical turbulence is caused primarily by mechanically induced density fluctuations whose structure is quite different.

The theory of free atmosphere optical turbulence has been developed and experimentally verified sufficiently to permit the direct calculation of optical signal degradation. However, the theory of aircraft boundary layer optical turbulence is not so well developed, and experimental results are only presently being obtained. For the present purpose, we must rely on preliminary data for estimates of the aircraft boundary layer effect. Since the types of degradations produced by the boundary layer are the same as those produced by the free atmosphere, we proceed to a brief description of free atmosphere turbulence.

FREE ATMOSPHERE TURBULENCE

Background

The origin of the free atmosphere turbulence effects lies in the fact that the refractive index at a point in the atmosphere exhibits small fluctuations about its mean value. The fluctuations are correlated only over short distances, and hence produce a general degradation in optical signals propagating through the atmosphere. Clearly, a detailed description of the degradation is not possible without a detailed knowledge of the refractive index space-time dependence. However, a statistical description

of the refractive index fluctuations does permit a statistical description of the resultant optical degradation. It is this approach which has been used by many authors to obtain useful formulae for calculating the various degradations produced by atmospheric turbulence. A major portion of the theory is contained in the volume by Tatarski (Ref.14), and the review articles by Lutomirski et al (Ref.13) and by Lawrence and Strohbehn (Ref.21) provide useful practical discussions and summaries of more recent important theoretical and experimental results.

Refractive index fluctuations arise primarily from temperature fluctuations in the atmosphere, which in turn are produced by the turbulent mixing of hot air (usually heated by the earth's surface) with cool air. The mixing occurs through a series of eddies ranging in size from L_o ($\simeq$ 1 meter near the surface) to ℓ_o ($\simeq$ 1 millimeter). L_o and ℓ_o are called the outer and inner scales of turbulence. Pressure and humidity fluctuations also produce index fluctuations, but their effect is usually negligible compared with temperature fluctuations. An exception to this rule occurs when dry air mixes with moist air, as might occur at a land-sea interface (Ref.22).

A useful descriptor of the index fluctuations at a point z along a propagation path is the spatial index power spectrum $\Phi_n(\vec{K},z)$, which is defined as the three-dimensional Fourier transform of the index spatial correlation function. For locally isotropic turbulence, $\Phi_n(\vec{K},z)$ is often written

$$\Phi_n(\vec{K}, z) = \frac{0.033\, C_n^2(z)\, e^{-(K\ell_o)^2}}{\left[K^2 + L_o^{-2}\right]^{11/6}} \qquad \text{(A-7)}$$

where K is the spatial frequency and $C_n^2(z)$ is a parameter which is a measure of the strength of the turbulence (the rms index fluctuation is approximately $C_n L_o^{1/3}$). The gross spatial dependence of Φ_n is contained in $C_n^2(z)$. For many applications, the Φ_n dependence on ℓ_o and L_o can be supressed, yielding the Kolmogorov spectrum

$$\Phi_n(K,z) = 0.033\, C_n^2(z)\, K^{-11/3} \qquad \text{(A-8)}$$

Since no good models exist for the outer scale at high altitudes and since the inner scale can usually be neglected, we utilize the Kolmogorov spectrum for this application. We note that C_n^2 has the dimension of $(\text{length})^{2/3}$ and that the constant 0.033 is appropriate when MKS units are used.

A useful conceptualization of the refractive index field is to imagine a dynamic collection of arbitrarily shaped lenses having different refractive indices with sizes ranging from ℓ_o to L_o. An optical wave passing through the atmosphere will then undergo a series of focusings and steerings, and will impinge on a target or receiver with considerable degradation. The degradation will be manifest in a variety of ways, depending on the type of optical wave involved (i.e., spherical wave, focused beam, or reflected ambient light), the viewing techniques (i.e., point detection or imaging system), and the coherence of the initial optical signal as well as other factors.

Most treatments divide the total wave degradation for infinite extent wavefronts into two parts: amplitude fluctuations and phase fluctuations. The amplitude fluctuations, termed scintillation, are produced primarily by the focusing action of the index field and are observed as a breakup of the wavefront into fluctuation patches of high and low intensity. The phase fluctuations are produced primarily by the steering action of the index field and are observed to first order as fluctuations in the angle of arrival (wavefront propagation direction) of the radiation.

The same division (amplitude and phase) is generally carried over in treatments of finite beam degradation. However the turbulence will also produce two additional effects, motion of the beam centroid (beam wander) and fluctuations and enlargement of the beam waist (beam spread). These effects are the result of first order and higher phase fluctuations respectively. In passing, we note that intensity fluctuations actually observed at a point in the beam may be due both to scintillation and to beam wander. The scintillation which we estimate below should be taken as the intensity fluctuation at the beam center.

In imaging systems, the wavefront incident on the receiver will be degraded by scintillation and by phase distortion. However, it is not these degradations directly but rather those observed in the image plane which are of interest. In general, a point in the image will show power fluctuations due to scintillation, motion (image dancing) due to first order phase fluctuations, and spreading (increase in the point spread function (PSF) width) due to higher order phase degradations. The power fluctuations are often negligible due to the averaging effect of the receiver and source.

Before discussing the specific turbulence-produced effects studied here, we point out that the time frame in which observations are made can be important. For example, in a short time (approximately 10 ms) imaging system, the resolution will be determined by the instantaneous point spread function, and will not be affected by the image dancing. However, for long-time averaging (as in a 10 second photographic exposure), the image dancing will be convoluted with the PSF, yielding a further decrease in resolution. When each image point is a short-time average, but the image frame is collected over a long time, the overall effect will be a high-resolution image (as determined by the instantaneous PSF), with considerable distortion as determined by the image dancing.

Analysis

A general optical ship identification system will potentially utilize an illuminator and an imaging receiver. The turbulence degradations which need be considered for the illuminator are scintillation, beam wander, instantaneous beam spread, and long-term beam spread. For an imaging receiver, we need to consider scintillation, image dancing, instantaneous point spread function, and long-term point spread function. We now present the formulae used to estimate these effects. Since formulae for finite beam propagation are complex and unwieldy, and since plane wave or point source (spherical wave) formulae often yield adequate approximations, we use those formulae where applicable.

The descriptor for scintillation is σ_ℓ^2, the variance of the distribution for the natural logarithm of the normalized intensity as observed by a point receiver. For spherical wavefronts of wave number $k = 2\pi/\lambda$, propagating from position $z' = 0$ to position $z' = z$, σ_ℓ^2 is given by

$$\sigma_{\ell,s}^2 = 4\pi^2 \int_0^z dz'(z-z')^2 \left[\frac{z'}{z}\right]^2 \int_0^\infty K^5 dK\, \Phi_n(K,z') \times \frac{\sin^2\left[\frac{K^2 z'(z-z')}{2kz}\right]}{\left[\frac{K^2 z'(z-z')}{2kz}\right]^2} \tag{A-9}$$

For the Kolmogorov spectrum, this equation reduces to

$$\sigma_{\ell,s}^2 = 2.24\, k^{7/6} \int_0^z (z-z')^{5/6} \left(\frac{z'}{z}\right)^{5/6} C_n^2(z')dz' \qquad \text{(A-10)}$$

The corresponding equation for plane waves is

$$\sigma_{\ell,p}^2 = 2.24\, k^{7/6} \int_0^z (z-z')^{5/6} C_n^2(z')dz' \qquad \text{(A-11)}$$

We note that, for spherical waves, turbulence near the path midpoint is weighted strongest, but for plane waves the strongest weighting is for turbulence near the source.

These equations yield good agreement with measurements for $\sigma_\ell^2 \lesssim 1$; however, for strong turbulence and/or long propagation paths such that $\sigma_\ell^2 > 1$, the formulae yield values which are too large. Experimentally, a saturation of scintillation occurs. An empirical correction factor has been obtained (Ref.23) which yields a corrected $\sigma_{\ell,c}$ given by

$$\sigma_{\ell,c} = \frac{\sigma_\ell}{1 + A\sigma_\ell^B} \qquad \text{(A-12)}$$

where A and B are constants with a slight wavelength dependence.

In addition to the saturation correction, the averaging effect of the receiver (or resolution element for the illuminator) must be considered. A useful engineering formula for the aperture average correction factor is (Ref.13)

$$a = \frac{1}{1 + \left(\frac{D}{2\rho_\ell}\right)^2} \qquad \text{(A-13)}$$

Then $\sigma_{\ell,av}^2 = a\, \sigma_{\ell,c}^2$

where D is the receiver diameter and ρ_ℓ is the transverse amplitude correlation length and is given approximately by

$$\rho_\ell = \sqrt{\frac{k}{z}} \tag{A-14}$$

This factor "a" is somewhat optimistic for $\sigma_\ell^2 > 1$, but is accurate enough for the work at hand (Refs 24, 25).

For imaging systems, one further correction is needed to account for the averaging over the resolution element at the target. Lutomirski (Ref.13) gives this factor as

$$S = \left(\frac{\rho_\ell}{r}\right)^{7/3}; \quad \text{then} \quad \left(\sigma^2_{\ell,s} = S\ \sigma^2_{\ell,c}\right) \tag{A-15}$$

where ρ_ℓ is as defined above and r is the linear dimension of the resolution element at the target.

The primary descriptor for the phase degradation is the phase structure function $D_\phi(\rho)$ defined by

$$D_\phi(\rho) = \left\langle [\phi(\vec{r}) - \phi(\vec{r} + \vec{\rho})]^2 \right\rangle \tag{A-16}$$

where $\phi(r)$ is the phase at point r in the target or receiver plane and ρ is a displacement transverse to the propagation path. The brackets indicate a time average. For spherical wavefronts, $D_\phi(\rho)$ is given by

$$D_{\phi,s}(\rho,z) = 8\pi^2 k^2 \int_0^z dz' \int_0^\infty [1 - J_0(\frac{K\rho z'}{z})]\, \Phi_n(K,z')KdK \tag{A-17}$$

For the Kolmogorov spectrum, this reduces to

$$D_{\phi,s}(\rho,z) = 2.91\, k^2\, \rho^{5/3} \int_0^z C_n^2(z') \left(\frac{z'}{z}\right)^{5/3} dz' \qquad \text{(A-18)}$$

The corresponding formula for plane waves is

$$D_{\phi,\rho}(\rho,z) = 2.91\, k^2\, \rho^{5/3} \int_0^z C_n^2(z')dz' \qquad \text{(A-19)}$$

Another useful descriptor for the wave degradation is the mutual coherence function $M(\rho)$ which can be defined as the cross correlation of the complex radiation field normalized to its vacuum value (Ref. 13). $M(\rho)$ can be written

$$M(\rho) = e^{-1/2\, D_\phi(\rho)} \qquad \text{(A-20)}$$

where $D_\phi(\rho)$ is the phase structure function.

The separation ρ_o in the receiver plane at which $M(\rho_o) = e^{-1}$ is called the transverse coherence length and is given by

$$D_\phi(\rho_o,z) = 2 \qquad \text{(A-21)}$$

Formulae (A-20) and (A-21) are valid for all three waveforms (plane, spherical and beam), provided the appropriate phase structure function is used.

Using the Huygens-Fresnel approach, Lutomirski (Ref. 13) has shown that the total long-term beam spread for a Gaussian beam can be approximately written as

$$\theta = (\theta_0^2 + \theta_s^2)^{1/2} \qquad \text{(A-22)}$$

where θ_o is the diffraction limit spread and θ_s is caused by turbulence and can be written as

$$\theta_s = \frac{2}{k\rho_o} \tag{A-23}$$

Here, ρ_o is the transverse coherence length, and Equation (A-23) gives the value appropriate for computing the e^{-1} diameter. Since the Huygens-Fresnel approach is used in the derivation of Equation (A-22), the spherical wave structure function is used to compute ρ_o.

The short-term beam wander Φ for homogeneous turbulence (C_n^2 = constant) is given by Chiba (Ref. 26) to be

$$\Phi^2 = 21.5\, C_n^2\, z^{5/6}\, k^{1/6} \tag{A-24}$$

where Φ is defined as the e^{-2} diameter of the beam wander distribution. This formula should be approximately valid for inhomogeneous turbulence if the appropriate average value of C_n^2 is used. Since beam wander is a phase effect, we have used the phase structure function as a basis for computing the average C_n^2, obtaining

$$\overline{C}_n^2 = \frac{8}{3} \frac{\int_0^z C_n^2(z') \left(\frac{z'}{z}\right)^{5/3} dz}{z} \tag{A-25}$$

The spherical wave form of D_ϕ was used because it yields a more pessimistic value for $\overline{C}_n^2$.

Reliable predictive formulae for the short-term beam spread γ are not available, so we estimate this parameter by taking the root square difference between θ_s and Φ

$$\gamma \simeq (\theta_s^2 - \Phi^2)^{1/2} \tag{A-26}$$

This estimate is likely to break down for $\theta_s \simeq \Phi$ due to the different approximations involved in obtaining Φ and θ_s.

The short-term rms image dancing is equal to the rms angle of arrival fluctuation α, which is given by (Ref. 13)

$$\alpha = \frac{\sqrt{D_\phi(D)}}{kD} \qquad \text{(A-27)}$$

where D is the receiver diameter. The spherical wave structure function is used here.

Combining Equations (10a) and (10b) of Ref. 27, and applying a point source function, the long-term point spread function PSF is given by:

$$PSF(x) = C\, e^{-\alpha z} \int_0^D \int_0^{2\pi} M_L\left(\frac{\rho}{D}\right) M_s(\rho)\, e^{-i(k\rho x \cos\theta)/f} \rho\, d\phi\, d\rho \qquad \text{(A-28)}$$

where f and D are the lens focal length and diameter, $M_s(\rho)$ is the spherical wave mutual coherence function, and $M_L(\rho/D)$ is the lens transfer function

$$M_L(\rho/D) = \frac{2}{\pi}\left[\cos^{-1}\left(\frac{\rho}{D}\right) - \left(\frac{\rho}{D}\right)\sqrt{1 - \left(\frac{\rho}{D}\right)^2}\right] \qquad \text{(A-29)}$$

The factor $e^{-\alpha z}$ represents transmission losses.

The short-term PSF width is approximated as the root square difference between the long-term PSF width and the image dancing parameter α.

In carrying out the detailed computations, it is necessary to adopt a form for the altitude variation of C_n^2. No adequate theory exists to predict a form except at low altitudes and under specific meteorological conditions; we therefore rely heavily on measured profiles. Figure A-10 shows results obtained from AFWL (Ref. 28), summarizing airplane measurements made on several flights. Figure A-11 shows a sample profile measured from an ascending balloon (Ref. 29). C_n^2 profiles have also been inferred from stellar scintillation measurements. In arriving at a composite profile, many authors (Refs 30, 31, 32) use terms such as

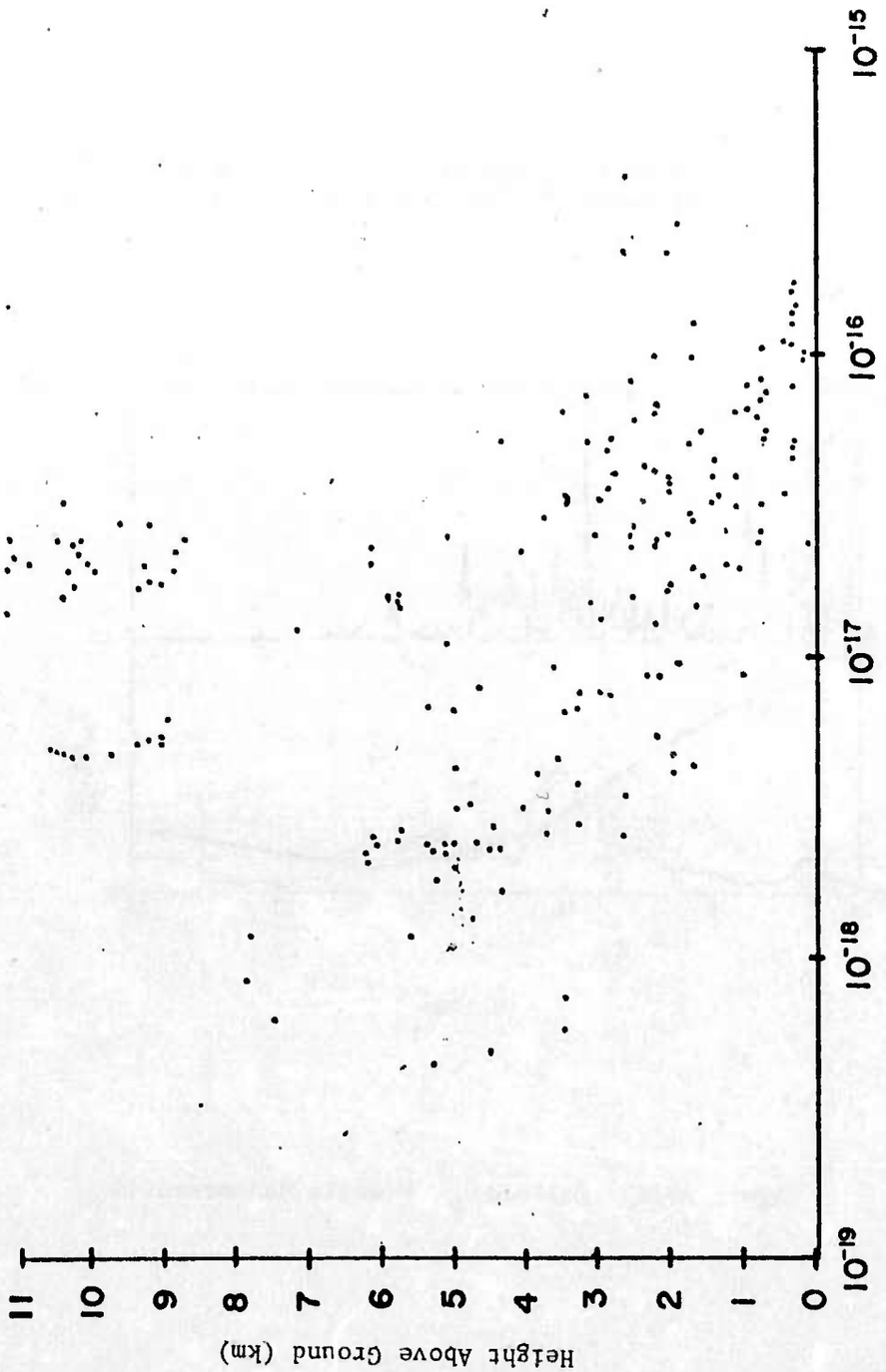

Figure A-10. Aircraft C_n^2 Measurements

Typical profiles of refractive-index structure coefficient $C_n^2(h)$, temperature T, and wind speed $|\vec{V}|$ vs. altitude h above mean sea level.

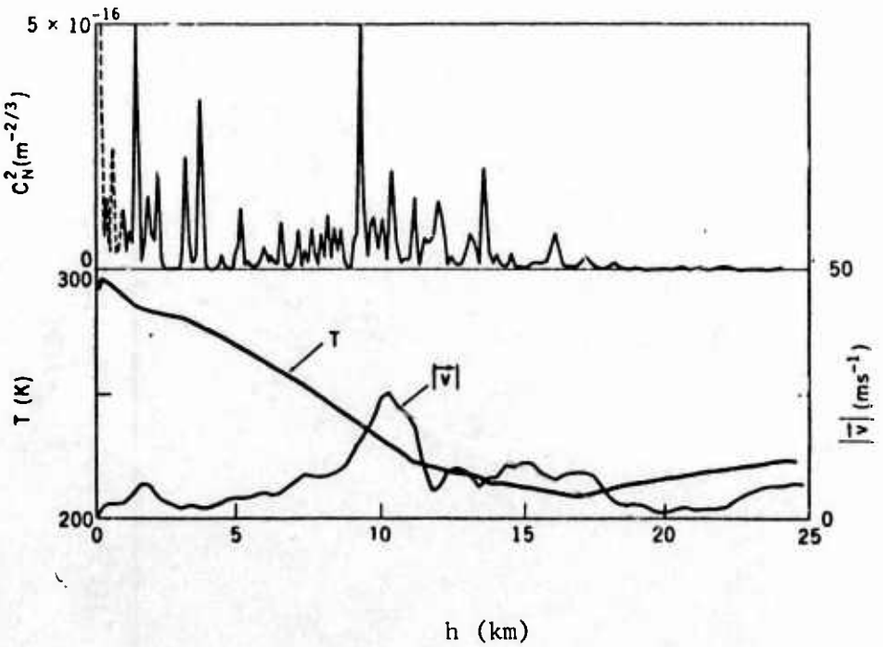

Figure A-11. Balloon C_n^2 Profile Measurements

$$C_n^2(h) \approx C_o^2 \, h^a \, e^{-h/h_o} \qquad \text{(A-30)}$$

The profile chosen for this effort is of the form

$$C_n^2(h) = K_o \, h^{-2/3} \, e^{-h/1000} + 5 \times 10^{-17} \, m^{-2/3} \qquad \text{(A-31)}$$

Here, K_o represents the ground level ($h = 1$ m) turbulence and the $-2/3$ exponent is the low level ($h \lesssim 100$ m) altitude dependence observed under neutral conditions over water. (Under meteorologically unstable conditions, a $-4/3$ exponent is more appropriate; we have chosen the more conservative exponent.) The value of $h_o = 1000$ m describes the more rapid decrease of the ground level influence at higher altitudes. The constant term $5 \times 10^{-17} \, m^{-2/3}$ is a worst-case estimate for the highly variable upper troposphere C_n^2 level. Ground level measurements generally find C_n^2 varying from $\sim 10^{-15} \, m^{-2/3}$ or less to $5 \times 10^{-13} \, m^{-2/3}$ over land, depending on the local meteorological conditions. Over sea, the upper limit is an order of magnitude lower for comparable solar flux and air temperature conditions (Ref. 33). We have chosen K_o values of 10^{-15}, 10^{-14}, and 10^{-13} for the computations.

Results

Programs for the Hewlett-Packard 9820 calculator were written to evaluate the integrals involved in the formulae. Calculations were performed for three levels of turbulence ($K_o = 10^{-13}$, 10^{-14}, 10^{-15}) and at four wavelengths ($\lambda = 0.5145$, 1.06, 3.80, and 10.6 micrometer) covering the ranges of primary interest. For the calculations, the transmitter/receiver was assumed to be at 12.2 km altitude, with the target at a slant range of 65.9 km.

For calculating scintillation in the transmitted beam, we have used the spherical wave approximation. This formula should be quite good for diverging beams, and the error should be small for collimated beams for the air-to-ground path since the strong turbulence is near the ground. (For

collimated beams propagating from ground level to the aircraft, the plane wave approximation would be more accurate.) Since we are interested in the ultimate effect of the scintillation on the target image, we have averaged the scintillation over a one-meter spot corresponding to a 15-microradian resolution element. Table A-4 shows the results, including the theoretical σ^2, the value corrected for saturation $\sigma^2(m)$, and the aperture-averaged value $\sigma^2(A)$, along with the amplitude correlation length ρ_ℓ and the resultant rms intensity fluctuation level both at a point (dB(pt)) and averaged over the one-meter spot (dB(avg)).

Table A-5 shows the short-term beam wander Φ for the air-to-ground path. Also shown is the average value of C_n^2 used in the computation for each turbulence level as computed from the phase structure function. The beam wander is given as the e^{-2} diameter of the beam position distribution.

Table A-6 gives the transverse coherence length ρ_ℓ and the resultant long-term beam spread θ_s. Beam spread values are given both at the e^{-1} diameter (θ_s) (per the formula) and at the e^{-2} diameter (θ_s') for comparison with the beam wander. We have computed θ_s' assuming a Gaussian distribution ($\theta_s' = 2\sqrt{2}\ \theta_s$). In order to make the result more general, the vacuum beam divergence has been omitted.

Table A-7 summarizes the degradations to be expected in the illuminating beam. For scintillation we include the point intensity fluctuation level (dB(pt)), the resolution element averaged fluctuation level (dB(avg)), and the amplitude correlation length ρ_ℓ. Also shown are the short-term beam wander Φ, the short-term beam spread γ, and the long-term beam spread θ_s', each given at the e^{-2} diameter of the distribution (γ is the root square difference between θ_s' and Φ).

For scintillation in the imaging leg (as well as for all other turbulence effects in the imaging leg), we use spherical wave formulae. Table A-8 shows the scintillation results, including the theoretical σ^2, the value corrected for saturation $\sigma^2(m)$, the value corrected for source

Table A-4. Illuminating Beam Scintillation over 66-km Slant Path, Free Atmosphere

K_o	λ (μm)	ρ_ℓ (cm)	σ^2	σ^2(m)	dB(pt)	σ^2(A)	dB(avg)
10^{-13}	0.5145	7.3	5.55	1.17	4.7	0.025	0.68
	1.06	10.5	2.39	0.62	3.4	0.026	0.70
	3.8	20.0	0.539	0.323	2.5	0.045	0.92
	10.6	33.3	0.163	0.132	1.6	0.040	0.87
10^{-14}	0.5145	7.3	3.41	1.09	4.5	0.023	0.66
	1.06	10.5	1.47	0.54	3.2	0.023	0.65
	3.8	20.0	0.331	0.231	2.1	0.032	0.77
	10.6	33.3	0.100	0.086	1.3	0.027	0.71
10^{-15}	0.5145	7.6	3.19	1.08	4.5	0.022	0.65
	1.06	10.5	1.37	0.52	3.1	0.022	0.65
	3.8	20.0	0.308	0.219	2.0	0.030	0.75
	10.6	33.3	0.094	0.082	1.2	0.025	0.69

Table A-5. Short-Term Beam Wander over 66-km Slant Path, Free Atmosphere

K_o	C_n^2 ($m^{-2/3}$)	λ (μm)	Φ (μrad)
10^{-13}	3.49×10^{-16}	0.5145	34
		1.06	32
		3.8	29
		10.6	27
10^{-14}	7.99×10^{-17}	0.5145	16
		1.06	15
		3.8	14
		10.6	13
10^{-15}	5.30×10^{-11}	0.5145	13
		1.06	13
		3.8	11
		10.6	10

Table A-6. Long-Term Beam Spread over 66-km Slant Path, Free Atmosphere

K_o	λ (μm)	θ_s (μrad)	θ_s' (μrad)
10^{-13}	0.5145	15	43
	1.06	13	37
	3.8	10	29
	10.6	8	23
10^{-14}	0.5145	6	18
	1.06	5	15
	3.8	4	12
	10.6	3	10
10^{-15}	0.5145	5	14
	1.06	4	12
	3.8	3	9
	10.6	3	8

Table A-7. Summary of Illuminating Beam Degradations over 66-km Slant Path, Free Atmosphere

K_o	λ (μm)	dB(pt)	dB(avg)	ρ_ℓ (cm)	ρ_o (cm)	Φ (μrad)	γ (μrad)	θ_s' (μrad)
	0.5145	4.7	0.7	7.3	1.1	34	26	43
10^{-13}	1.06	3.4	0.7	10.5	2.6	32	19	37
	3.8	2.5	0.9	20.0	12.0	29	--	29
	10.6	1.6	0.9	33.3	41.1	27	--	23
	0.5145	4.5	0.7	7.3	2.6	16	--	18
10^{-14}	1.06	3.2	0.7	10.5	6.3	15	--	15
	3.8	2.1	0.8	20.0	29.1	14	--	12
	10.6	1.3	0.7	33.3	99.4	13	--	10
	0.5145	4.5	0.7	7.3	3.4	13	--	14
10^{-15}	1.06	3.1	0.7	10.5	8.0	13	--	12
	3.8	2.0	0.8	20.0	37.2	11	--	9
	10.6	1.2	0.7	23.3	127.0	10	--	8

Table A-8. Scintillation in Imaging Leg of Active System over 66-km Slant Path, Free Atmosphere

K_o	λ (μm)	ρ_ℓ (cm)	σ^2	σ^2(m)	σ^2(s)	dB	σ^2(A)	dB
10^{-13}	0.5145	7.3	5.55	1.17	0.0026	0.22	5.0×10^{-4}	0.10
	1.06	10.5	2.39	0.62	0.0032	0.25	1.1×10^{-3}	0.14
	3.8	20.0	0.54	0.32	0.0074	0.37	4.8×10^{-3}	0.30
	10.6	33.3	0.16	0.13	0.0099	0.43	8.2×10^{-3}	0.39
10^{-14}	0.5145	7.3	3.41	1.09	0.0024	0.21	4.6×10^{-4}	0.09
	1.06	10.5	1.47	0.54	0.0028	0.23	9.2×10^{-4}	0.13
	3.8	20.0	0.33	0.23	0.0053	0.32	3.4×10^{-3}	0.25
	10.6	33.3	0.10	0.09	0.0065	0.35	5.4×10^{-3}	0.32
10^{-15}	0.5145	7.3	3.14	1.08	0.0024	0.21	4.6×10^{-4}	0.09
	1.06	10.5	1.37	0.52	0.0027	0.23	8.9×10^{-4}	0.13
	3.8	20.0	0.31	0.22	0.0050	0.31	3.2×10^{-3}	0.25
	10.6	33.3	0.09	0.08	0.0062	0.34	5.1×10^{-3}	0.31

averaging $\sigma^2(s)$, and the receiver averaged value $\sigma^2(A)$ (for a 30-cm aperture). Also shown are the amplitude correlation length ρ_ℓ and the resultant rms intensity fluctuation levels, both at a point in the receiver plane (dB(pt)) and at a point in the image (dB(avg)).

Table A-9 gives the rms image dancing computed for a one-meter receiver diameter, both at the rms radius (α) and at the e^{-2} diameter (α'). Note that this parameter is independent of wavelength.

To calculate long-term point spread functions, a f = 1.0 m, D = 30 cm diffraction-limited imaging lens was chosen. Both the diffraction limit and the turbulence degraded PSF's were computed. Figure A-12 shows typical curves (the curves are normalized to unity peak intensity). From these curves and the accompanying calculator output, the e^{-2} diameter of the diffraction limit (θ_o) and the degraded (θ_A) PSF's were obtained. These results are shown in Table A-10, along with the atmospheric degradation θ_D (root square difference between θ_A and θ_o) and the on-axis intensity reduction I/I_o. To evaluate the effect of lens diameter (f# constant) on image degradation, the PSF calculations were made for four different diameters (D = 0.15, 0.3, 0.6, and 0.9 m). Results from this calculation are shown in Table A-11 and Figure A-13.

Table A-12 summarizes the degradations to be expected in the image. For scintillation we include the intensity fluctuation level at a point in the receiver plane (dB(pt)), the fluctuation level at an image point (dB(avg)), and the amplitude correlation length ρ_ℓ. Also shown are the image dancing α', the short-term PSF width β_A, the long-term PSF width θ_A, and the diffraction limit θ_o (β is the root square difference between θ_A and α'). Again, these results are for a f = 1 m, D = 30 cm imaging lens, and the angular quantities are given at the e^{-2} diameter of the respective distributions.

Table A-9. Image Dancing over 66-km Slant Path, Free Atmosphere

K_o	α (μrad)	α' (μrad)
10^{-13}	2.4	9.6
10^{-14}	2.3	9.3
10^{-15}	2.3	9.3

Table A-10. Long-Term Point Spread Function Degradation over 66-km Slant Path, Free Atmosphere

K_o	λ (μm)	θ_O (μrad)	θ_A (μrad)	θ_D (μrad)	I/I_o
	0.5145	2.82	13.0	12.7	0.047
10^{-13}	1.06	5.81	12.8	11.4	0.208
	3.8	20.8	23.0	9.8	0.818
	10.6	58.1	58.9	9.7	0.973
	0.5145	2.82	12.6	12.3	0.050
10^{-14}	1.06	5.81	12.4	11.0	0.220
	3.8	20.8	22.9	9.5	0.827
	10.6	58.1	58.9	9.4	0.975
	0.5145	2.82	12.6	12.2	0.051
10^{-15}	1.06	5.81	12.4	10.9	0.221
	3.8	20.8	22.9	9.5	0.828
	10.6	58.1	58.8	9.3	0.975

Table A-11. Lens Diameter Dependence of Long-Term Point Spread Function Degradation over 66-km Slant Path, Free Atmosphere λ = 3.8 μm

D (cm)	θ_O (μrad)	θ_A (μrad)	θ_D (μrad)	I/I_o
15	41.6	43.0	10.9	0.936
30	20.8	23.0	9.8	0.818
60	10.4	13.8	9.1	0.564
90	6.9	11.3	8.9	0.376

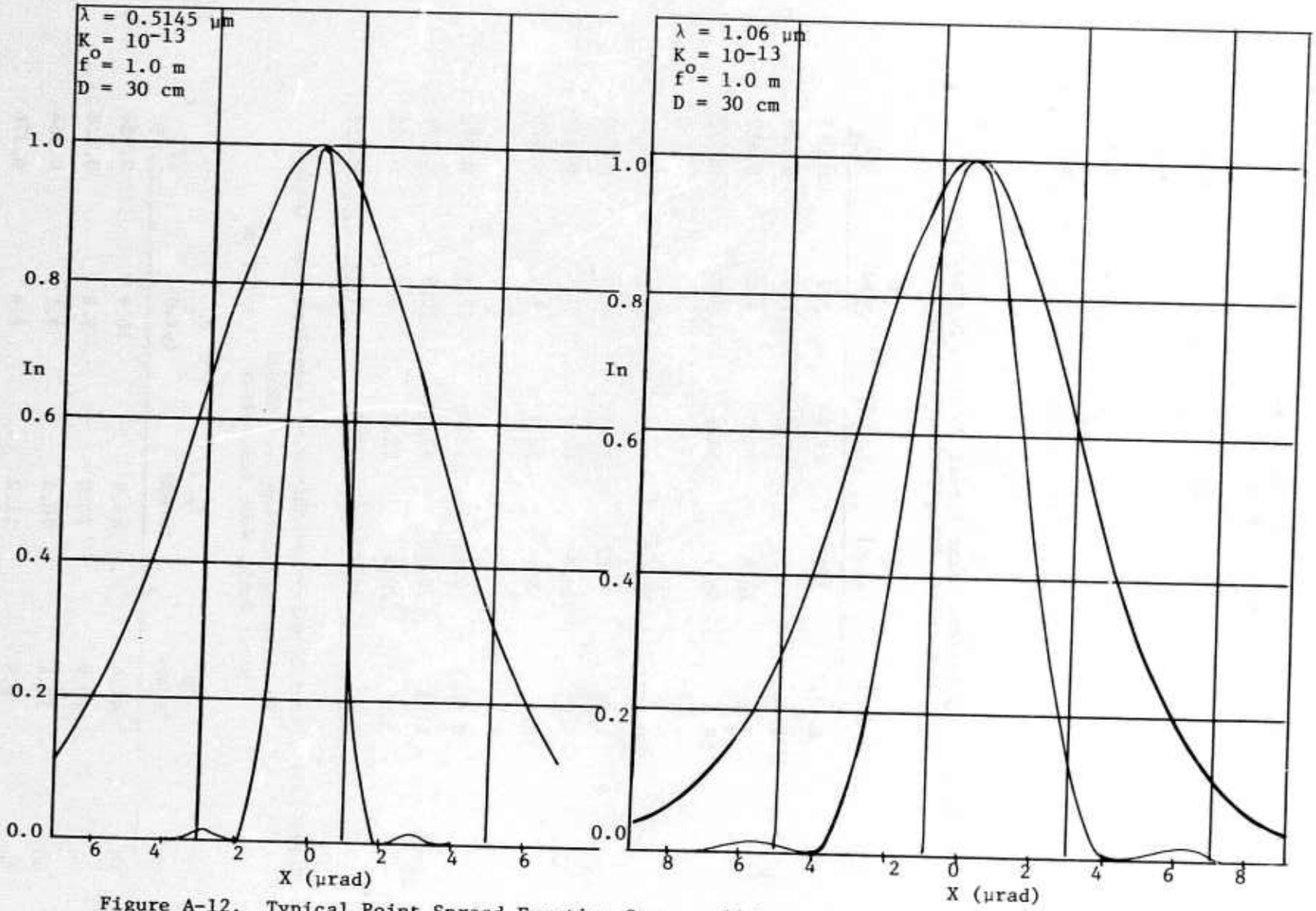

Figure A-12. Typical Point Spread Function Curves, 66-km Slant Path, Free Atmosphere

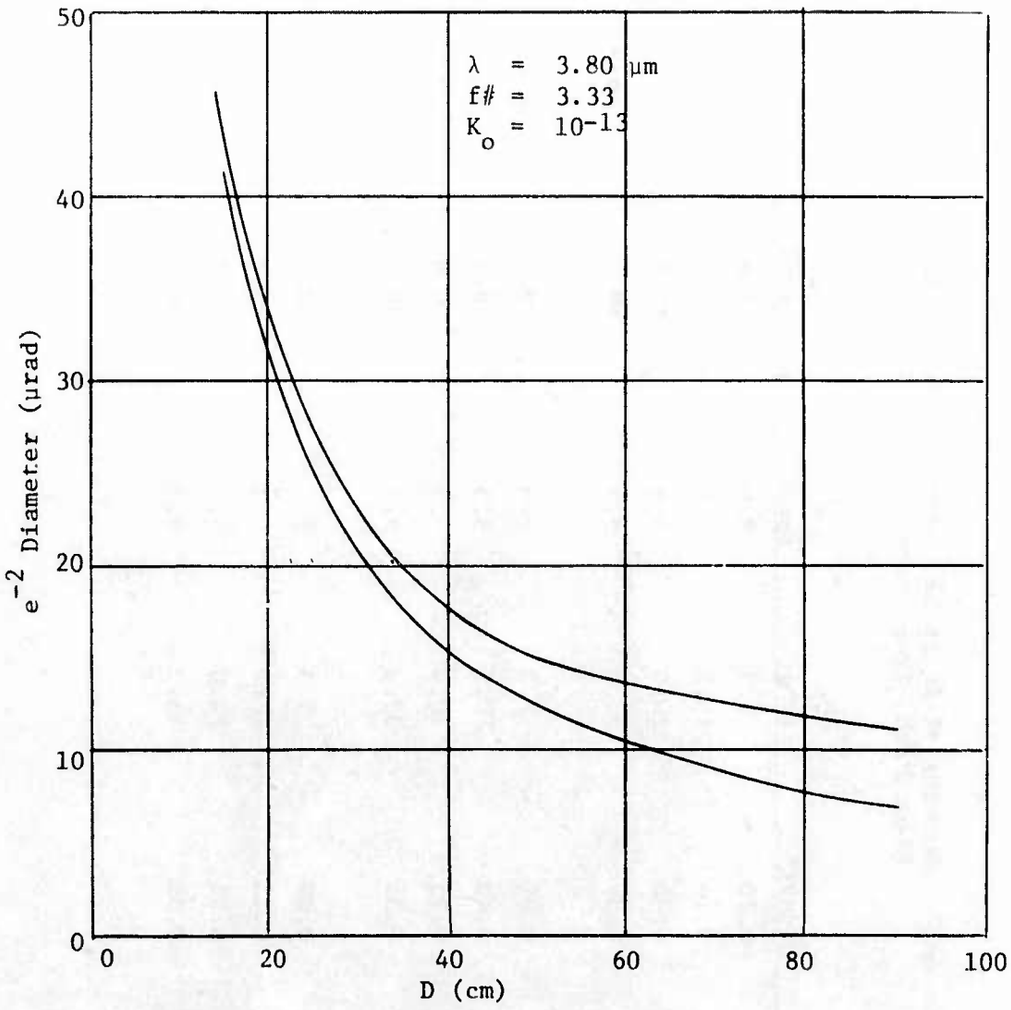

Figure A-13. Lens Diameter Dependence of Point Spread Function Degradation Over 66-km Slant Path, Free Atmosphere

Table A-12. Summary of Image Degradations over 66-km Slant Path, Free Atmosphere

K_o	λ (μm)	dB(pt)	dB(avg)	ρ_ℓ (cm)	α' (μrad)	β_A (μrad)	θ_A (μrad)	θ_0 (μrad)
10^{-13}	0.5145	0.19	0.10	7.3	9.6	8.8	13.0	2.82
	1.06	0.24	0.14	10.5	9.6	8.5	12.8	5.81
	3.8	0.52	0.30	20.0	9.6	20.9	23.0	20.8
	10.6	0.75	0.39	33.3	9.6	58.1	58.9	58.1
10^{-14}	0.5145	0.22	0.09	7.3	9.3	8.5	12.6	2.82
	1.06	0.25	0.13	10.5	9.3	8.2	12.4	5.81
	3.8	0.37	0.25	20.0	9.3	20.9	22.9	20.8
	10.6	0.43	0.32	33.3	9.3	58.4	58.9	58.1
10^{-15}	0.5145	0.22	0.09	7.3	9.3	8.5	12.6	2.82
	1.06	0.23	0.13	10.5	9.3	8.2	12.4	5.81
	3.8	0.32	0.25	20.0	9.3	20.9	22.9	20.8
	10.6	0.34	0.31	33.3	9.3	58.1	58.8	58.1

AIRCRAFT BOUNDARY LAYER OPTICAL TURBULENCE

The optical degradations introduced by propagation through the aircraft boundary layer will be qualitatively similar to those produced by the free atmosphere. We are primarily interested in the phase degradations, i.e., the wander and spread in the illuminating beam and the dancing and resolution loss in the image. Although some work has been done in the area of optical degradations produced by turbulent boundary layers (Refs 34, 35), reliable predictive equations are not generally available. We have therefore elected to utilize experimental results to obtain upper bound estimates for aircraft boundary layer degradations.

The Air Force Weapons Laboratory (AFWL) at Kirtland AFB in Albuquerque has had a comprehensive experimental investigation of turbulence degradations (including both boundary layer and free atmosphere effects) under way for some time. Although the major findings of the program are not yet published, useful preliminary results were made available to the SIS program. These results are in three areas: troposphere C_n^2 measurements (discussed previously); aircraft boundary layer degradation of finite beams; and boundary layer MTF measurements. The AFWL beam degradation data (only) carry a SECRET security classification.

The finite beam experiment (Ref. 36) involved the propagation of a 10.6-micrometer beam from the Airborne Laser Laboratory (ALL) C-135 aircraft to a target T-39 aircraft over a range of approximately 1 kilometer at various altitudes and air speeds. The beam was focused onto a target board consisting of an array of detectors whose temporal output was recorded. A simultaneous recording of the tracking and pointing errors in the ALL C-135 beam projection system was made. Analysis of the data allowed the computation of the temporal variation of both the beam centroid position and the beam diameter (as well as other parameters) for the experimental 1-kilometer path, and subsequent extrapolation to the nominal SIS 66-kilometer slant path. These results are classified SECRET, to be consistent with the AFWL data upon which they are based. To avoid classification of this appendix, those results are reported in the atmospheric optical effects section of the main body of this report.

With respect to imaging, information was received on two boundary layer MTF experiments (Ref. 37), both designed primarily to test the predictions of simple theory. This theory predicts that the MTF has the form

$$\text{MTF} = \exp -\left[\alpha k^2 \left(\frac{f^2}{f_o^2 + f^2}\right)\right]$$

where k is the wave number, f_o^2 is the spatial frequency associated with the dominant turbulence scale, and α is a strength parameter which is proportional to the dynamic pressure. The line spread function is then predicted to show saturation at apertures large compared with the dominant scale size and should have a considerable wavelength dependence. In the first experiment a 0.6328 micrometer beam was propagated twice through the turbulent boundary layer surrounding a specially fitted NASA Lear Jet in flight. Both the line spread function (LSF) and the MTF were measured at a variety of air speeds and altitudes and for beam diameters between 10 and 24 mm. In some measurements an aerodynamic fence was placed in the airstream ahead of the propagation path. The LSF degradation as measured by the peak intensity relative to the non-degraded peak intensity (I/I_o) was between 0.73 and 0.86 micrometer (one way) for all runs without the fence. With the fence, values as low as 0.55 micrometer were reported. The expected dependence on dynamic pressure (altitude and air speed) was present only when the fence was used. The LSF saturation with aperture size was not observed even though the 24-mm aperture was considerably larger than the estimated 4.8-mm dominant scale size. The fence, often used to quiesce flows around open ports, resulted in significantly smaller degradation.

The second MTF experiment was performed in a wind tunnel and was designed to investigate further the wavelength and aperture dependence. Although analysis is not complete, preliminary results were made available which verified the predicted wavelength scaling (from 0.488 to 1.06 micrometer) and which showed aperture saturation for 35 mm beams.

In order to use the results from these experiments in obtaining estimates of boundary layer image degradation, we assume that aperture saturation takes place at all wavelengths before 40 mm. (This seems reasonable since boundary layers are typically 5 cm thick.) Scaling the Lear Jet data to 40 mm, degradations of 0.45 should be expected at 0.6328 micrometer.

Using a $\frac{1 - e^{-(a/\lambda)^2}}{(a/\lambda)^2}$ wavelength dependence (approximately valid for the free atmosphere), we compute I/I_o values of 0.33, 0.73, 0.97, and 0.99 for 0.5145, 1.06, 3.8, and 10.6 micrometers respectively.

COMBINED RESULTS: FREE ATMOSPHERE AND AIRCRAFT BOUNDARY LAYER TURBULENCE

For the case of an illumination beam, the results are classified and are therefore reported in the body of this report.

For the imaging case, we can combine the boundary layer PSF degradation by taking the product of the I/I_o ratios for the boundary layer and the free atmsophere and then computing resultant PSF widths. Table A-13 shows the total estimated image degradation for a f = 1 m, D = 30 cm lens, including the scintillation level in the image plane (dB(avg)), the image dancing α_T, the short-term PSF width β_T, the long-term PSF width θ_r, and the lens diffraction limit θ_o.

Table A-13. Combined Image Degradation

K_o	λ (μm)	dB(avg)	α_T (μrad)	β_T (μrad)	θ_r (μrad)	θ_0 (μrad)
10^{-13}	0.5145	0.10	9.6	21	23	2.82
	1.06	0.14	9.6	11	15	5.31
	3.8	0.30	9.6	21	23	20.8
	10.6	0.39	9.6	58	59	58.1
10^{-14}	0.5145	0.09	9.3	20	22	2.82
	1.06	0.13	9.3	11	14	5.81
	3.8	0.25	9.3	21	23	20.8
	10.6	0.32	9.3	58	59	58.1
10^{-15}	0.5145	0.09	9.3	20	22	2.82
	1.06	0.13	9.3	11	14	5.81
	3.8	0.25	9.3	21	23	20.8
	10.6	0.31	9.3	58	59	58.1

Section A-5

ATMOSPHERIC AEROSOL ATTENUATION OVER 66-KM SLANT PATH

(Summary of current data and analysis)

ATTENUATION COEFFICIENTS*

Figure A-14 is a graph of aerosol attenuation coefficients for AFCRL atmospheric aerosol models, at sea level, for a normalized "clear" atmosphere (for which the standard visibility range is 23 kilometers).

The solid curve is plotted from tabulated values taken fromthe AFCRL "Optical Properties of the Atmosphere" report (Ref. 1), and is consistent with Figure 22 of that report. That curve is also reflected in the aerosol coefficient tabulations of other reports of the 1972 era (e.g., AFCRL-72-0312 (Ref. 7) and AFCRL-72-0611 (Ref. 4)) and in the atmospheric transmittance computer program LOWTRAN 2, AFCRL-72-0745 (Ref. 2).

The dotted curve marked by x's was plotted from tabled values (Ref. 19) supplied to SRL by AFCRL. That curve represents AFCRL's revised model for an "average continental aerosol," based upon a great deal of experimental measurements and analysis during the 1972-74 time period. The revised data are reflected in Figure 2 of AFCRL-TR-74-0003 (Ref. 3) but are not yet published in coefficient tables comparable to those of the earlier reports. They do, however, appear in the aerosol spectral data listing in Computer Code LOWTRAN 3 (Ref. 8), recently published by AFCRL.

The dotted curve of Figure A-14 marked by small circles represents an AFCRL estimate of an "average maritime aerosol," according to tabulated values (Ref. 20) supplied to us by AFCRL. The data are the "sea level" values applicable to the "exchange layer" or transition region between the ocean surface "boundary layer" and the "upper atmosphere," for a 60% salt spray, 40% continental aerosol mixture. Depending upon sea state and weather (including recent weather history), the exchange layer may be from

* Some of the ideas expressed here and in the subsection following (entitled "Status of Models") are based upon personal discussions during a visit to AFCRL (see Ref. 38).

1 to 5 kilometers in depth. In this region, the atmospheric aerosol characteristics are considered to transition from a predominantly marine type in the lower part to a predominantly continental type at the top. During periods of low wind and a relatively calm sea, salt particles and salt water droplets drift downward and effectively lower the top of the marine aerosol region.

The plotted curves are for a relative humidity of 75%. However, the variation with relative humidity is negligible for continental aerosols, but is significant for marine aerosols. This is due to the hygroscopic nature of salt: at low values of R.H., atmospheric salt content consists primarily of solid particles; at high values of R.H., much of the atmospheric salt exists as salt water droplets, with differing optical properties.

STATUS OF MODELS

The plotted (1974) continental aerosol values are based upon many measurements of atmospheric aerosol particle sizes, chemical determination of constituent materials, and measurement of the complex index of refraction of those materials. Additionally, optical measurements of scattering and attenuation using laser sources have confirmed the accuracy of the plotted results at representative points throughout the spectrum. In brief, that curve is rather well established.

In contrast, the data points on the marine aerosol curve are calculated values based upon very sketchy data about marine atmospheres. Experimental verification is virtually non-existent, and the statistical variations with time, altitude and location are almost entirely unknown. In brief, the marine aerosol model constitutes a "best guess"--a good starting point to serve as a basis for the additional research and experimentation required to establish a valid data base.

APPLICATION TO SIS SLANT PATH AEROSOL PARTIAL TRANSMITTANCE ESTIMATES

In view of the status of the current marine aerosol model, the reader is cautioned to consider the following results as rather preliminary (but

the best that can be done at this time). The cited "average continental" and "estimated marine" models were employed to calculate the results reported briefly below and on the accompanying graphs.

Figure A-15 is a graph of aerosol transmittance versus wavelength for a 66-kilometer slant path, based upon the revised aerosol coefficients of Figure A-14, calculated for a normalized "clear" atmosphere, for which the sea level visibility range is 23 kilometers (for each model). The solid curve is for the revised "average continental aerosol model" and the dotted curve assumes that the estimated marine aerosol model (60% sea spray, 40% continental aerosols) exists over the whole path, which, from our conversations with AFCRL, is an unlikely situation. The dashed curve is for a "composite" situation in which the marine aerosol model is assumed for the first kilometer of altitude and the average continental model is assumed for the remainder of the path. This is considered (postulated, really) to represent approximately a "worst case" with respect to atmospheric aerosol content.

Figure A-16 is a similar presentation for a normalized "hazy" atmosphere, for which the sea level visibility range is 5 kilometers for each model. The sea level aerosol concentration is 4.87 times the "clear" value, with a decreasing ratio between the two as altitude increases. Above 5 kilometers, the two are identical in the models.

Figure A-17 is a similar presentation for SRL's normalized "light haze" atmosphere, for which the sea level visibility is 10.8 km. The sea level aerosol concentration for this visibility is the geometric mean of the "clear" and "hazy" values, or 2.2 times the "clear" value ($2.2 = \sqrt{4.87 \times 1}$).

Figures A-18, 19, and 20 present the same curves as in Figures A-15, 16, and 17, but the curves are grouped to compare "clear", "light haze" and "hazy" transmittance for each aerosol type in lieu of the previous presentation.

METHOD OF COMPUTATION

Since altitude variation tables are not currently available for the revised continental and new marine models, it was necessary to synthesize the required "optical depth" values from which to calculate aerosol transmittance values for the slant path. This was accomplished in the following manner, based upon the essential linearity of the aerosol attenuation process:

(1) It was determined, from data tables in AFCRL-72-0497 (Ref. 1), that the equivalent sea level path length (ESLPL) of a 0-1 km vertical path for a "clear" atmosphere is 0.664 km, and the ESLPL of a 1-12 km vertical path is 0.656 km. Similarly, for a normalized "hazy" atmosphere the ESLPL for 0-1 km is 0.604 km, and for 1-12 km it is 0.373 km.

(2) Then for our 66-kilometer slant path, the respective ESLPL's are just the above values multipled by the secant of the path zenith angle (secant $79.35^{o} = 5.41$). Hence, for an all-continental or all-marine atmosphere, the slant path optical depth values are, for a "clear" atmosphere:

$$OD = (0.664 + 0.656)5.41\ \gamma_a = 7.14\ \gamma_a$$

For a normalized "hazy" atmosphere, the slant path "optical depth" is:

$$OD = (0.604 + 0.373)(4.87)(5.41)\ \gamma_a = 25.7\ \gamma_a,$$

where γ_a is the "clear" sea level value.

(3) For the "composite" atmosphere the two assumed layers are considered separately, according to the following:

For normalized "clear":

$$OD = (0.664\ \gamma_a^{M} + 0.656\ \gamma_a^{C})5.41$$

where γ_a^M and γ_a^C are the sea level coefficient values for the marine and continental aerosols, respectively.

For normalized "hazy":

$$OD = [(0.604 \times 4.87\ \gamma_a^M) + (0.373 \times 4.87\ \gamma_a^C)]5.41$$

$$= (2.94\ \gamma_a^M + 1.817\ \gamma_a^C)5.41$$

(4) For a "light haze" atmosphere, the optical depth at each wavelength was taken as the geometric mean of the "clear" and "hazy" values. This is consistent with a sea level aerosol concentration of 2.2 times the "clear" value, where the hazy value is 4.87 times the clear value, with comparable scaling for each altitude increment.

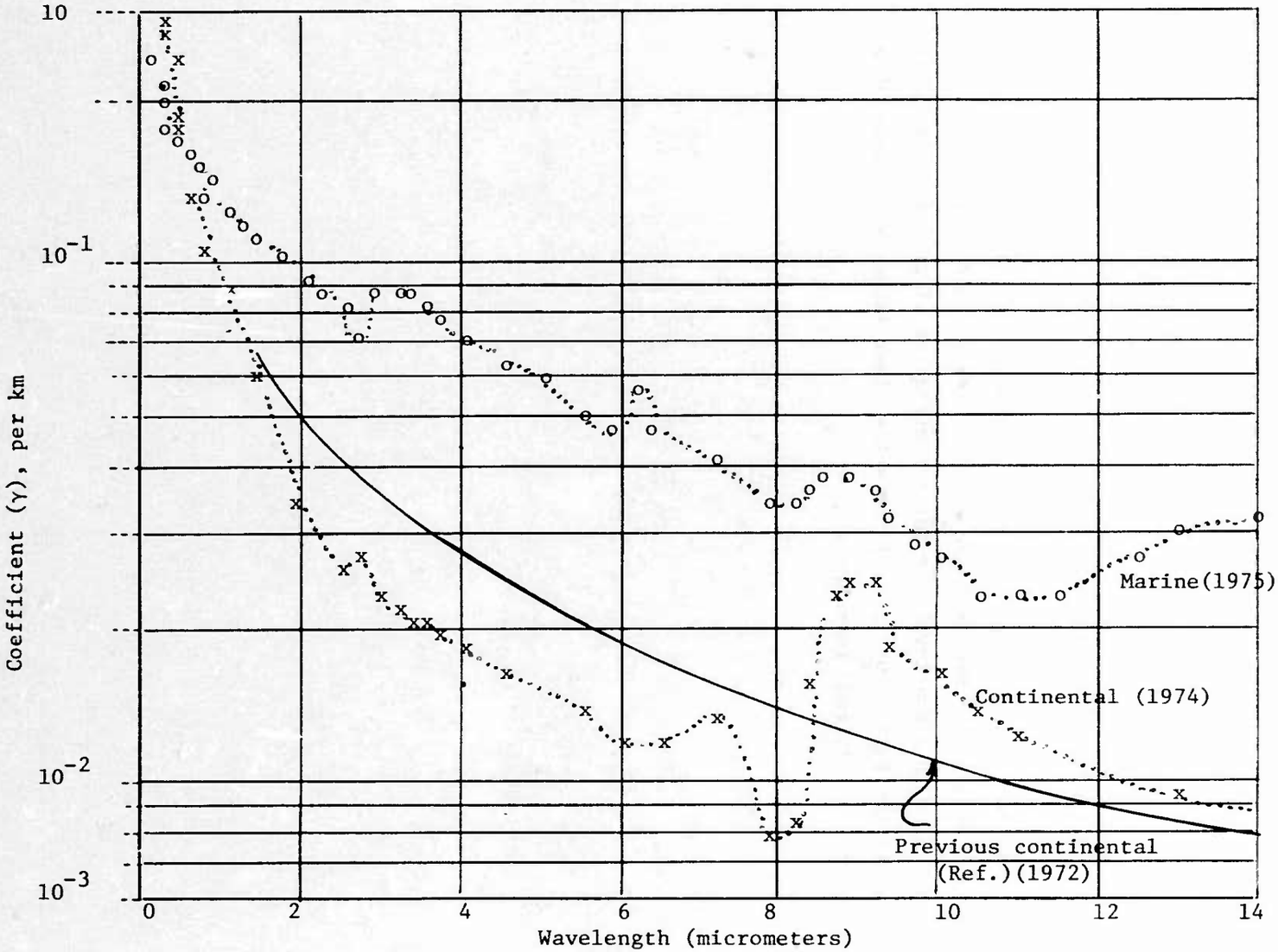

Figure A-14. Aerosol Attenuation Coefficients (Average Atmosphere Models) (Clear)

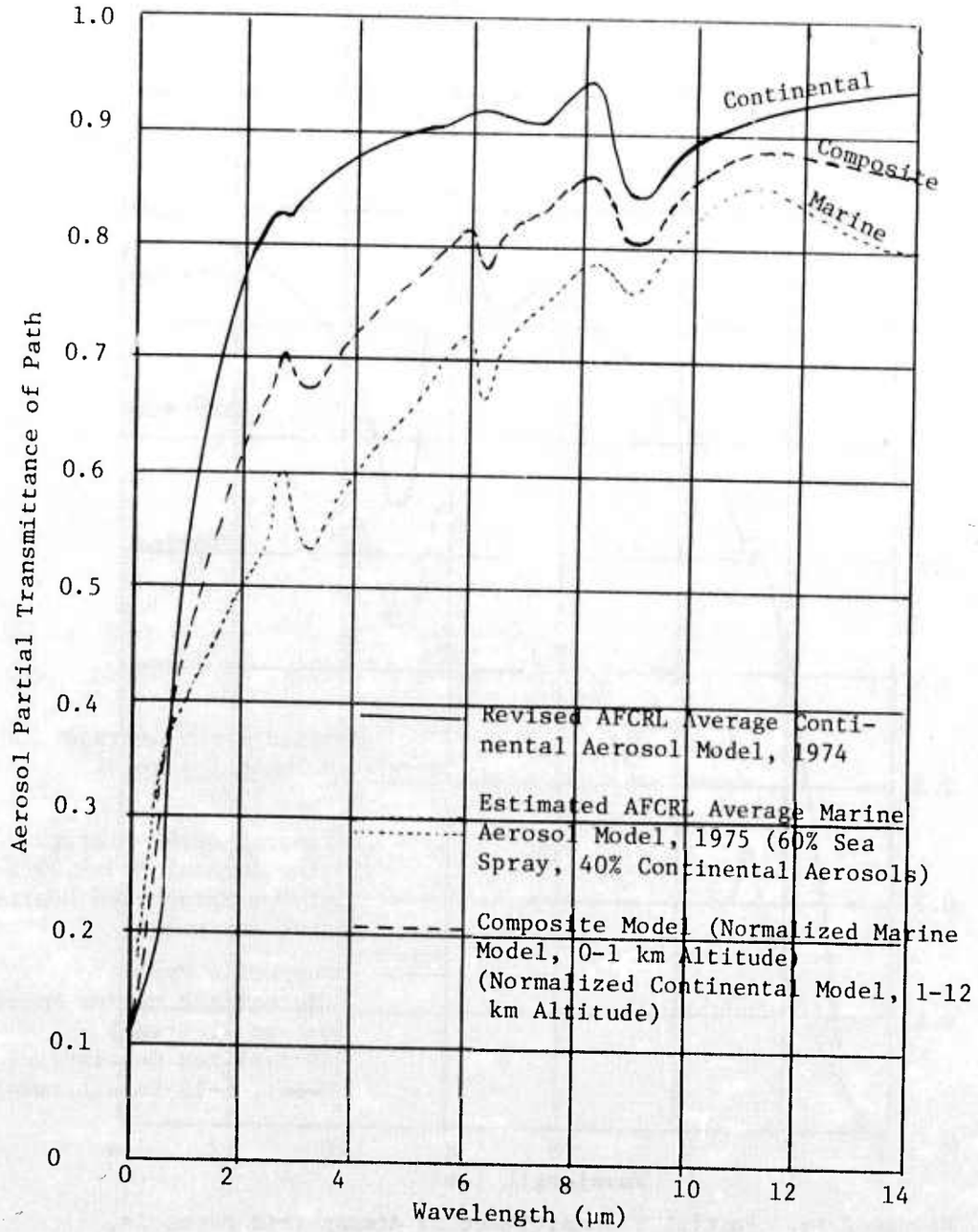

Figure A-15. Partial Transmittance of Atmospheric Aerosols, 0 to 40,000 ft, 35 nmi Slant Path (0-12.19 km, 64.82 km, 66 km Slant Range), Normalized "Clear" Atmosphere

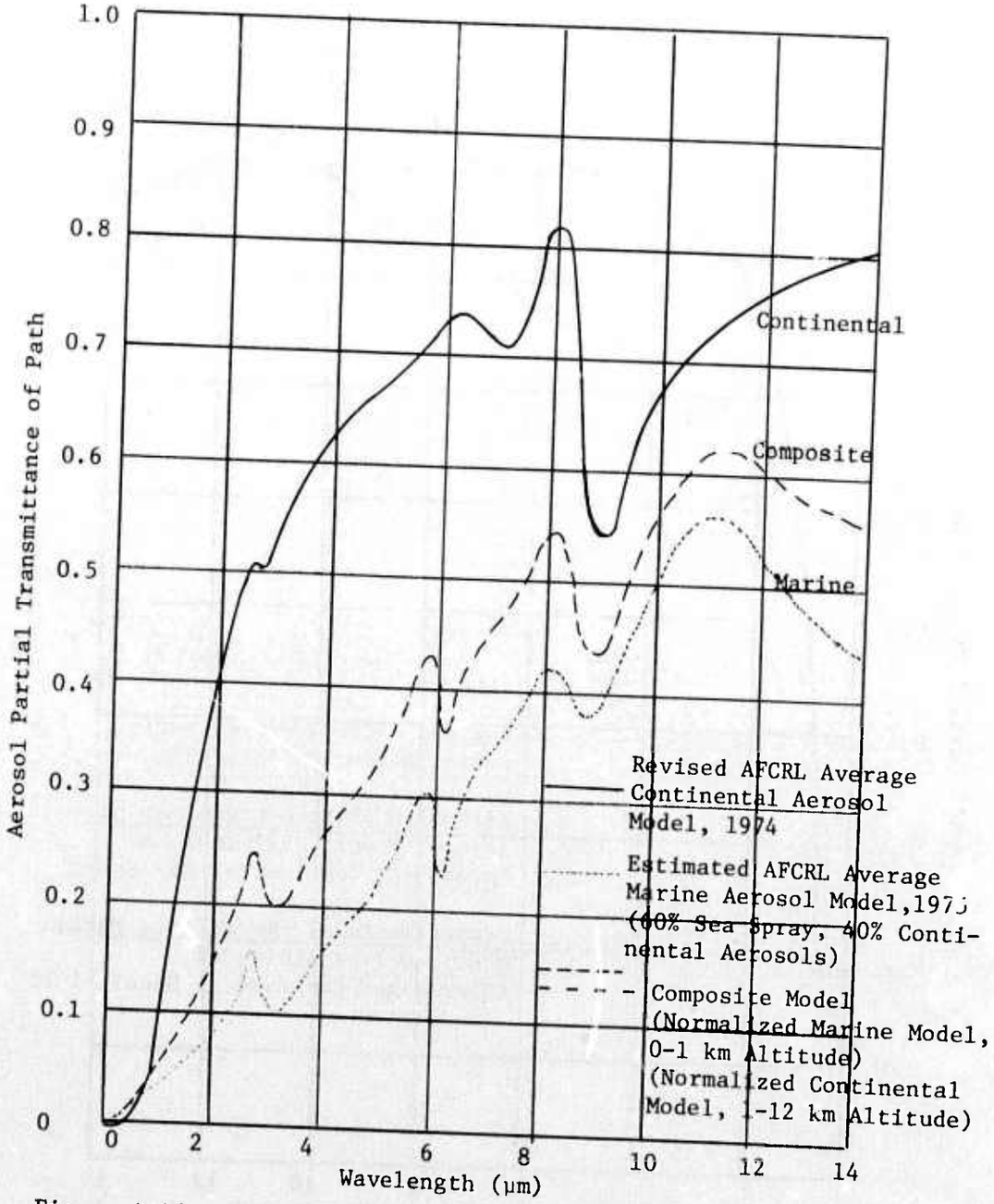

Figure A-16. Partial Transmittance of Atmospheric Aerosols, 0 to 40,000 ft, 35 nmi Slant Path (0-12.19 km, 64.82 km, 66 km Slant Range), Normalized "Hazy" Atmosphere

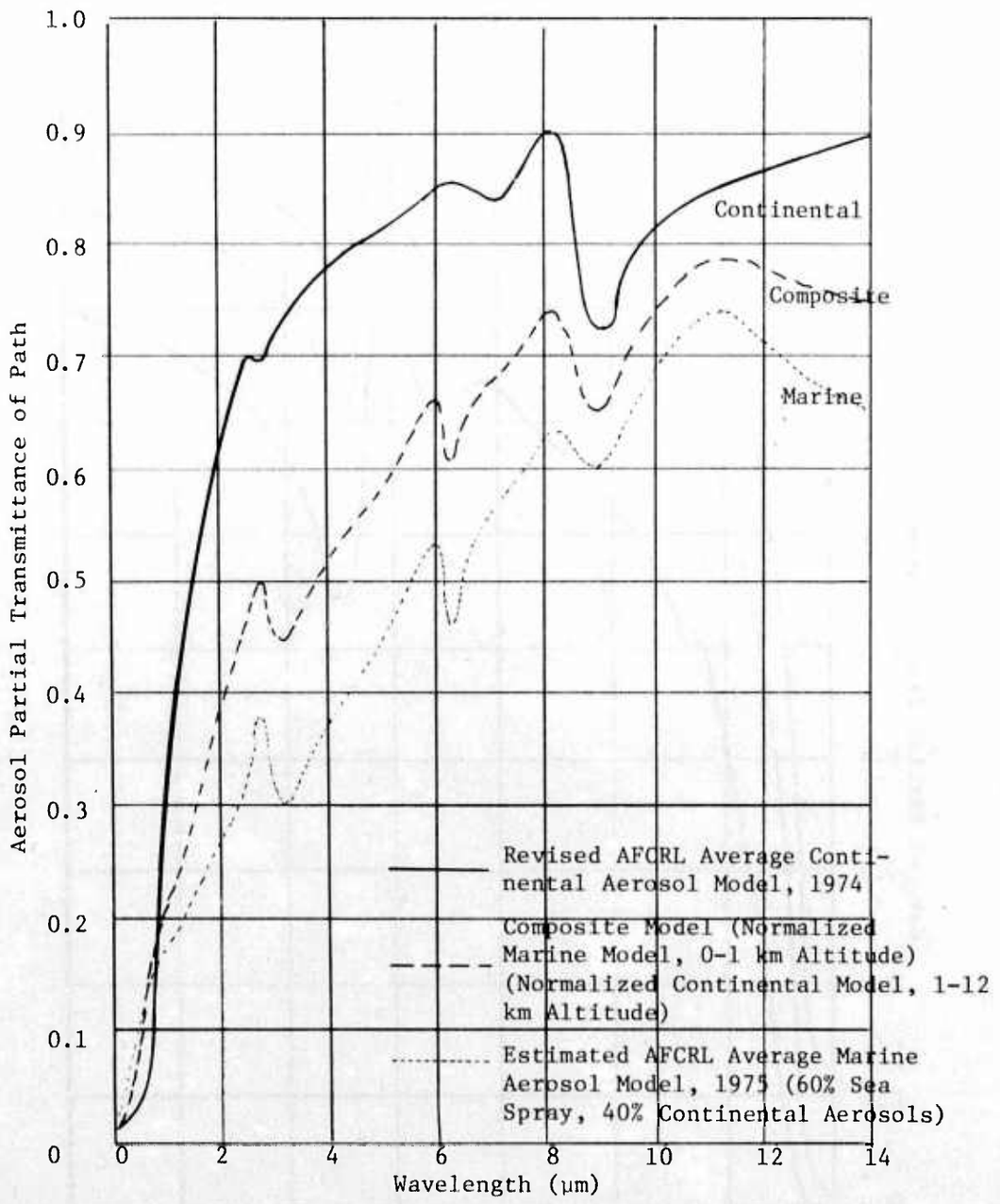

Figure A-17. Partial Transmittance of Atmospheric Aerosols, 0 to 40,000 ft, 35 nmi Slant Path (0-12.19 km, 64.82 km, 66 km Slant Range), Normalized "Light Haze" Atmosphere

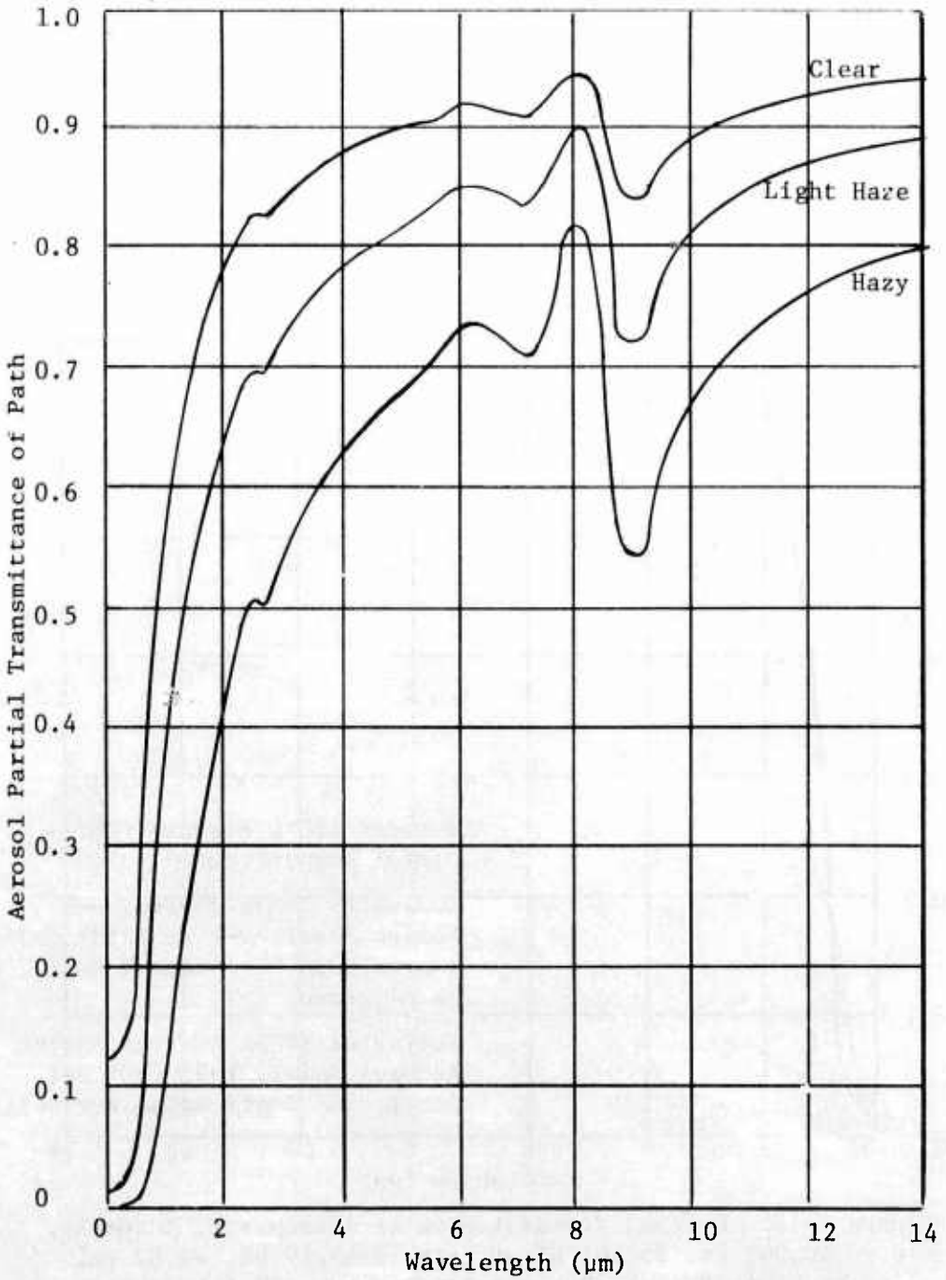

Figure A-18. Partial Transmittance of Atmospheric Aerosols, 0 to 40,000 ft, 35 nmi Slant Path, Average Continental Aerosol Model

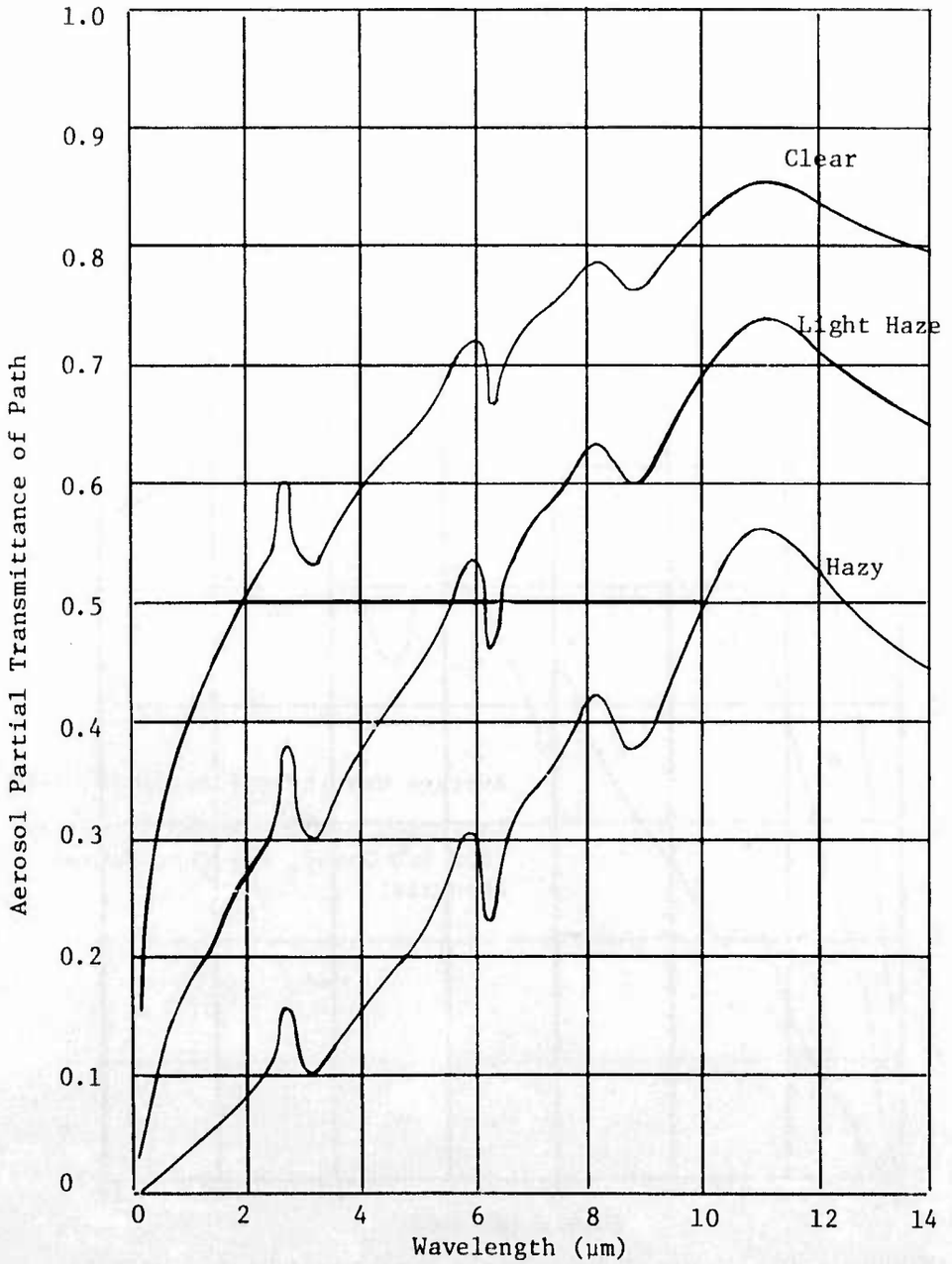

Figure A-19. Partial Transmittance of Atmospheric Aerosols, 0 to 40,000 ft, 35 nmi Slant Path, Estimated Marine Aerosol Model

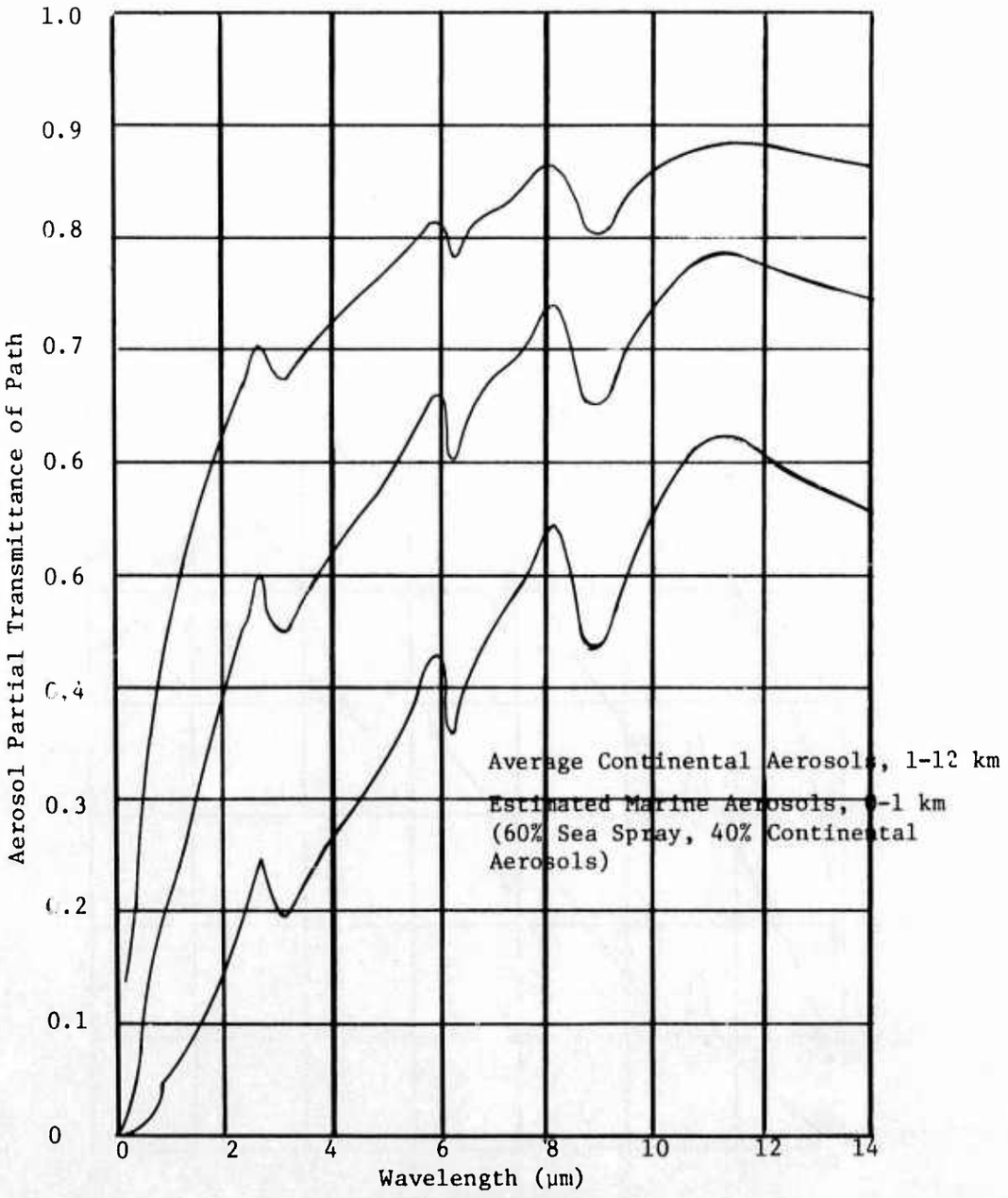

Figure A-20. Partial Transmittance of Atmospheric Aerosols, 0 to 40,000 ft, 35 nmi Slant Path, Composite Aerosol Model

Section A-6

COMPUTER-CALCULATED BAND TRANSMITTANCE CURVES FOR SIS 66-KILOMETER SLANT PATH

INTRODUCTION

This section consists of 70 computer-generated plots of atmospheric transmittance, calculated for the SIS nominal 66-kilometer slant path. The plots are arranged in six sets, of which the first three utilize AFCRL's "average continental aerosol model" of 1974, and the other three utilize AFCRL's "estimated marine aerosol model" of 1975 (60% sea spray). One of the three wavelength regions is covered in each set, with the wavelength regions designated as Visible and Near IR, Mid-Range IR, and Long-Wave IR. A wide spectrum of atmospheric conditions is represented by the use of AFCRL's five latitude-season models and two atmospheric haze models ("clear) and "hazy"), with an intermediate haze level ("light haze") also included in the Visible and Near IR wavelength region.

The "marine aerosol" sets were included to show the possible effects of sea spray in the atmosphere. However, the uncertainties of the marine aerosol model, as discussed previously, dictate cautious use of the marine results. Also, the marine aerosol plots assume a 60% sea spray aerosol throughout, likely a very pessimistic assumption. (The relative influence of a "composite" aerosol, with sea spray only in a lower layer, was shown previously.)

These LOWTRAN plots may be used to get a general view of band transmittance over the wavelength region depicted, and the variation with atmospheric model and aerosol (haze) concentration. Sets I and IV can be used, also, to estimate laser transmittance at visible wavelengths and at 1.06 micrometer (because of the absence of strong molecular absorption lines in the vicinity). However, the plots will <u>not</u> give accurate estimates for DF laser lines, CO_2 lines, or other laser frequencies in regions having strong molecular resonance absorption lines. The reason is that LOWTRAN is a band transmittance model; it computes the average transmittance over an interval of 20 wave-numbers. The transmittance of a particular laser line having

a frequency within that interval may be somewhat above or from a little to far below this average, depending upon the position of its frequency on a high-resolution plot of the spectral transmittance in the interval. Such monochromatic transmittances may be readily calculated manually for those laser lines for which accurate attenuation coefficients have been computed and validated.

NOTE: A recent research report (Ref. 39) revises the previous estimates of water vapor continuum absorption in the 8 to 13 micrometer wavelength region, and includes a temperature dependence not previously established. The new data was incorporated into the LOWTRAN 3 program, for some computer-calculated runs on another AFAL program, and significant differences in the results were found. It was then decided to rerun the previously generated SIS LOWTRAN 3 curves (of August-September 1975) with the cited program changes, and the graphs of this appendix are based upon the resulting "Modified LOWTRAN 3" computer program.

The curves were run on the ASD central computer facility during April 1976, using the terminal in Building 22B and the Cal-Comp plotter in Building 22. The graphs reproduced herein were reduced 50% in size from the originals to facilitate publication.

The wavelength region of interest was divided into three bands for these runs, with the following intervals covered: (1) 0.3 to 1.85 micrometers, (2) 1.85 to 5.5 micrometers, and (3) 7.1 to 14.3 micrometers. The wavelength region from 5.5 to 7.1 micrometers was not computed because it is known to be opaque for low altitude atmospheric distances of more than a few hundred meters.

The above cited wavelength intervals are approximate. The LOWTRAN computer code used employs frequency (wave numbers per centimeter) rather than wavelength, and computes the average transmittance over 20 wave-number intervals. The specific frequency regions employed for the three cited bands, and the computation intervals employed, were as follows:

1. 5400 to 34,000 cm^{-1} (1.852 to 0.294 micrometers)
   $\Delta\nu$ = 20 cm^{-1}, 5400 cm^{-1} to 15,000 cm^{-1}
   $\Delta\nu$ = 200 cm^{-1}, 15,000 cm^{-1} to 34,000 cm^{-1}

2. 1800 to 5400 cm^{-1} (5.555 to 1.852 micrometers)
   $\Delta\nu$ = 10 cm^{-1}

3. 700 to 1400 cm^{-1} (14,286 to 7.143 micrometers)
   $\Delta\nu$ = 5 cm^{-1}

The differing computation frequency intervals were chosen to minimize computer and printout time while preserving adequate resolution in the graphs.

For each wavelength region there are five pages of graphs for each aerosol type (continental and marine). Each page shows the transmittance plots for one of five latitude-season atmosphere models, at each of two or three haze levels, keyed to visibility range. For the visible/near IR wavelength region three normalized haze levels ("clear," "light haze" and "hazy") are shown, for which the sea level visibility ranges are 23, 10.8, and 5 kilometers, respectively. For the other two wavelength regions, only "clear" and "hazy" graphs are shown because the transmittance variation with haze level is relatively small in these regions. The specific aerosol distributions making up the normalized "clear" and "hazy" atmospheric haze models are described in Ref. 1. The aerosol particle concentration in SRL's "light haze" model is the geometric mean of the other two concentrations, so that the sea level aerosol concentrations are in the ratio of 1, 2.2, and 4.87 respectively, for "clear," "light haze" and "hazy" atmospheres.

LATITUDE-SEASON MODELS

The model atmospheres used as the basis for LOWTRAN computations are given in Ref. 1. Sea level values of major variables having a significant influence on the LOWTRAN results are reported in Table A-14.

Table A-14. Principal Variables in Model Atmosphere

	Subarctic Winter Model	Mid-Lat. Winter Model	Subarctic Summer Model	Mid-Lat. Summer Model	Tropical Model
Pressure (mb)	1013	1018	1010	1013	1013
Temperature	-15.9°C	-0.8°C	14°C	21°C	27°C
Density (gm/m^3)	1372	1301	1220	1191	1167
Water vapor (gm/m^3)	1.2	3.5	9.1	14	19
Ozone ($\mu gm/m^3$)	41	60	49	60	56
CO_2 (ppm)	330	330	330	330	330

LOWTRAN 2, LOWTRAN 3, AND MODIFIED LOWTRAN 3

LOWTRAN 2 (Ref. 2) is an atmospheric transmittance computer model that has been widely used during the past three or four years. In August and September 1975 LOWTRAN 2 was employed for slant path transmittance calculations for the SIS nominal 66-kilometer slant path. In so doing, the following revisions were made in the basic program and data file:

1. Values in the H_2O spectral data table were changed per an update received from AFCRL on 3 March 1975.

2. The aerosol attenuation function was deleted and tabulated coefficient values for AFCRL's Average Continental Aerosol Model (1974, Ref. 19) and Estimated Marine Aerosol Model (1975, Rer. 20) were substituted, with provision for selecting either model at the start of a run. [The Average Continental Aerosol Model is now included in LOWTRAN 3 (Ref. 8).]

3. Provisions were made for employing several computation intervals on a single run, for different wavelength intervals.

A linear interpretation routine was employed with the aerosol table, and other appropriate changes were made to accomplish items 2 and 3 above.

In making the runs for this report an additional change was incorporated in the program: The ozone spectral data table of LOWTRAN 2 was revised to include changes made in the recently published report on LOWTRAN 3 (Ref.8).

It is understood, from discussion with the principal author/researcher and the LOWTRAN computer programmer at AFCRL, that incorporation of the above-cited changes into LOWTRAN 2 effectively convert it to LOWTRAN 3 for most applications, and we have labelled the graphs of this report accordingly. (The published LOWTRAN 3 also incorporates numerous other changes, mostly to make the program more flexible and useful for a wider range of applications.)

"Modified LOWTRAN 3" is SRL's term for a program that results from a change in the 8-13 micrometer water vapor continuum absorption computation in LOWTRAN. This change is made to incorporate recent research findings reported in a technical paper (Ref. 39) presented at the St. Louis IRIS meeting on 3 February 1976. The required program changes were obtained by phone from Mr. Jim Chetwynd, AFCRL LOWTRAN programmer, on 5 February 1976, with first-order verification by SRL. They remain to be officially verified, however, in a formal AFCRL document.

COMMENTS ON RESULTS

The first page of Set I graphs shows the rapid drop-off of transmittance at the short wavelength end of the visible region due to ozone continuum absorption and molecular scattering. It also shows the influence of strong molecular resonance absorption in a number of near-IR wavelength regions beginning at the top end of the visible region at 0.691 micrometer. In comparing the three curves of that page, the very strong influence of atmospheric haze level upon visible wavelengths is apparent, as is the decreasing effect of this factor in the near IR.

The remaining pages of Set I exhibit only small changes, showing the relatively negligible influence of latitude and season upon visible and

near IR wavelengths. (Note the difference in amplitude of some of the structure, however; e.g., the spike at 1.45 micrometer, and the width of the 1.4 to 1.8 micrometer window.)

The first page of Set II shows, for the 66-kilometer path, the three prominent windows in the mid-IR region. Comparison of the three curves shows the reduced influence of atmospheric haze in this wavelength region, as compared to the visible and near IR region of the previous graphs.

The remaining four pages of Set II show substantial changes, illustrating the relatively greater influence of latitude-season variables upon atmospheric transmittance in this region. The amount of atmospheric water vapor (absolute humidity) accounts for the major differences in results between the five latitude-season models, with the largest difference being at the longer wavelengths. The relatively good transmittance of the 2.1-2.3 micrometer and 3.5-4 micrometer atmospheric windows, over a wide range of atmospheric variables, is an important feature shown by the five pages of Set II.

Set III shows the wide IR window from about 8 to about 14 micrometers, most often used for passive thermal imaging. The ozone absorption band between 9 and 10 micrometers is evident; however, the major absorber is water vapor, with CO_2 also significant. The two curves of each page show the relatively small influence of atmospheric haze upon this wavelength region.

The five pages of Set III illustrate the large influence of latitude-season variables in this region. The chief constituent responsible for the large variation is water vapor content. Because of this influence, and the large dependence of atmospheric water vapor capacity upon air temperature, high values of transmittance are most likely in cold weather and low values are most likely in warm weather. The temperature itself has an influence upon the optical absorption of molecular constituents, as evidenced in several references (e.g., Refs 14 and 20), and this influence is reflected in the revised water vapor continuum absorption incorporated into "Modified LOWTRAN 3."

Sets IV, V, and VI duplicate Sets I, II, and III, respectively, but with the AFCRL Estimated Marine Aerosol Model (Ref. 20) data table substituted for the continental aerosol model table. The major influence of the sea spray in the marine model is seen to be a much reduced average transmittance in the near and mid-IR regions, as one would predict from the data of Section V of this report. The reader is again cautioned, however, of the uncertainties in the marine aerosol model and the likely great variability in over-ocean aerosols (as compared to continental aerosols) resulting from sea state and weather variables. The marine aerosol LOWTRAN curves may present an overly-pessimistic picture except for the most severe conditions.

Set I (LOWTRAN 3)

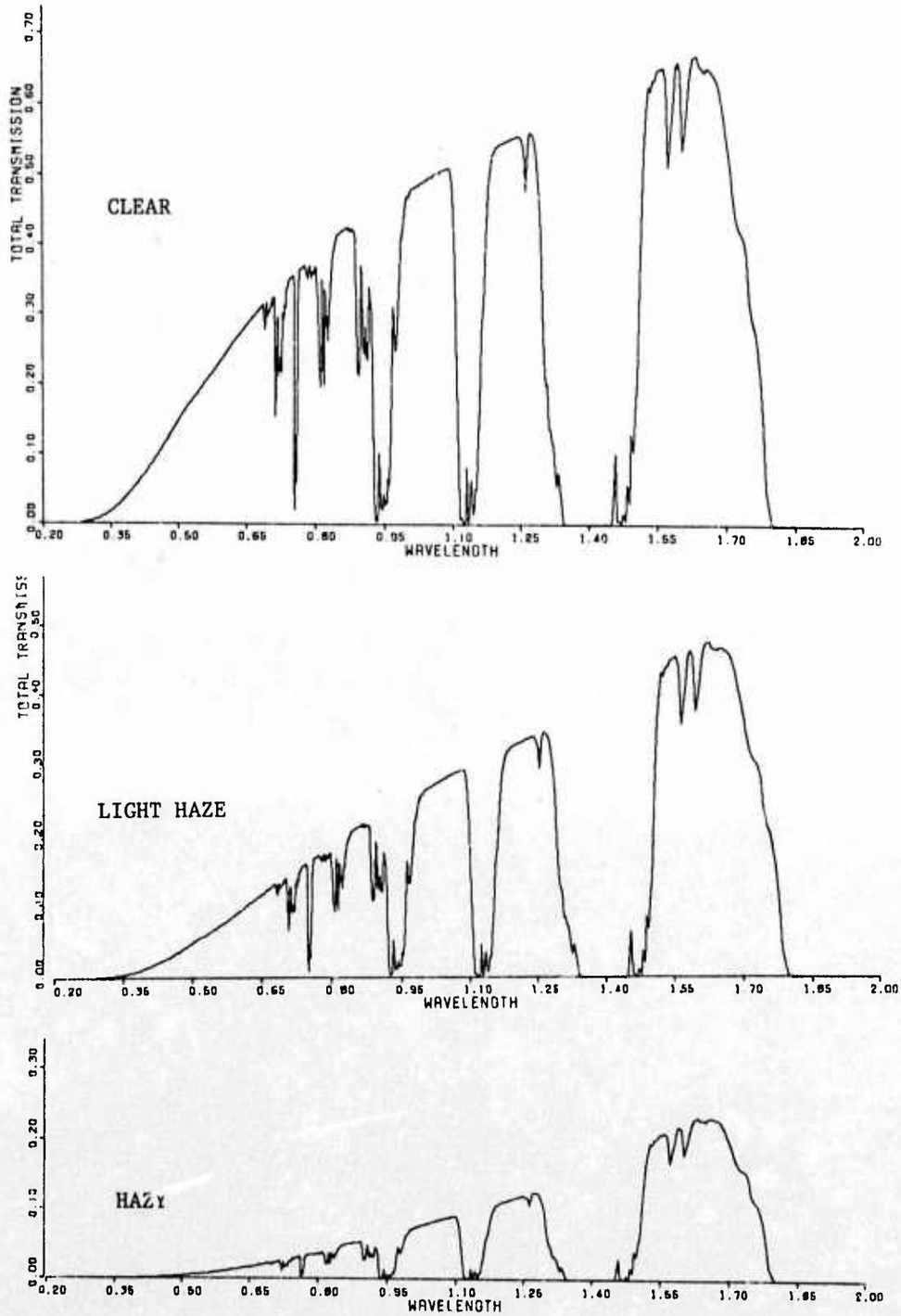

Visible and Near IR Computer-Calculated Band Transmittance over 66-km Slant Path, Tropical Atmosphere Model, Average Continental Aerosol Model.

Set I (cont.)

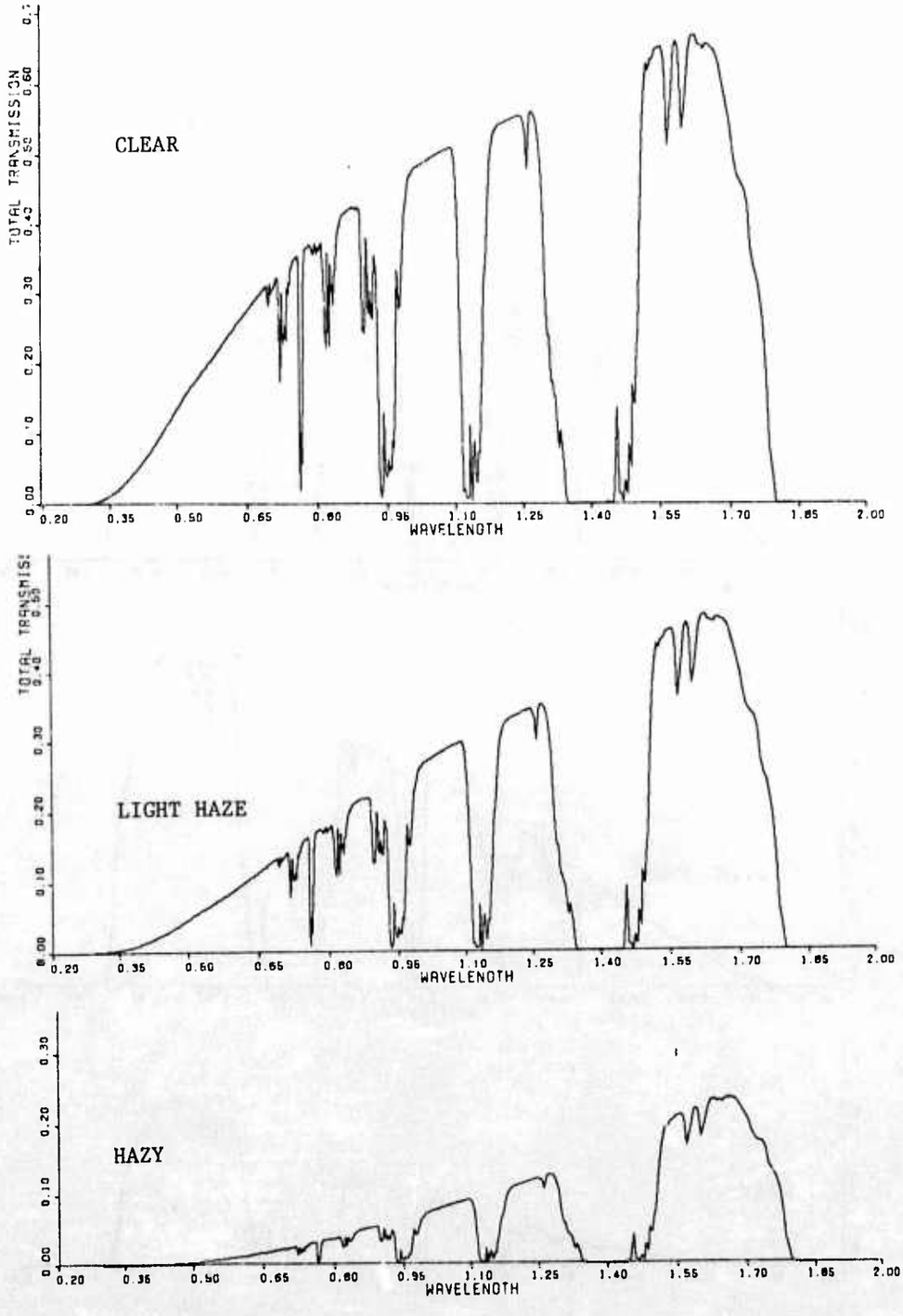

Visible and Near IR Computer-Calculated Band Transmittance over 66-km Slant Path, Mid-Latitude Summer Model, Average Continental Aerosol Model.

Set I (cont.)

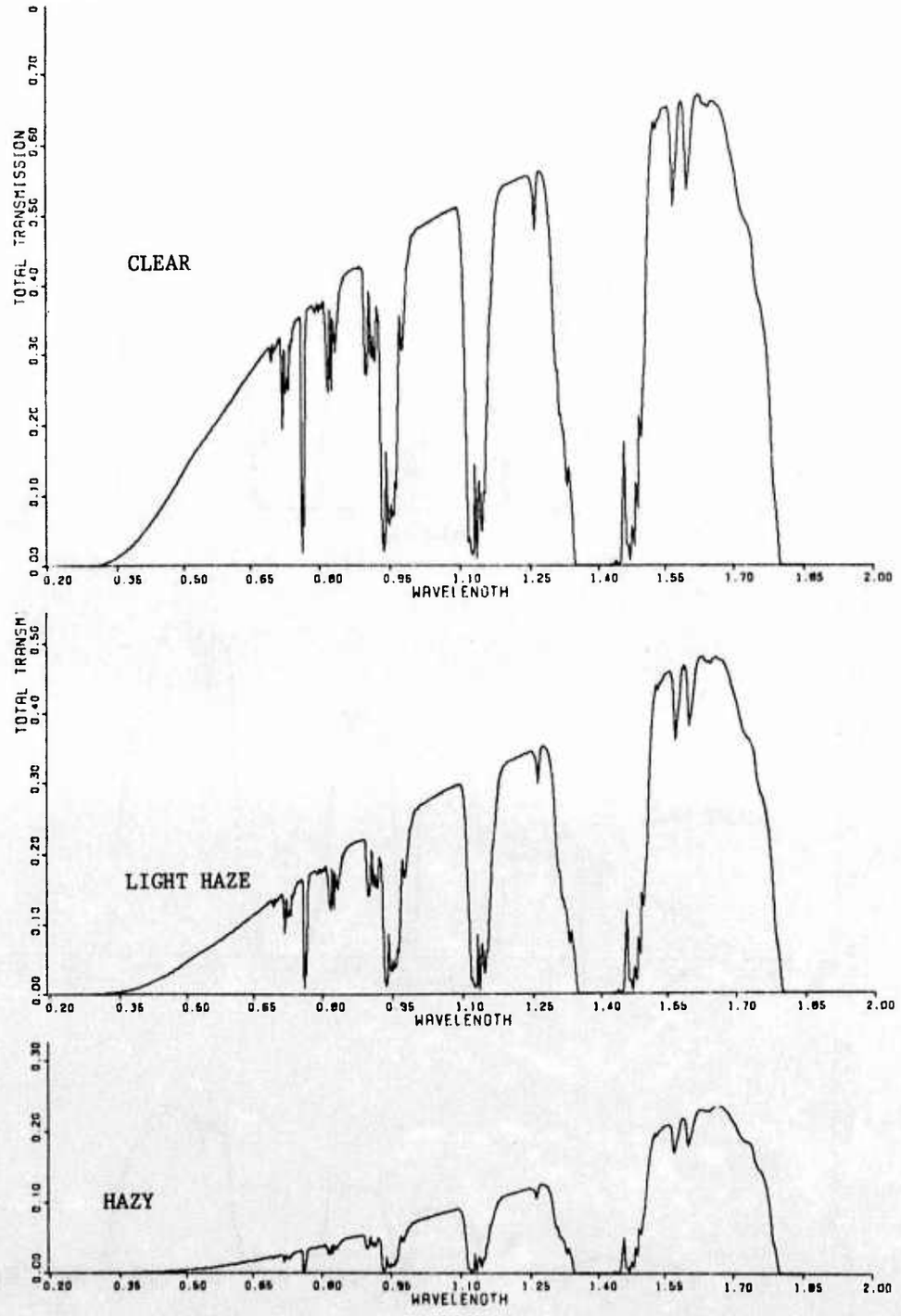

Visible and Near IR Computer-Calculated Band Transmittance over 66-km Slant Path, Sub-Arctic Summer Model, Average Continental Aerosol Model.

Set I (cont.)

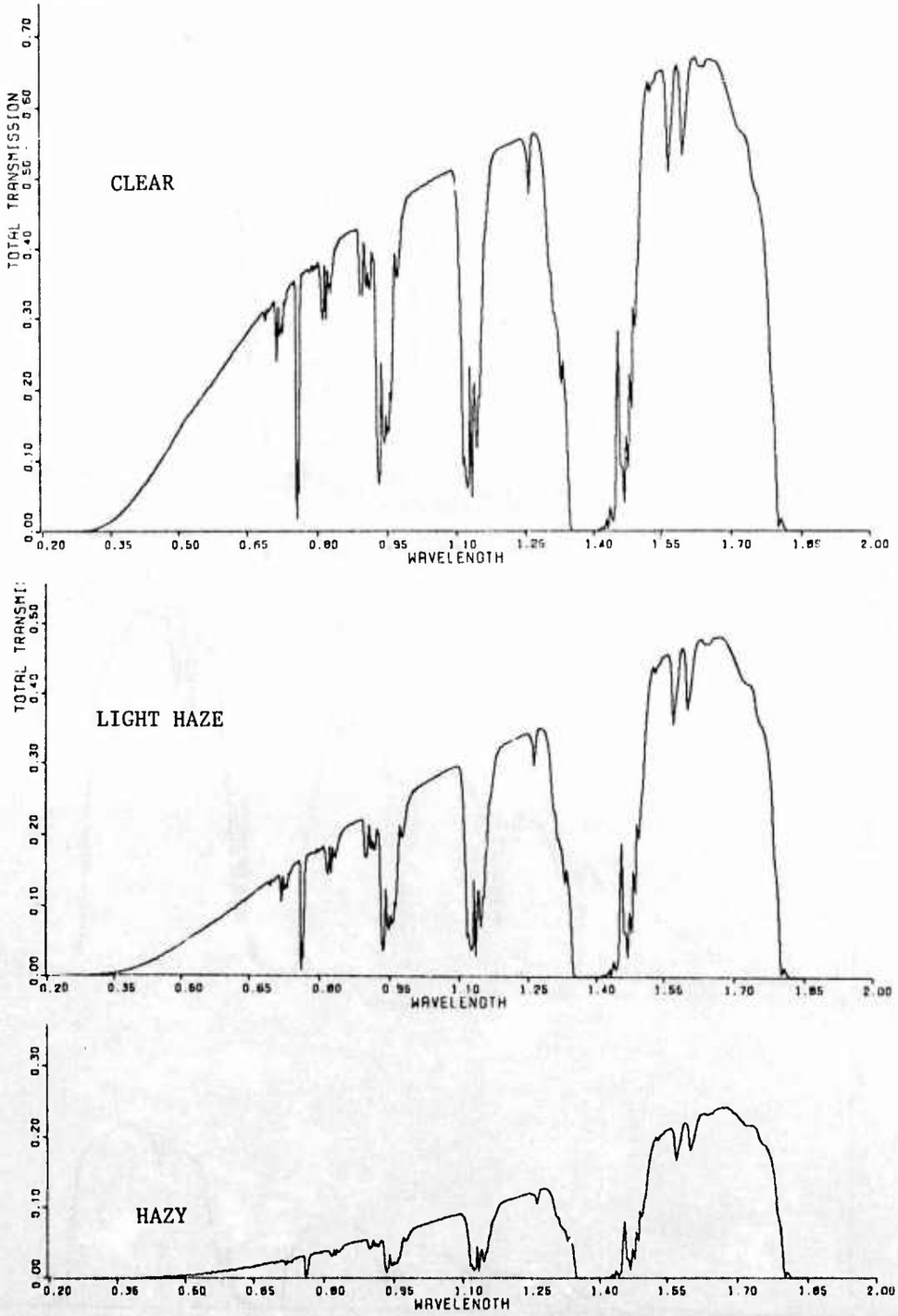

Visible and Near IR Computer-Calculated Band Transmittance over 66-km Slant Path, Mid-Latitude Winter Model, Average Continental Aerosol Model.

Set I (cont.)

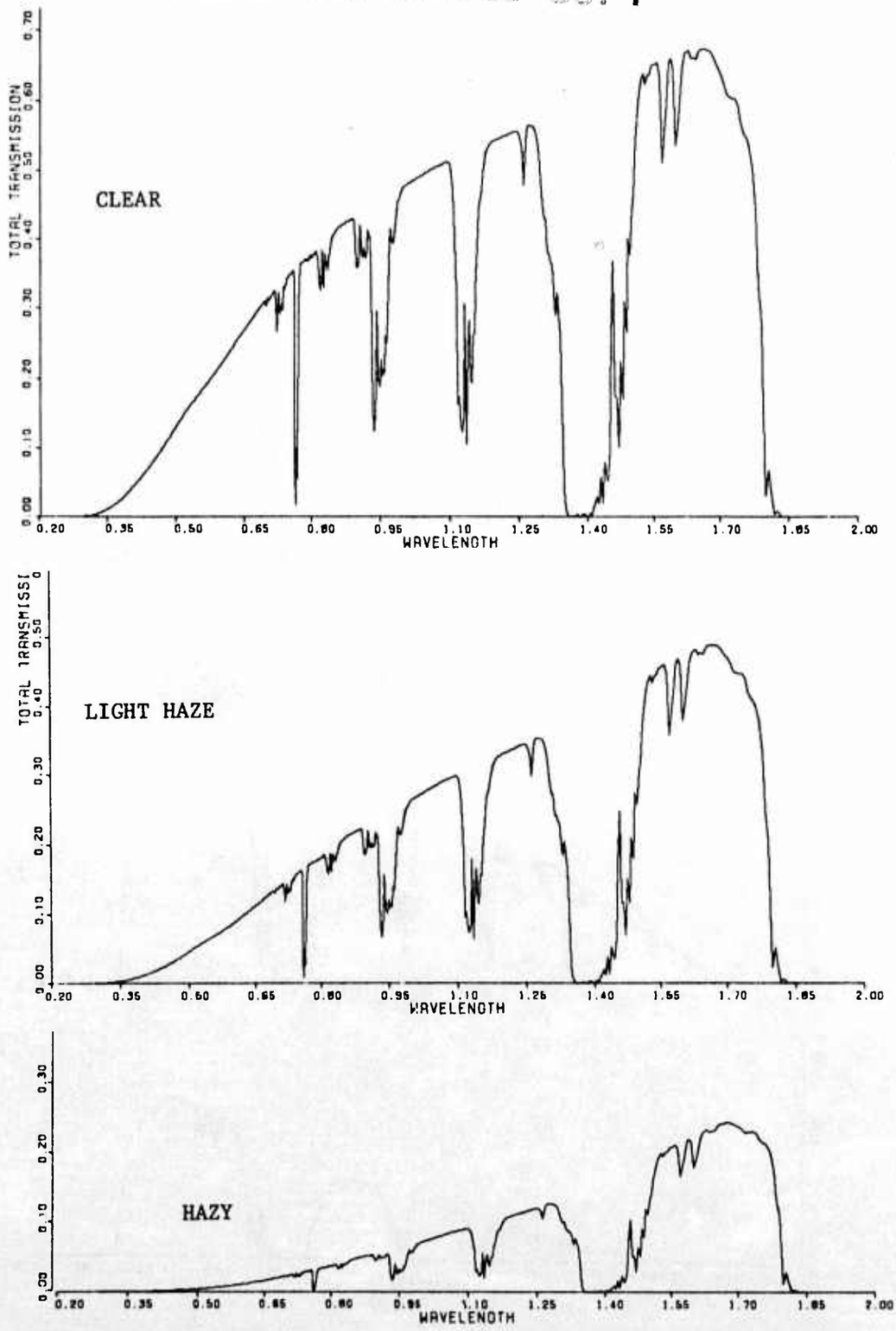

Visible and Near IR Computer-Calculated Band Transmittance over 66-km Slant Path, Sub-Arctic Winter Model, Average Continental Aerosol Model.

Set II (LOWTRAN 3)

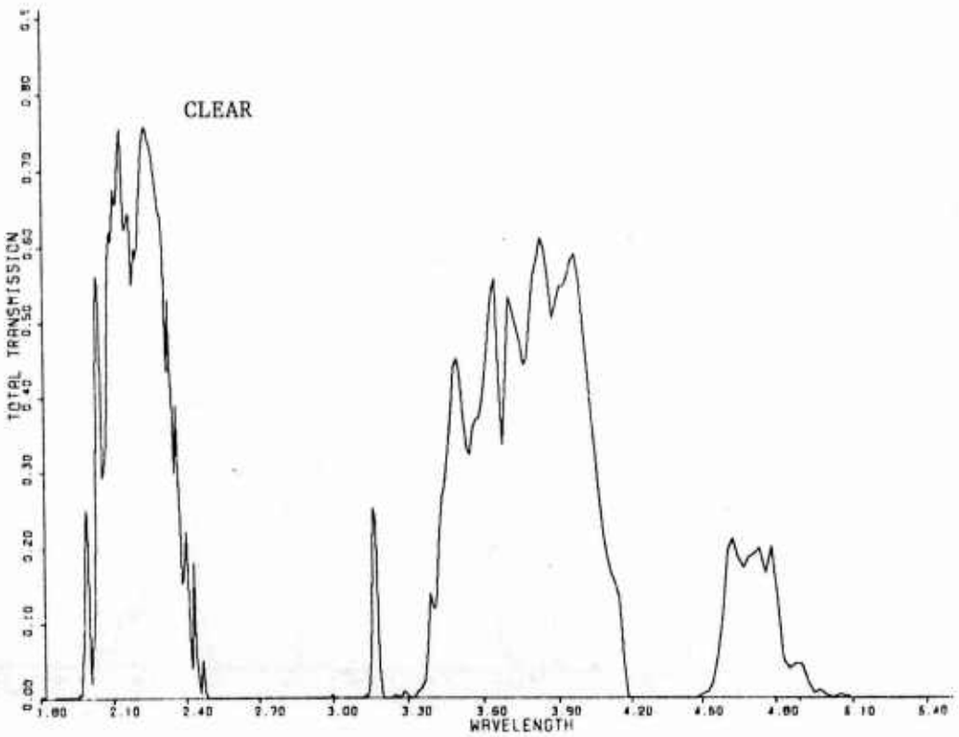

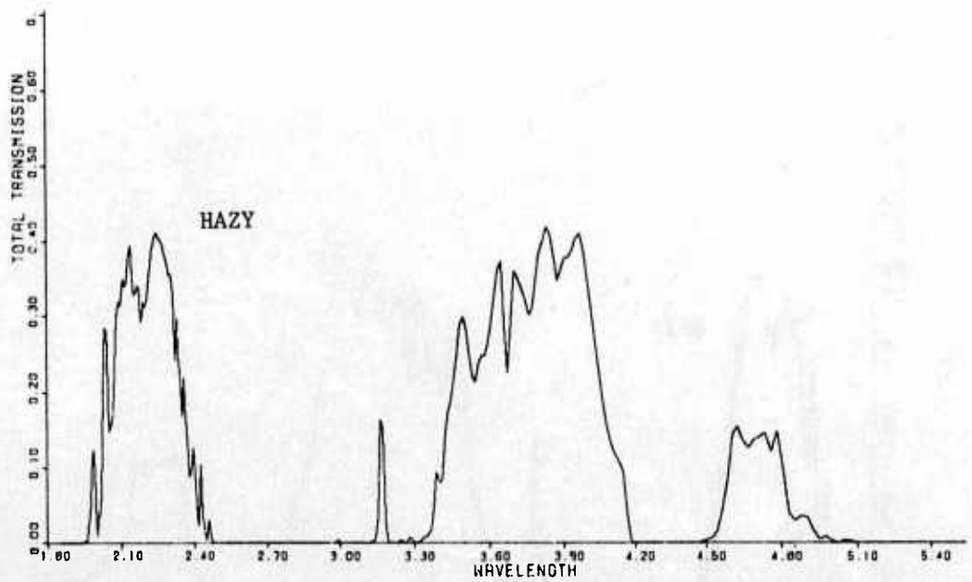

Mid-Range IR Computer-Calculated Band Transmittance over 66-km Slant Path, Tropical Atmosphere Model, Average Continental Aerosol Model.

Set II (cont.)

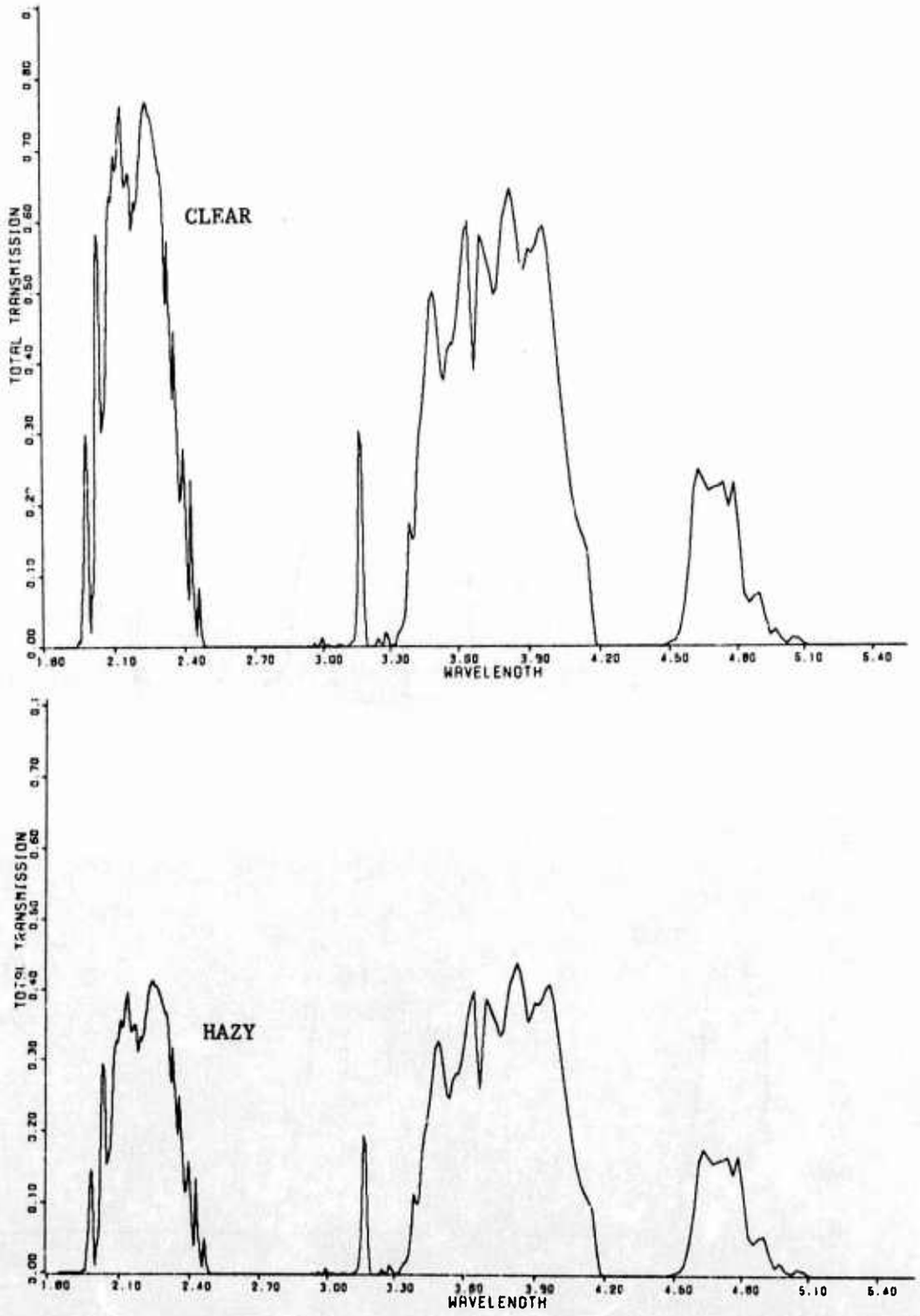

Mid-Range IR Computer-Calculated Band Transmittance over 66-km Slant Path, Mid-Latitude Summer Model, Average Continental Aerosol Model.

Set II (cont.)

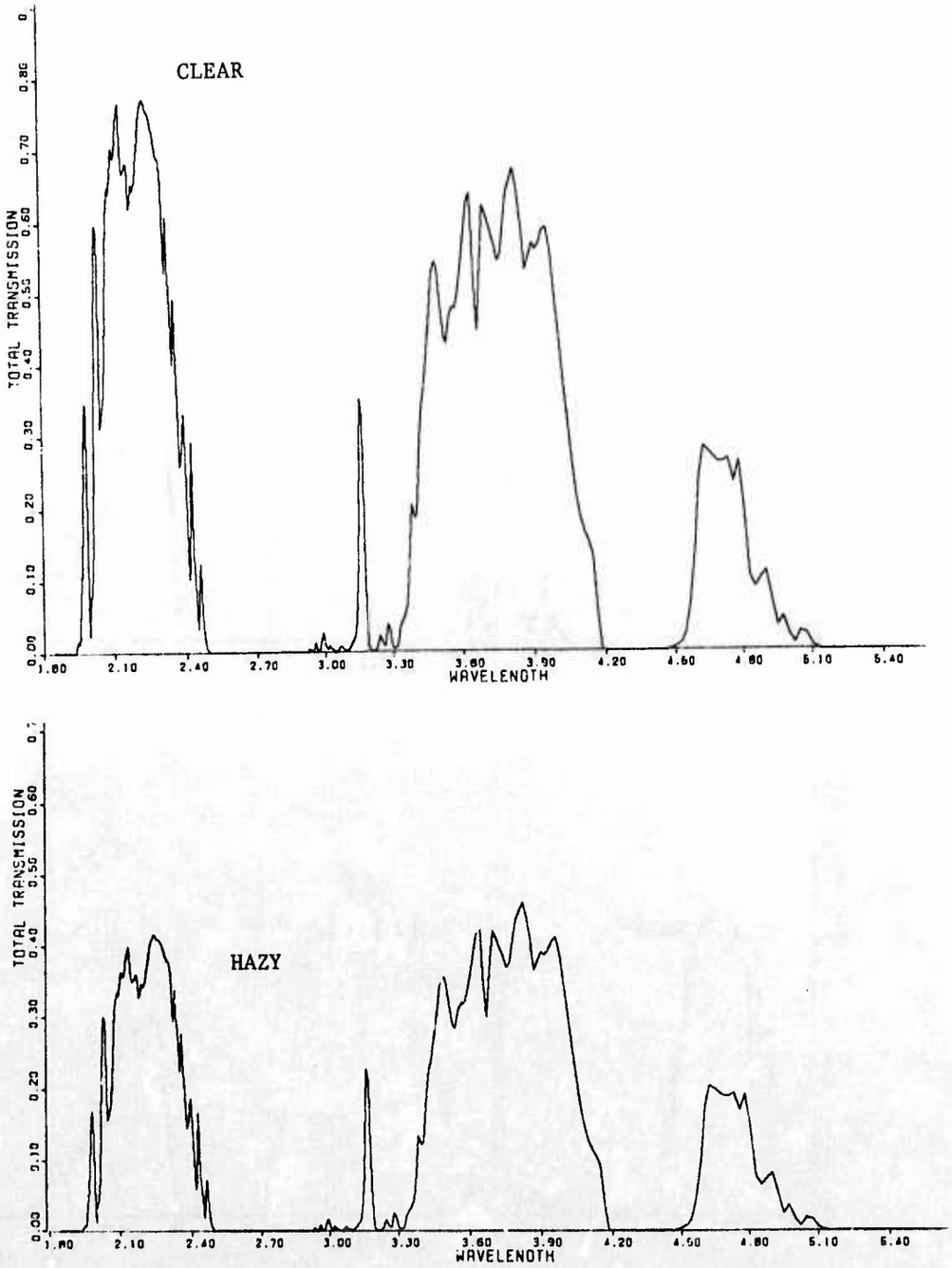

Mid-Range IR Computer-Calculated Band Transmittance over 66-km Slant Path, Sub-Arctic Summer Model, Average Continental Aerosol Model.

Set II (cont.)

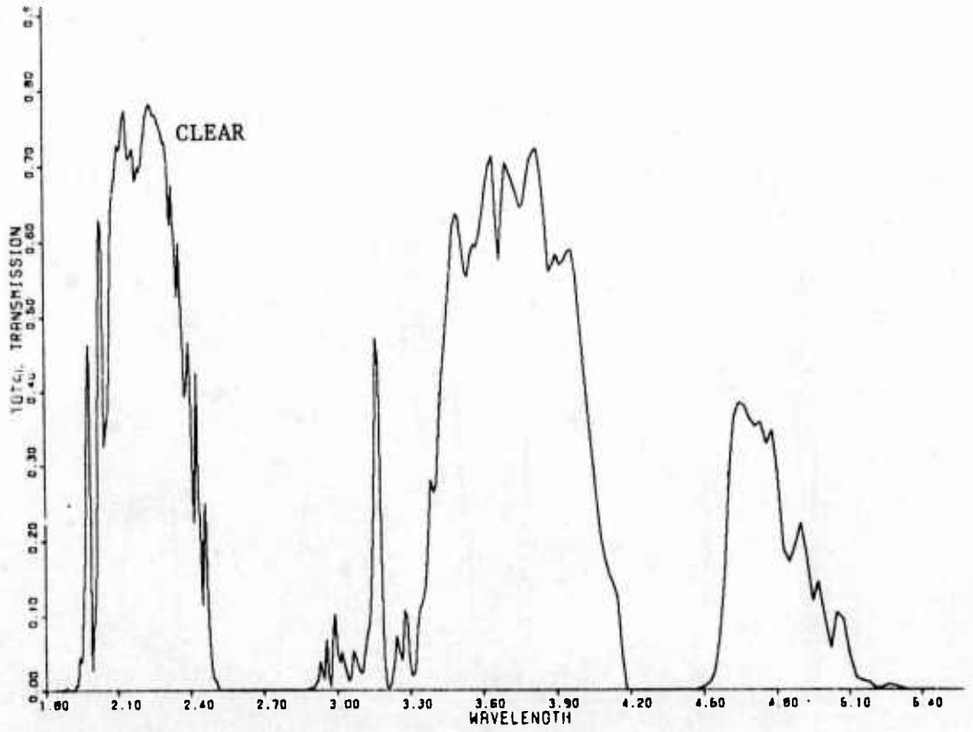

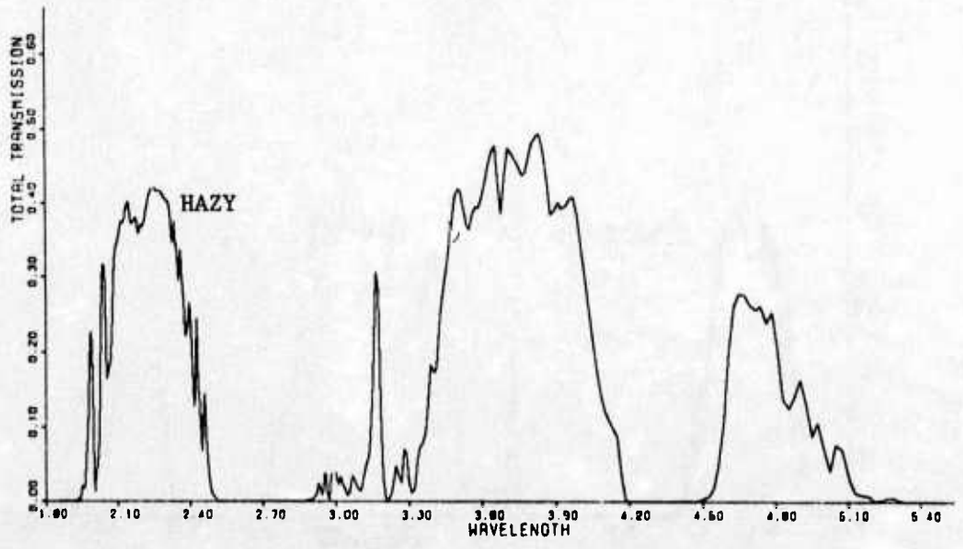

Mid-Range IR Computer-Calculated Band Transmittance over 66-km Slant Path, Mid-Latitude Winter Model, Average Continental Aerosol Model.

Set II (cont.)

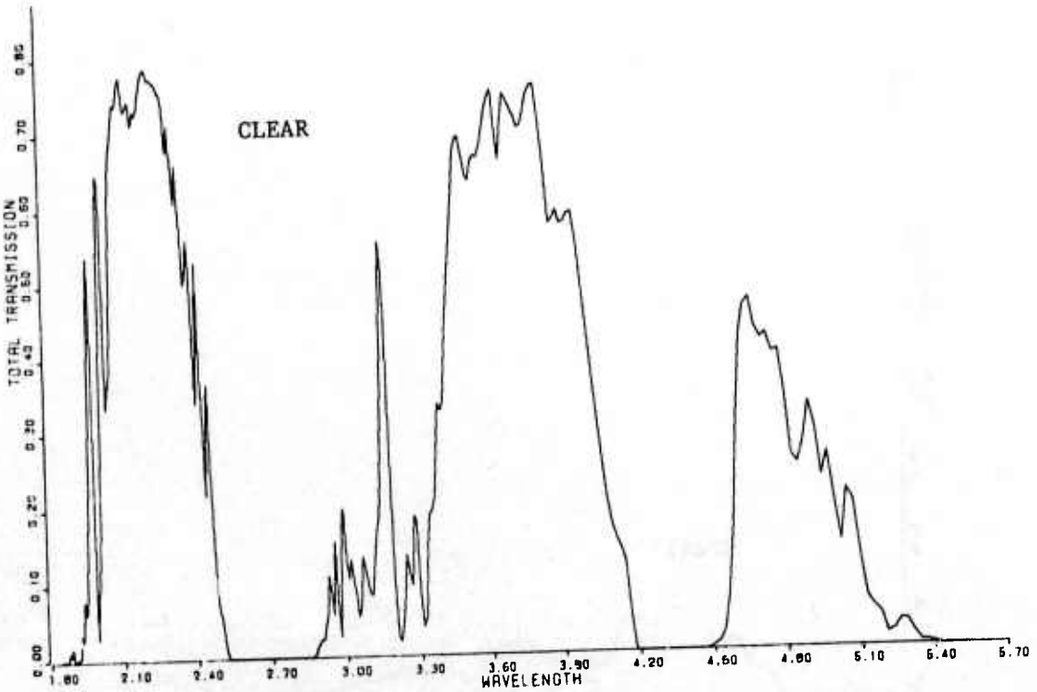

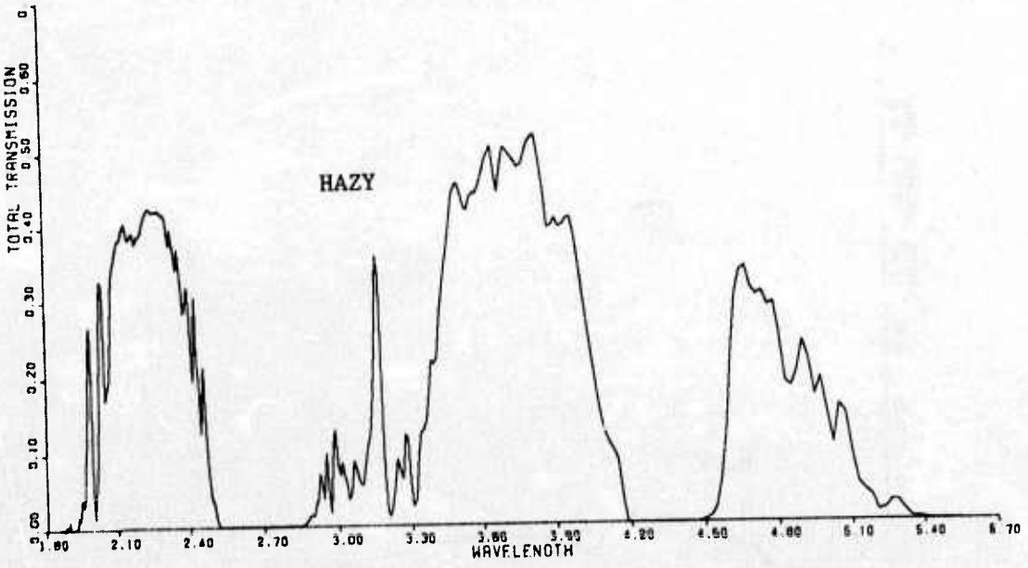

Mid-Range IR Computer-Calculated Band Transmittance over 66-km Slant Path, Sub-Arctic Winter Model, Average Continental Aerosol Model.

Set III (Modified LOWTRAN 3)

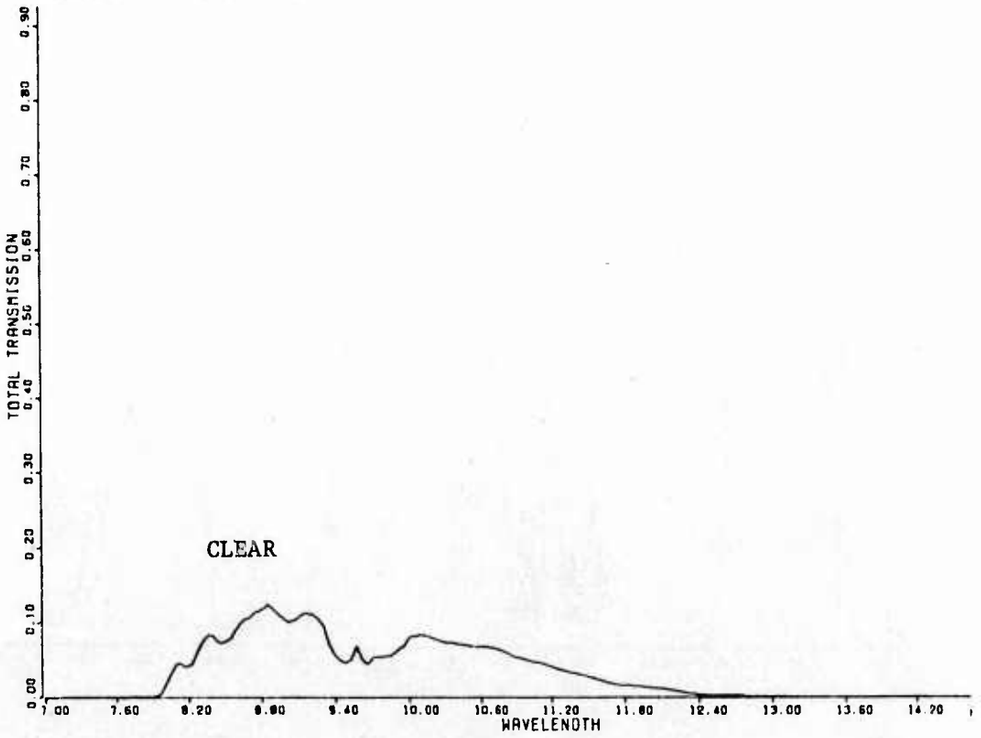

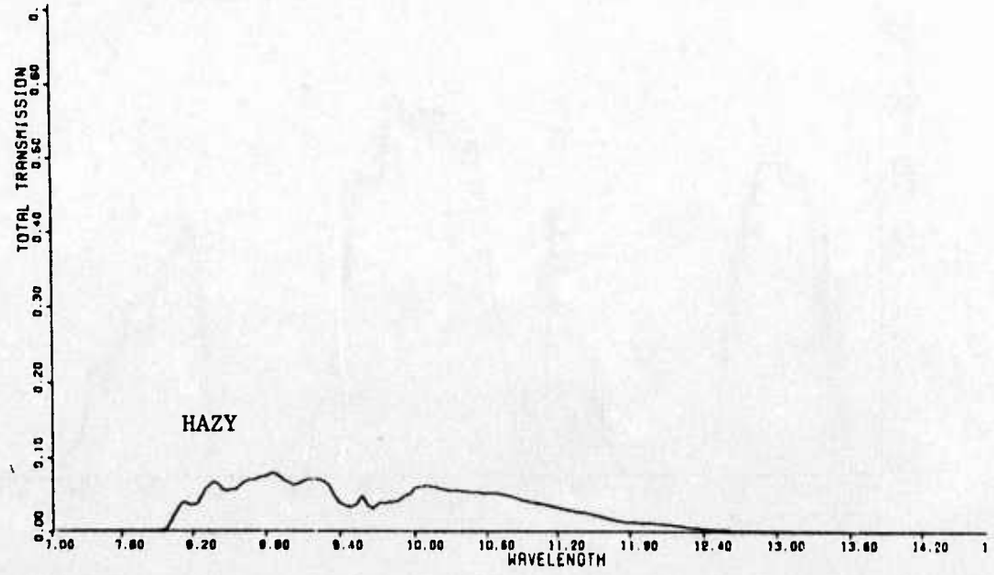

Long-Wave IR Computer-Calculated Band Transmittance over 66-km Slant Path, Tropical Atmosphere Model, Average Continental Aerosol Model.

Set III (cont.)

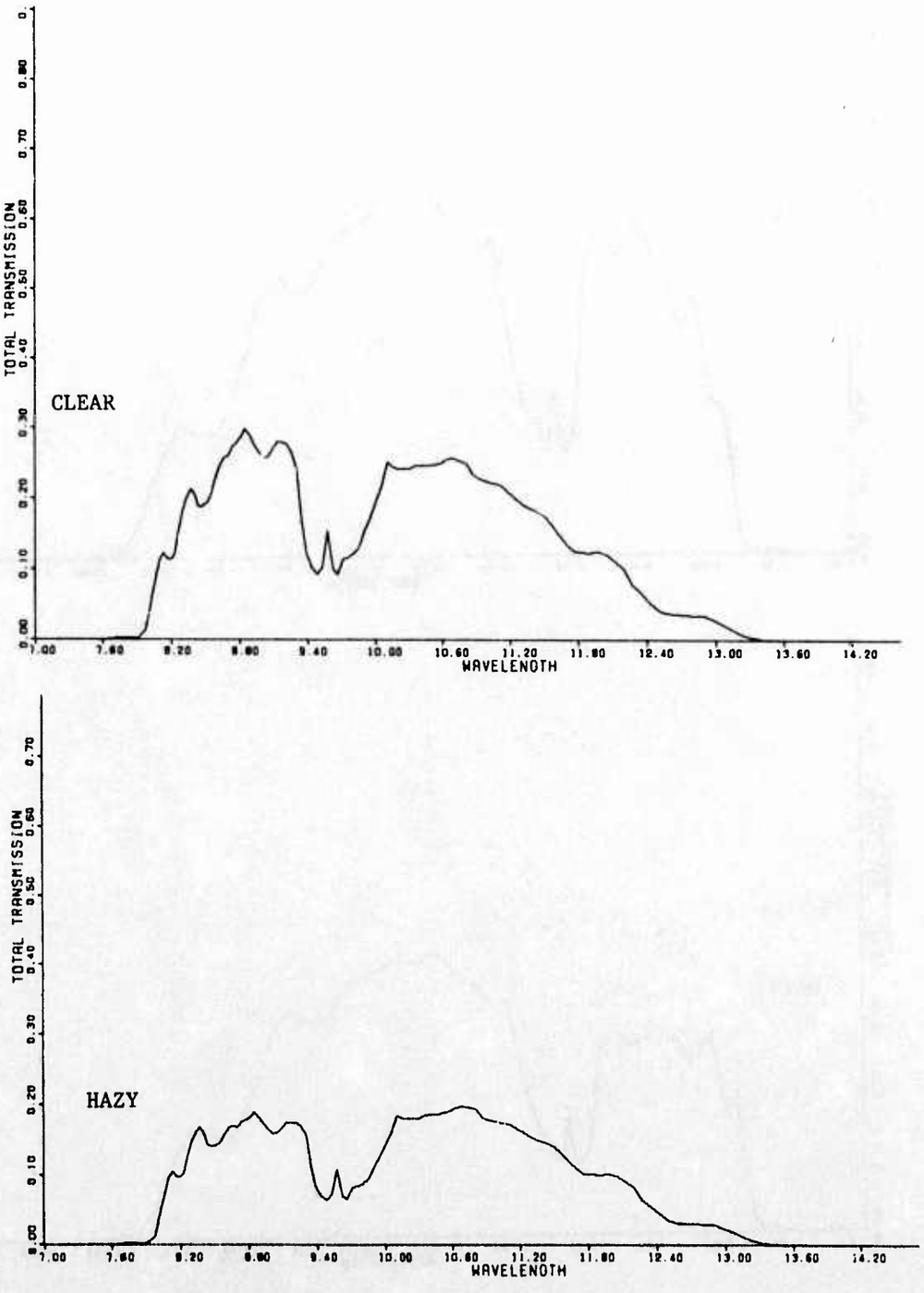

Long-Wave IR Computer-Calculated Band Transmittance over 66-km Slant Path, Mid-Latitude Summer Atmosphere Model, Average Continental Aerosol Model.

Set III (cont.)

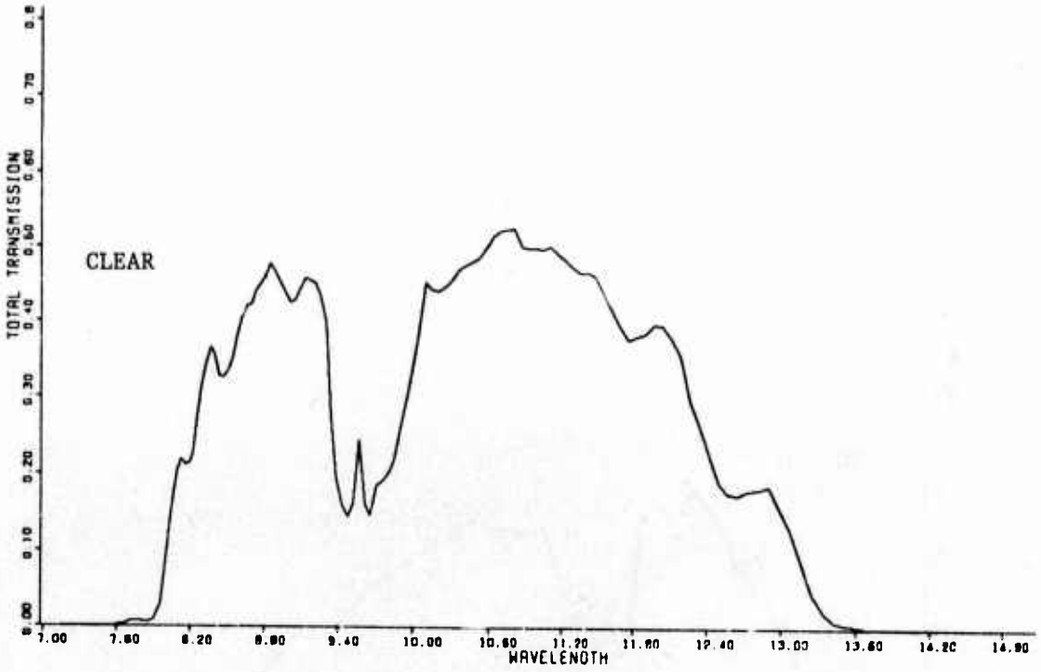

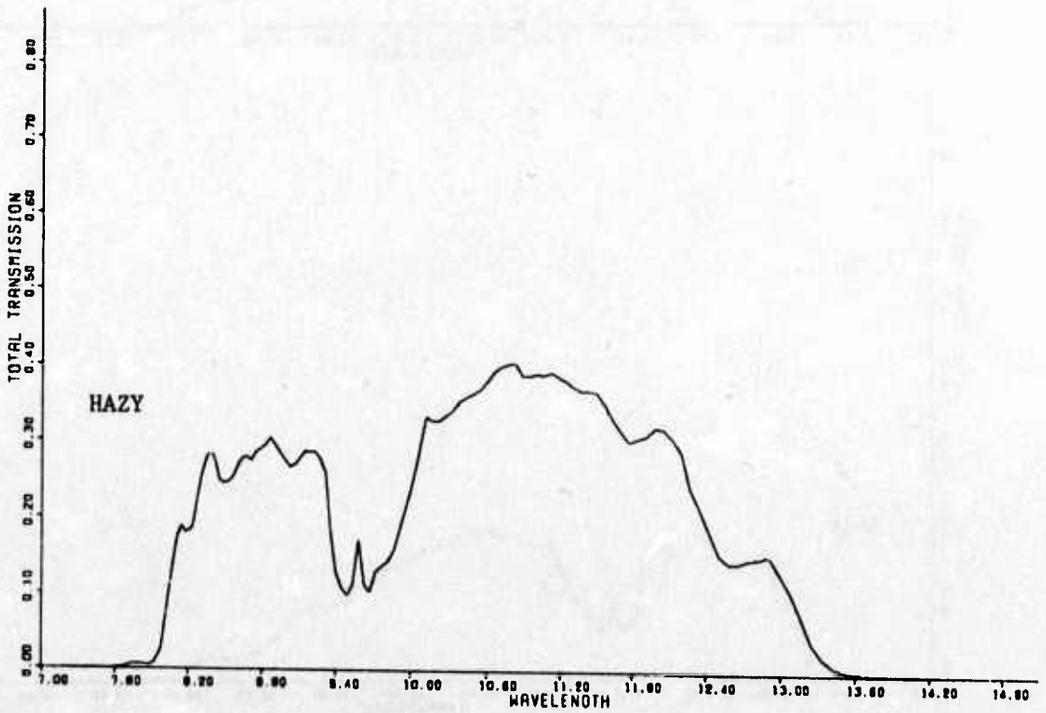

Long-Wave IR Computer-Calculated Band Transmittance over 66-km Slant Path, Sub-Arctic Summer Model, Average Continental Aerosol Model.

Set III (cont.)

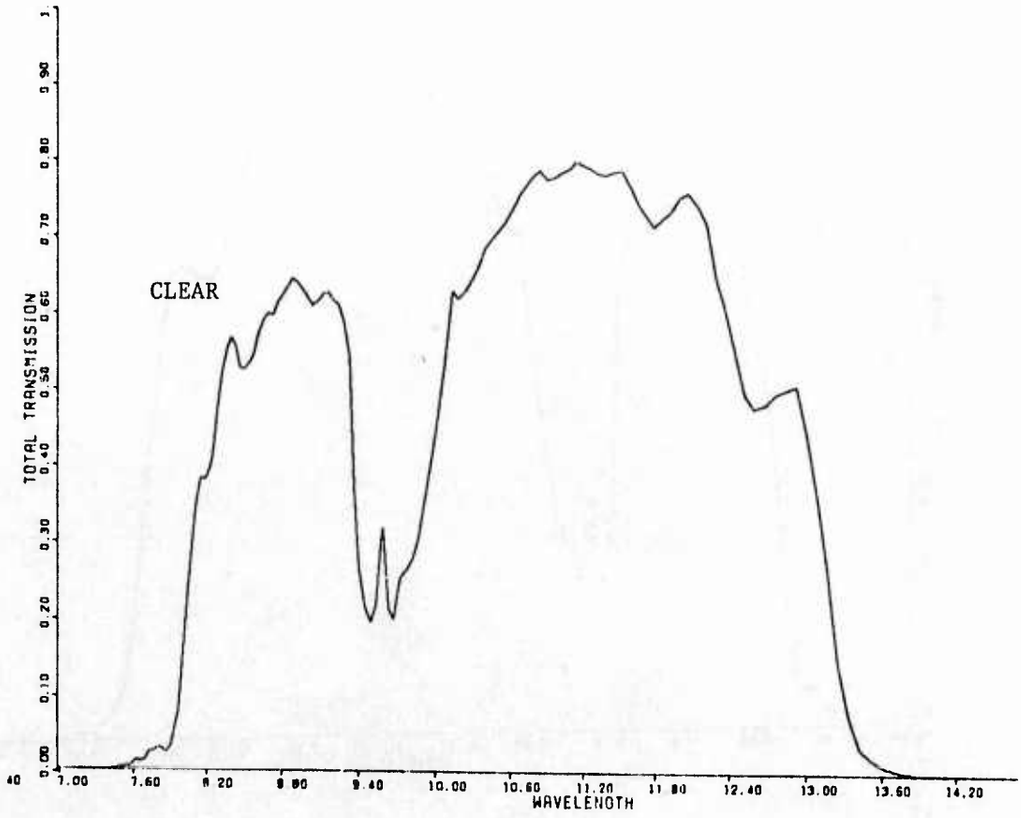

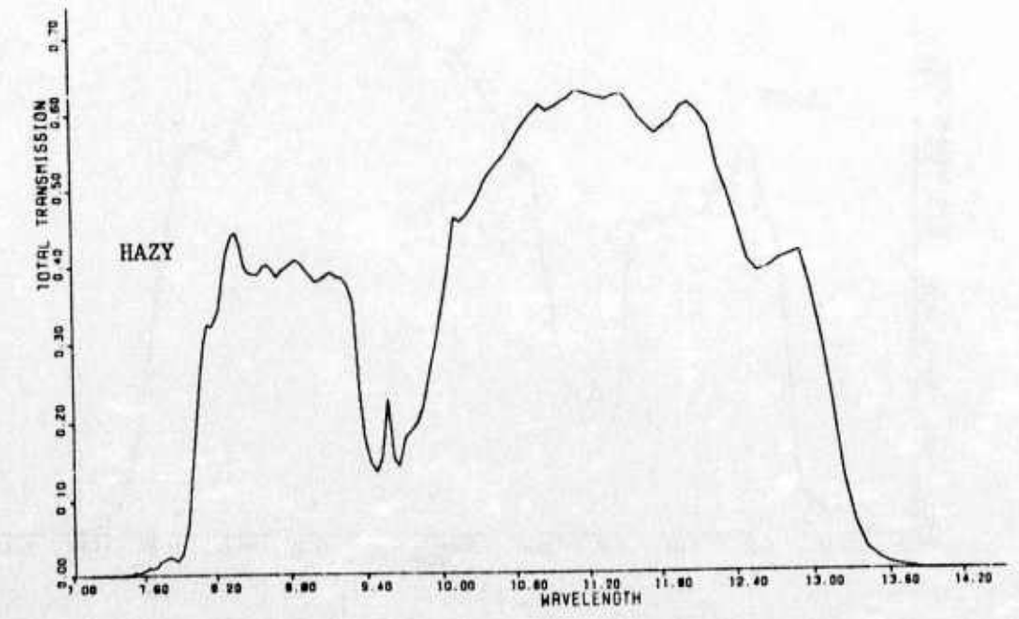

Long-Wave IR Computer-Calculated Band Transmittance over 66-km Slant Path, Mid-Latitude Winter Model, Average Continental Aerosol Model.

Set III (cont.)

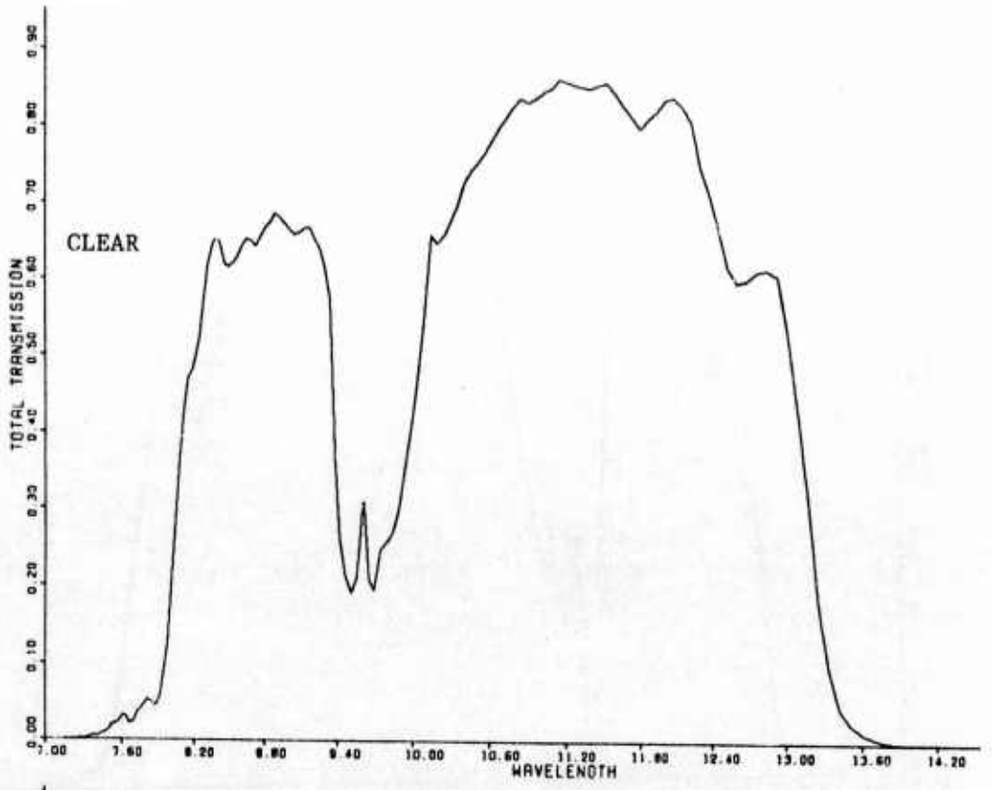

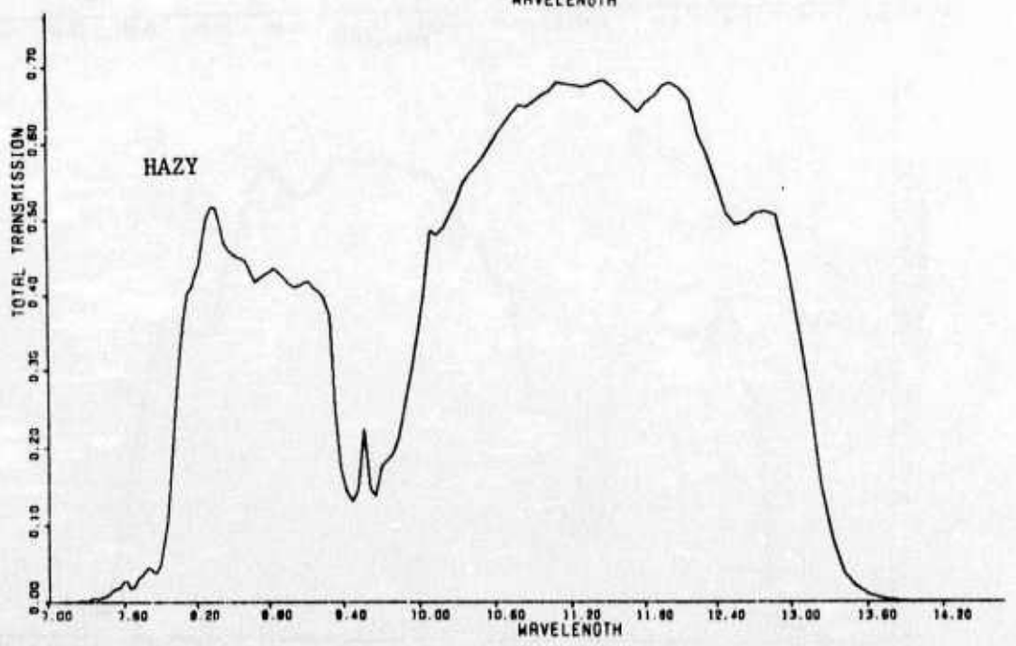

Long-Wave IR Computer-Calculated Band Transmittance over 66-km Slant Path, Sub-Arctic Winter Model, Average Continental Aerosol Model.

Set IV (LOWTRAN 3 - Marine)

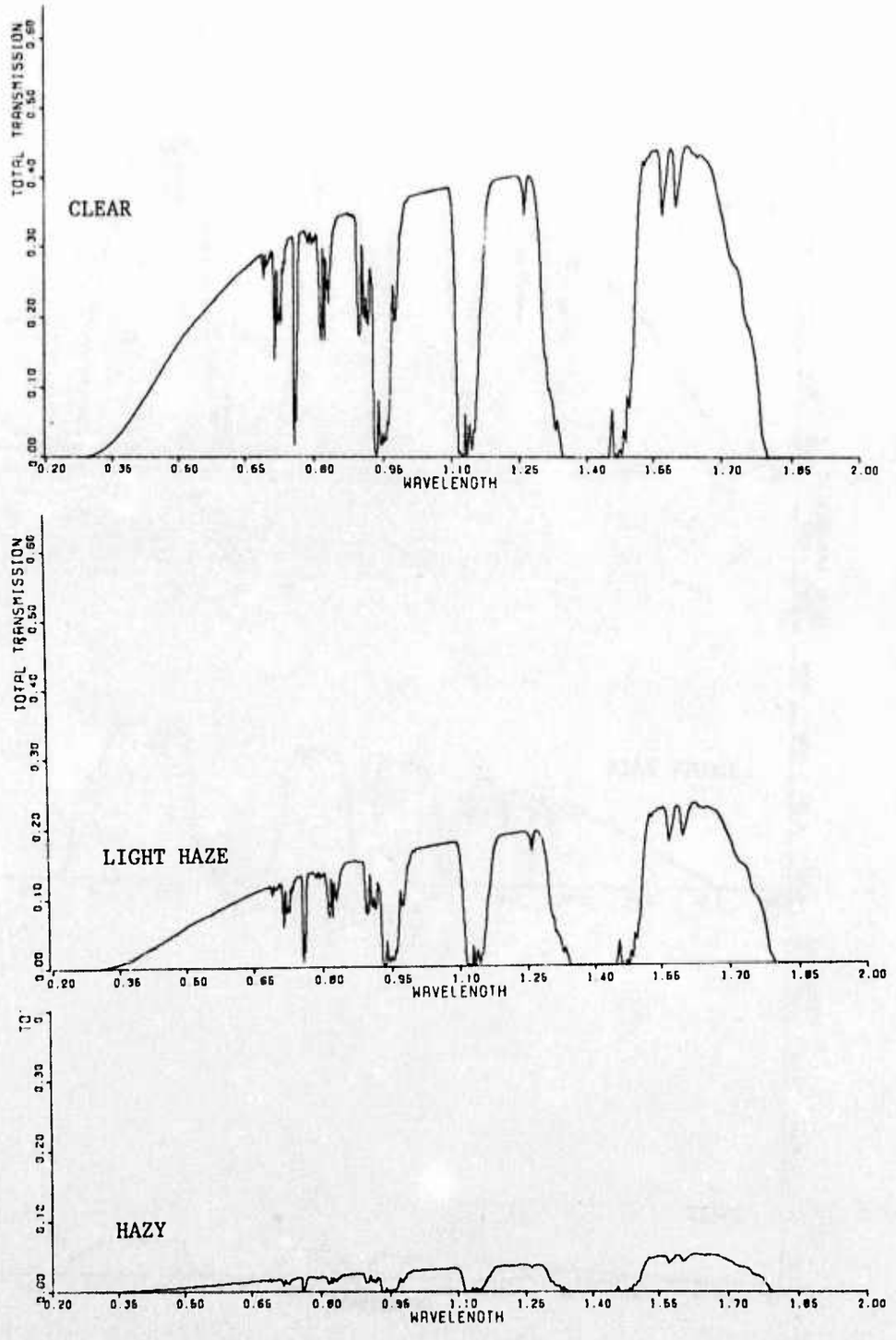

Visible and Near-IR Computer-Calculated Band Transmittance over 66-km Slant Path, Tropical Atmosphere Model, Estimated Marine Aerosol Model.

Set IV (cont.)

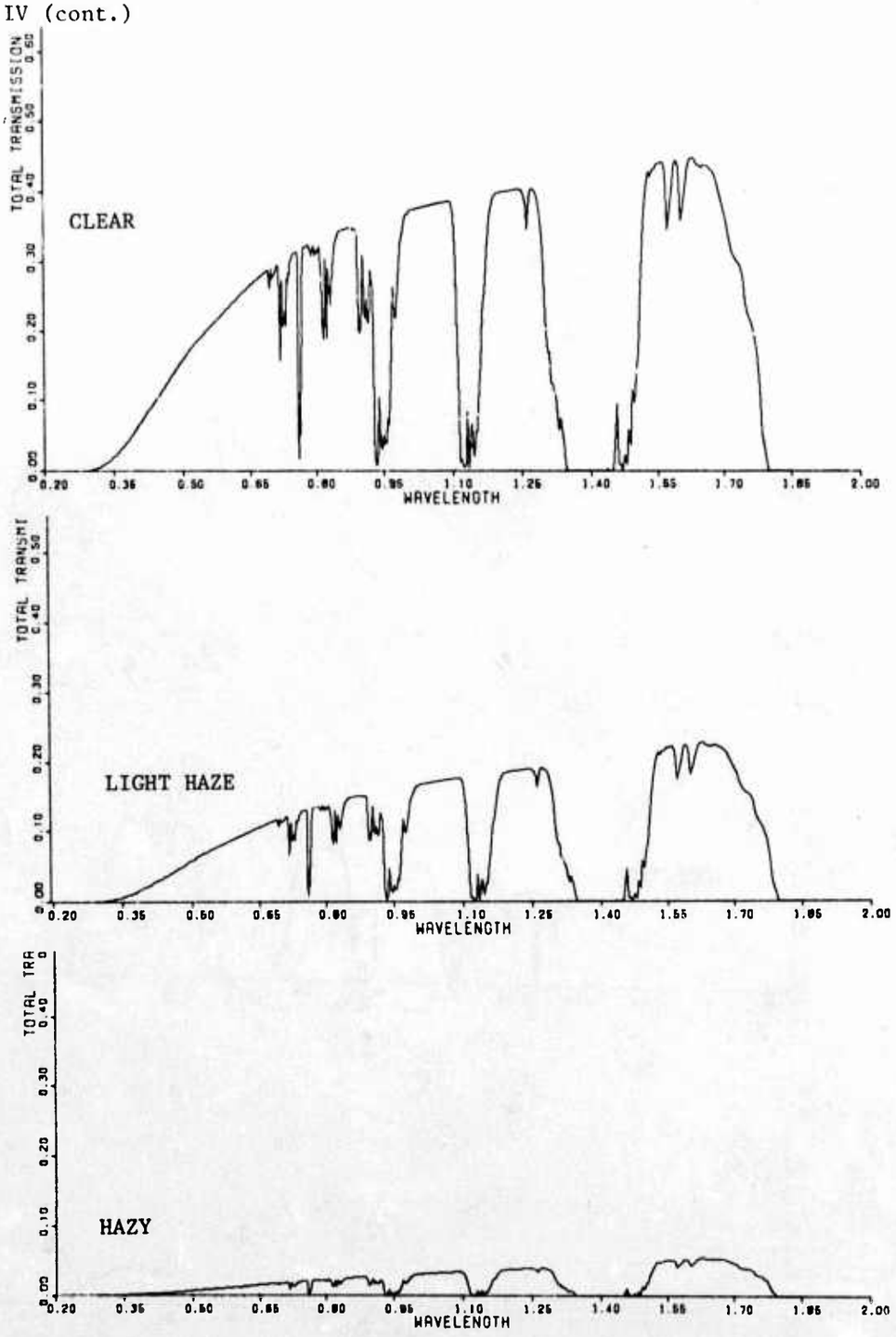

Visible and Near-IR Computer-Calculated Band Transmittance over 66-km Slant Path, Mid-Latitude Summer Model, Estimated Marine Aerosol Model.

Set IV (cont.)

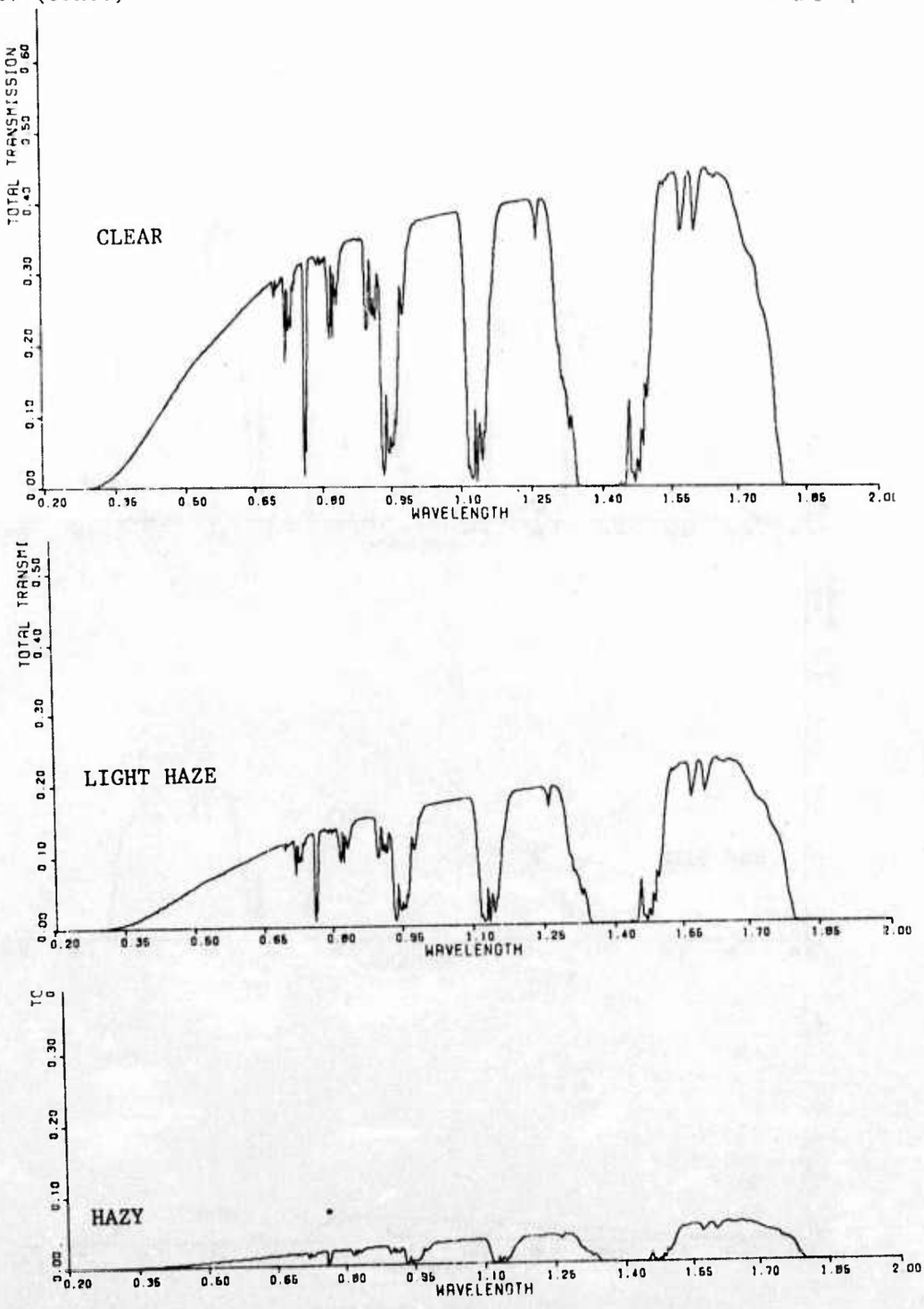

Visible and Near-IR Computer-Calculated Band Transmittance over 66-km Slant Path, Sub-Arctic Summer Model, Estimated Marine Aerosol Model.

Set IV (cont.)

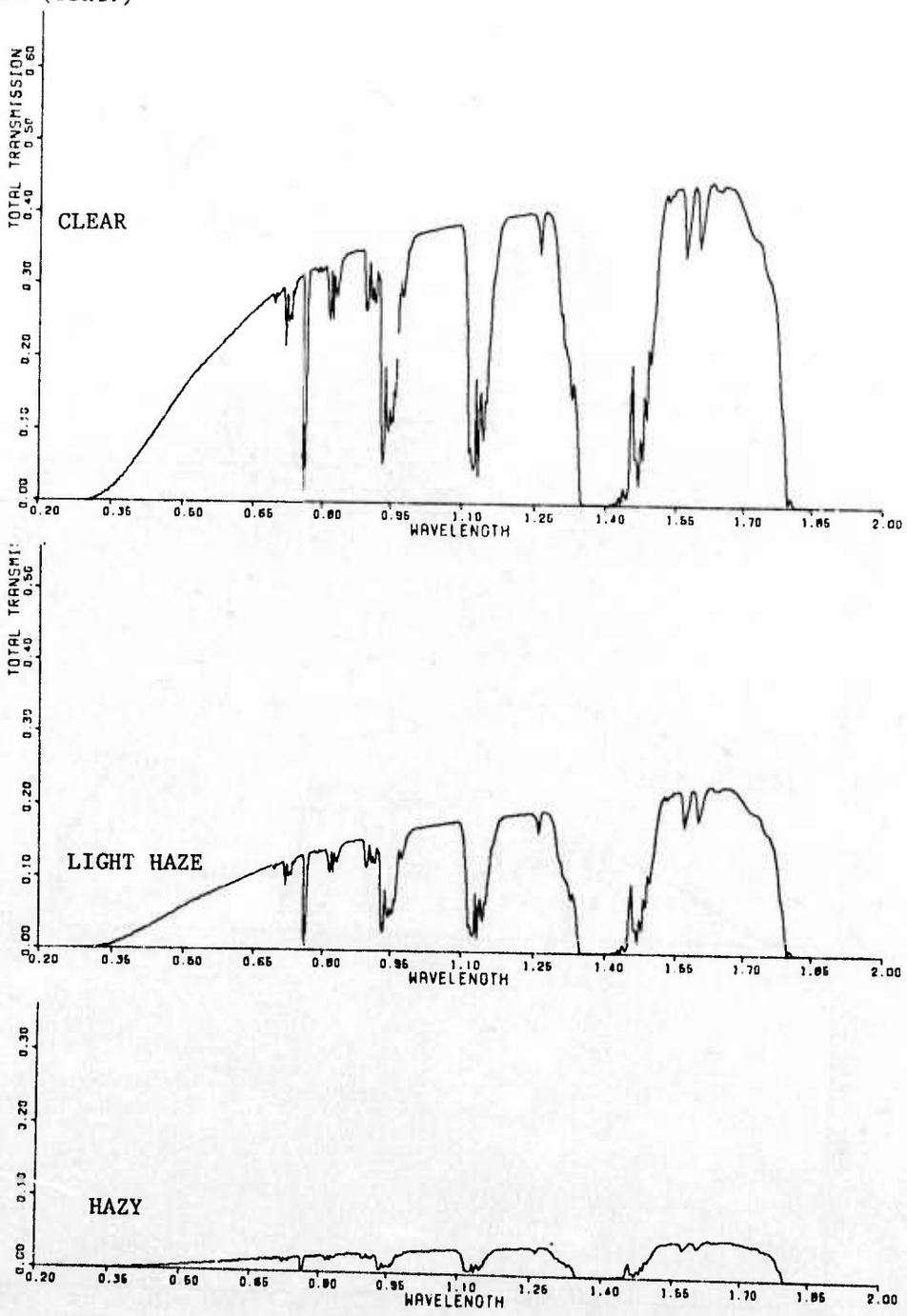

Visible and Near-IR Computer-Calculated Band Transmittance over 66-km Slant Path, Mid-Latitude Winter Model, Estimated Marine Aerosol Model.

Set IV (cont.)

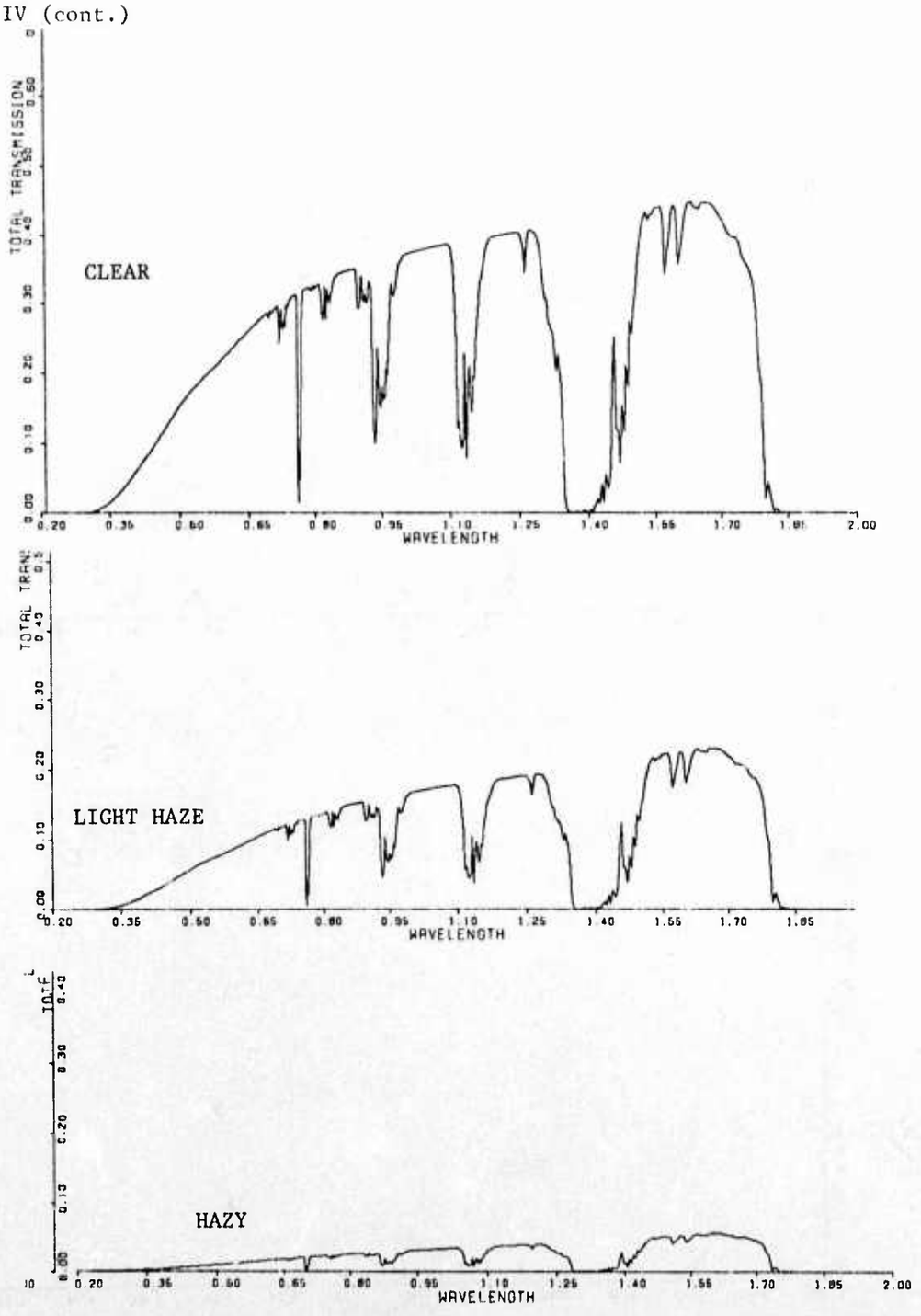

Visible and Near-IR Computer-Calculated Band Transmittance over 66-km Slant Path, Sub-Arctic Winter Model, Estimated Marine Aerosol Model.

Set V (LOWTRAN 3 - Marine)

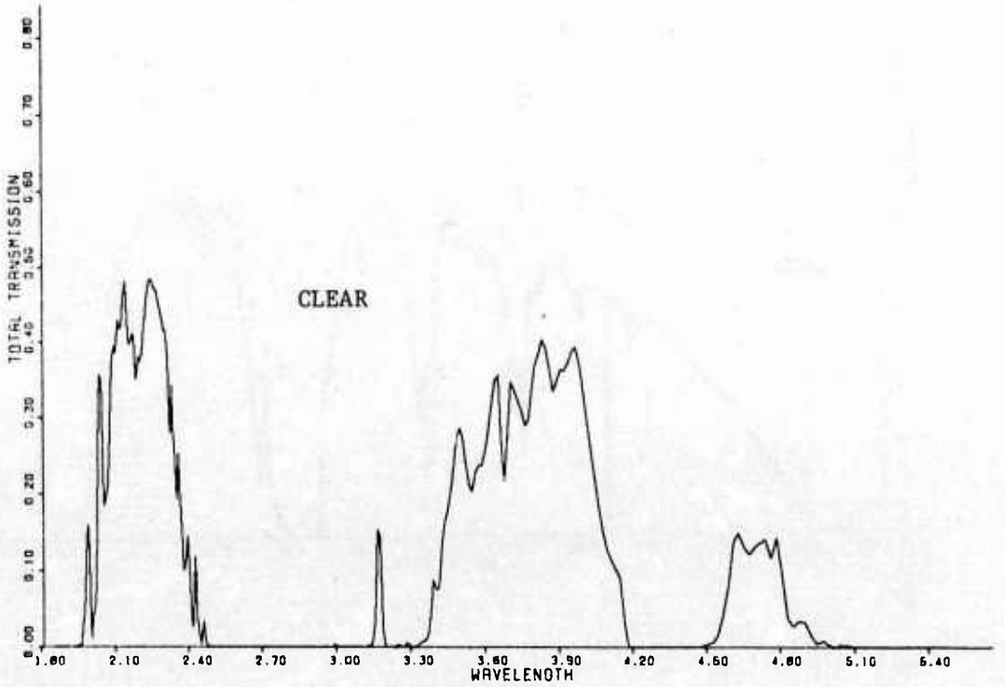

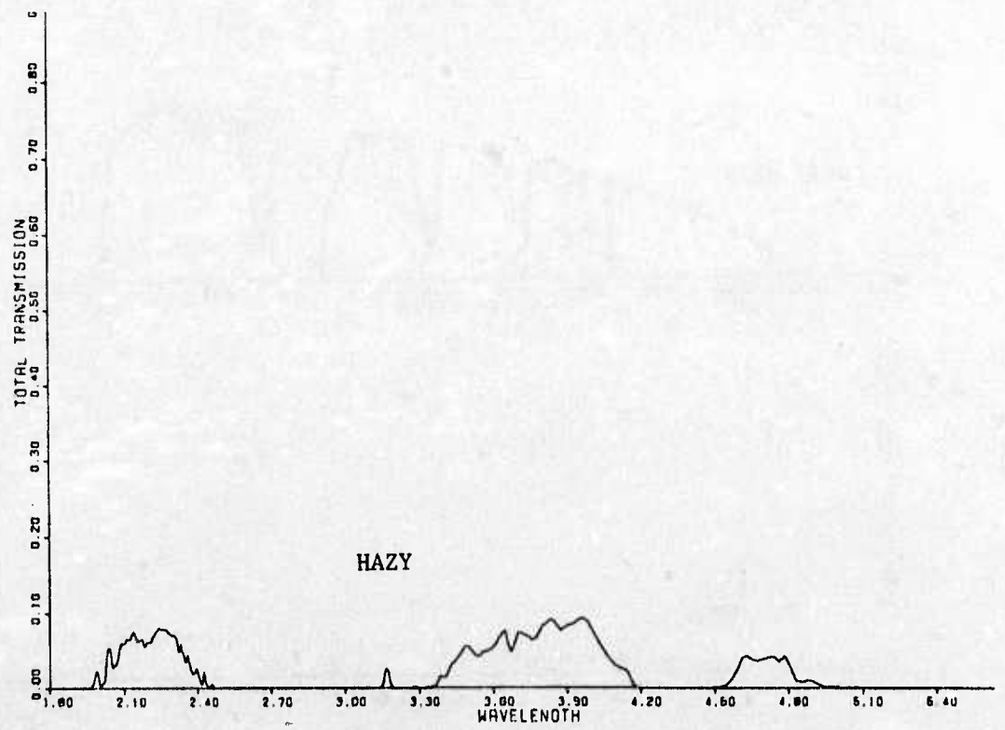

Mid-Range IR Computer-Calculated Band Transmittance over 66-km Slant Path, Tropical Atmosphere Model, Estimated Marine Aerosol Model.

Set V (cont.)

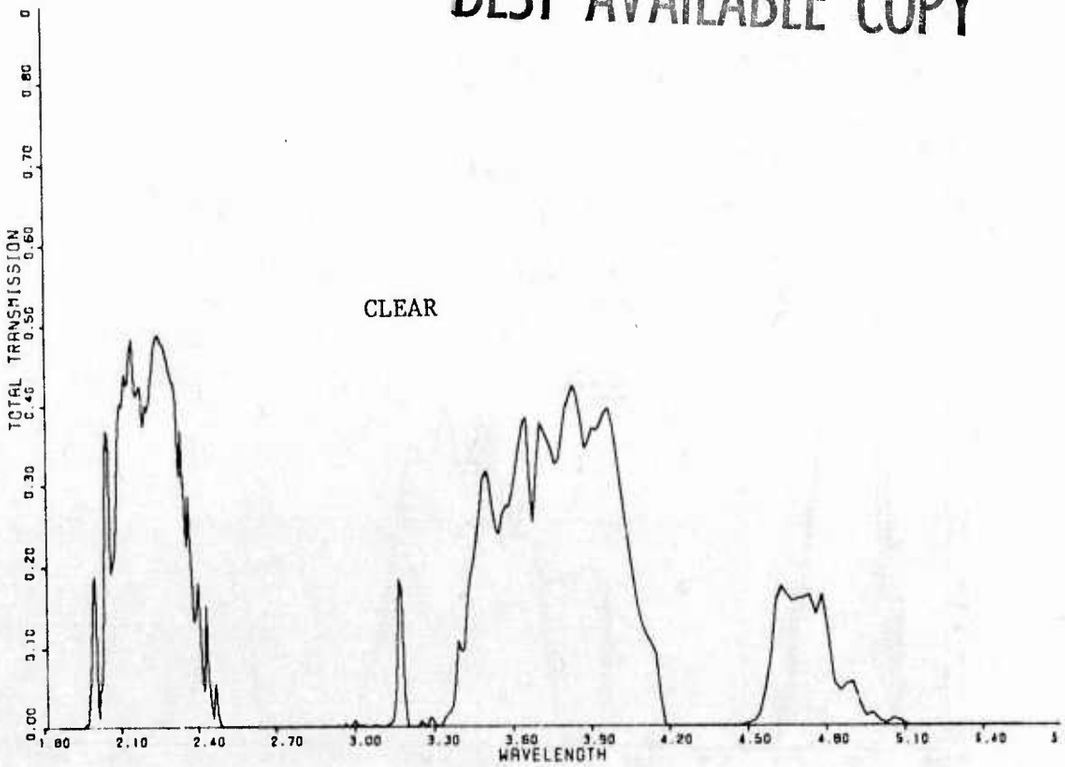

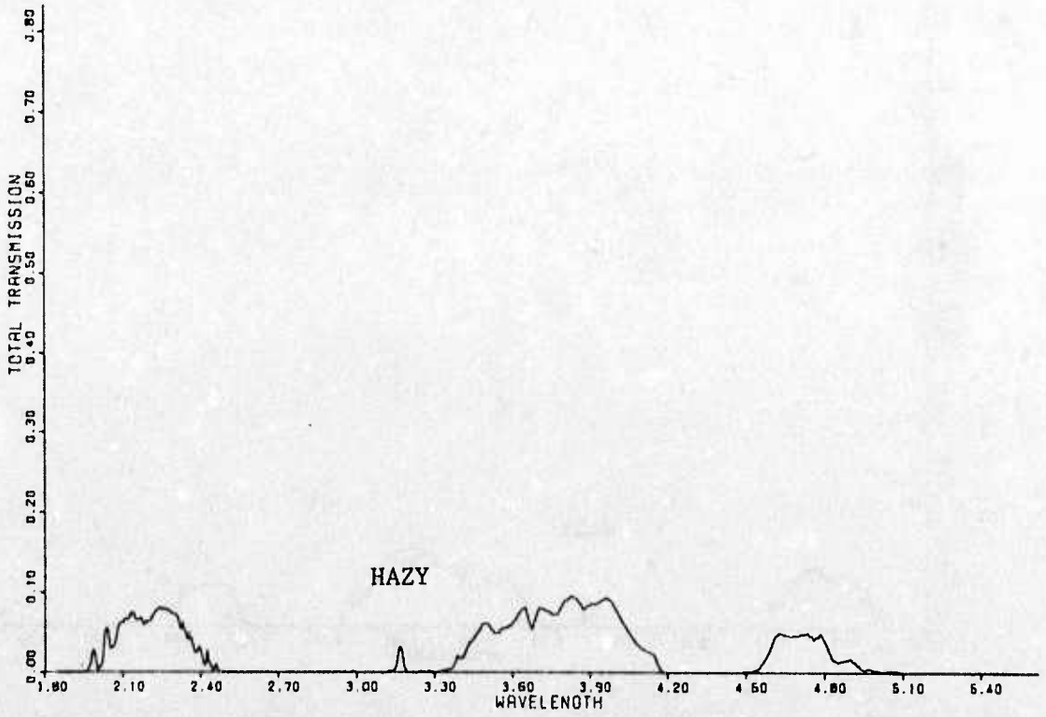

Mid-Range IR Computer-Calculated Band Transmittance over 66-km Slant Path Mid-Latitude Summer Model, Estimated Marine Aerosol Model.

Set V (cont.)

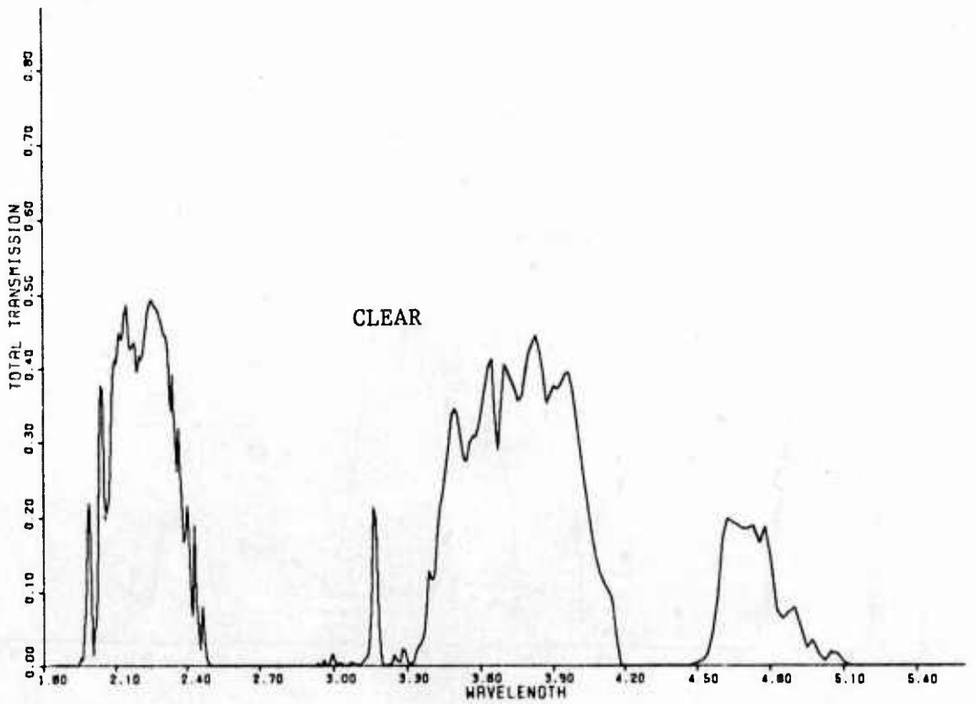

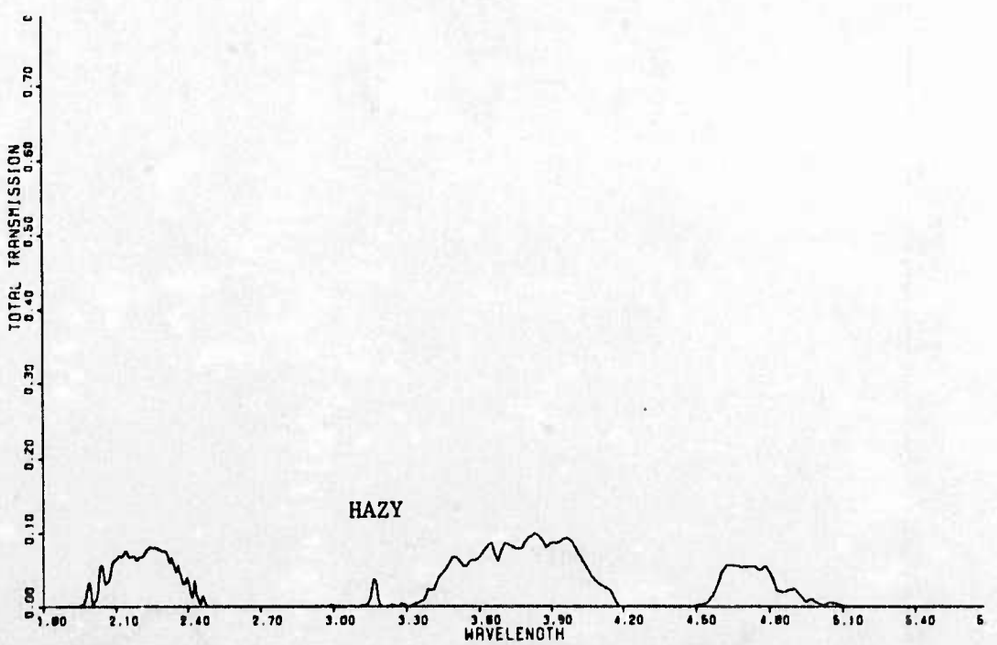

Mid-Range IR Computer-Calculated Band Transmittance over 66-km Slant Path, Sub-Arctic Summer Model, Estimated Marine Aerosol Model.

Set V (cont.)

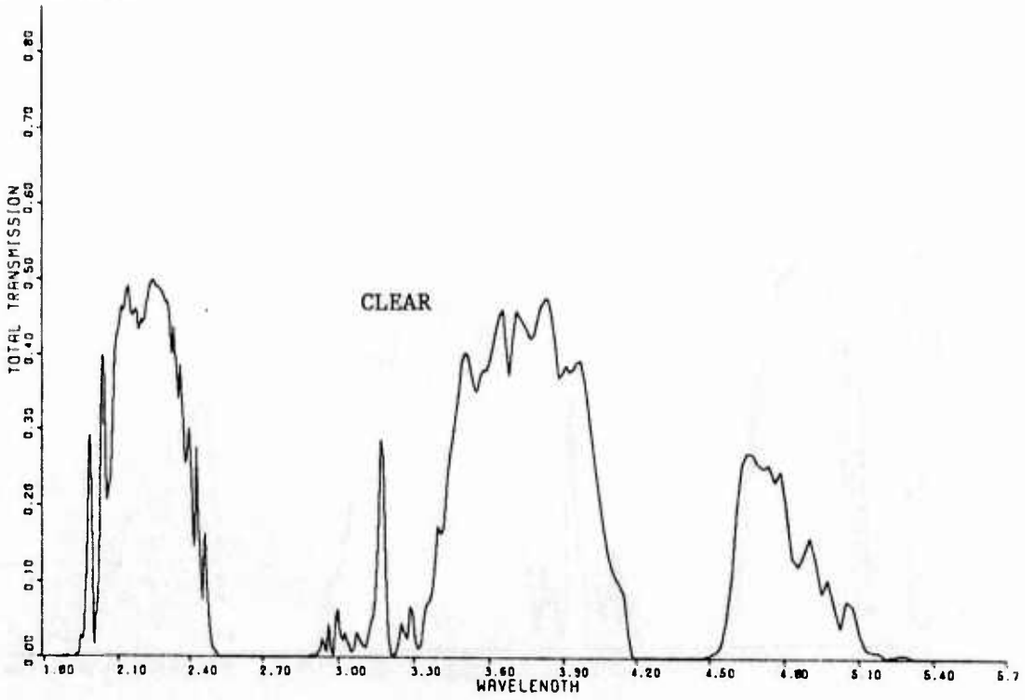

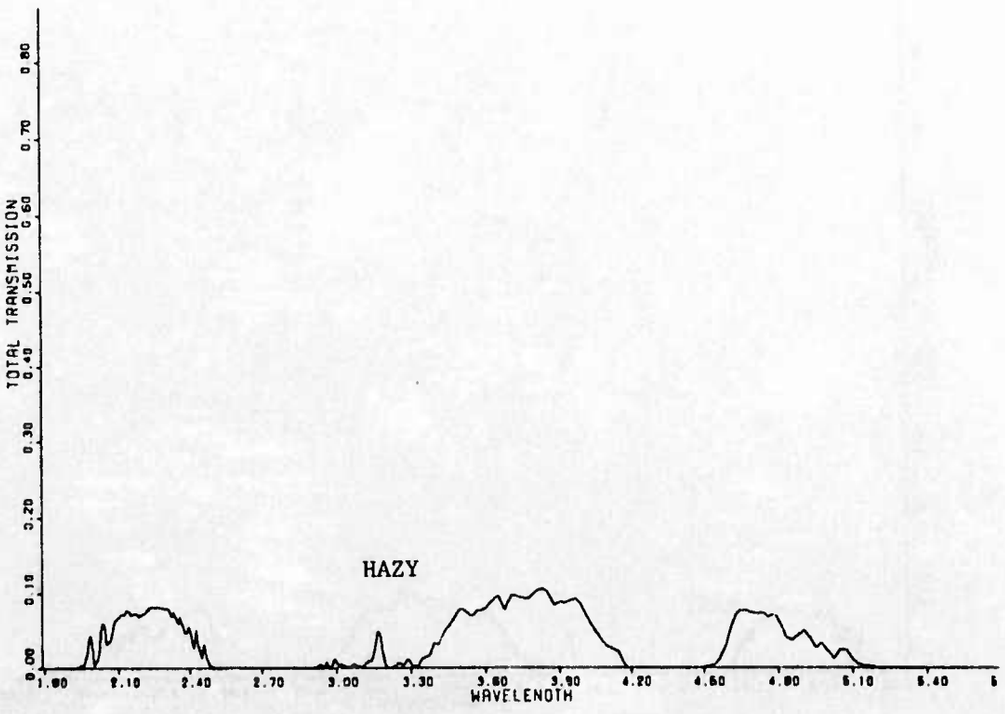

Mid-Range IR Computer-Calculated Band Transmittance over 66-km Slant Path, Mid-Latitude Winter Model, Estimated Marine Aerosol Model.

Set V (cont.)

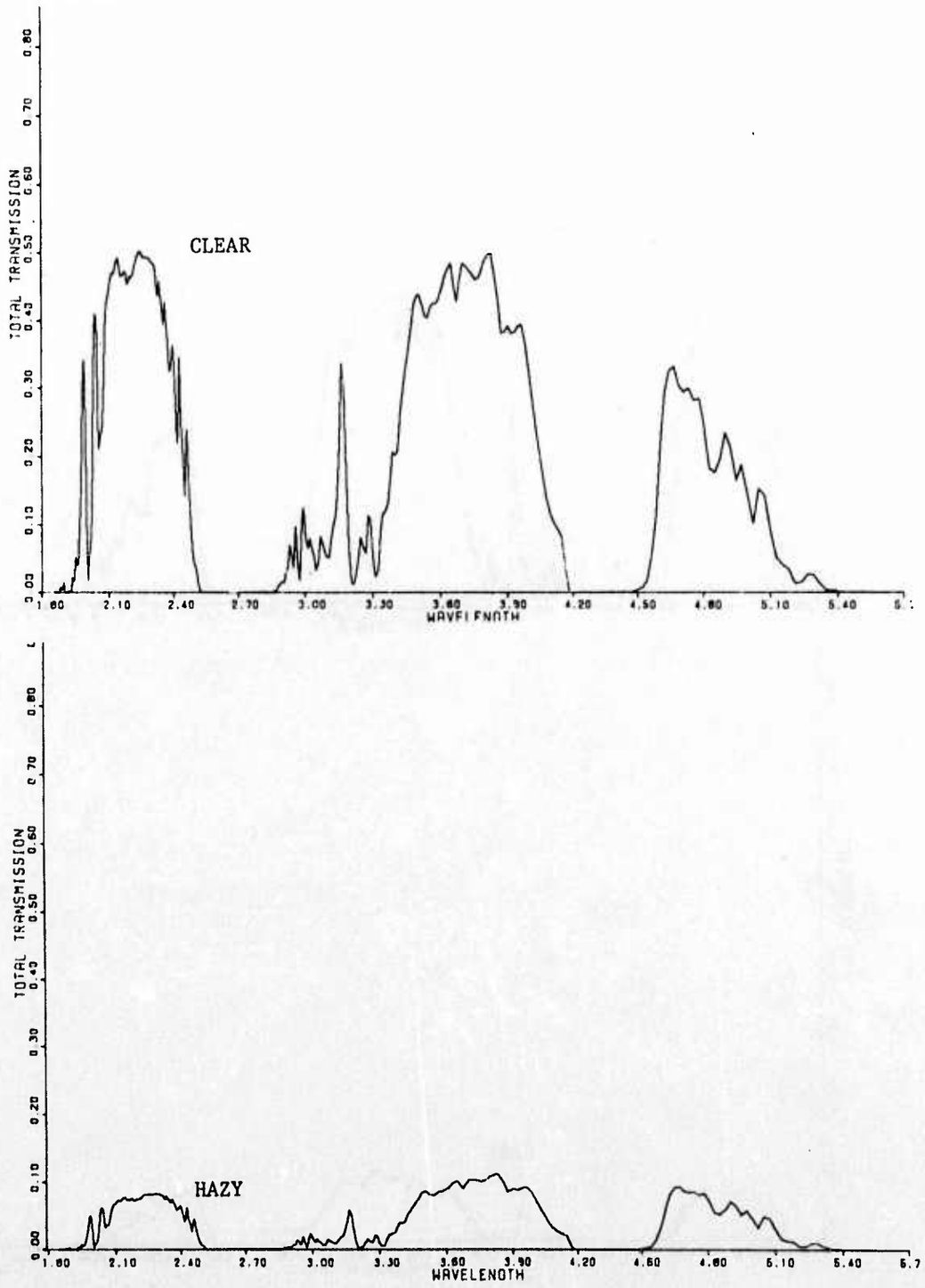

Mid-Range IR Computer-Calculated Band Transmittance over 66-km Slant Path, Sub-Arctic Winter Model, Estimated Marine Aerosol Model.

Set VI (Modified LOWTRAN 3 - Marine)

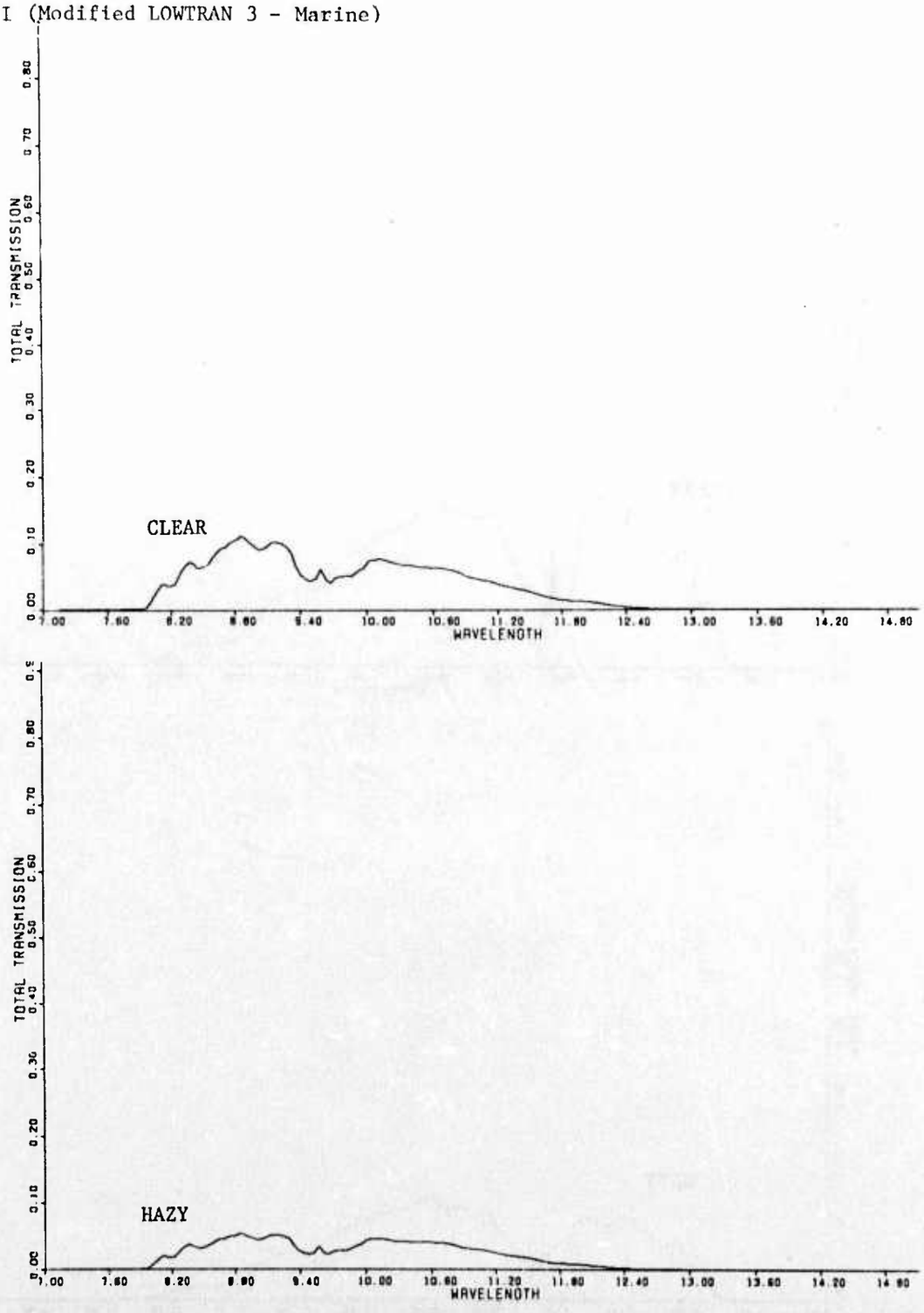

Long-Wave IR Computer-Calculated Band Transmittance over 66-km Slant Path, Tropical Atmosphere Model, Estimated Marine Aerosol Model.

Set VI (cont.)

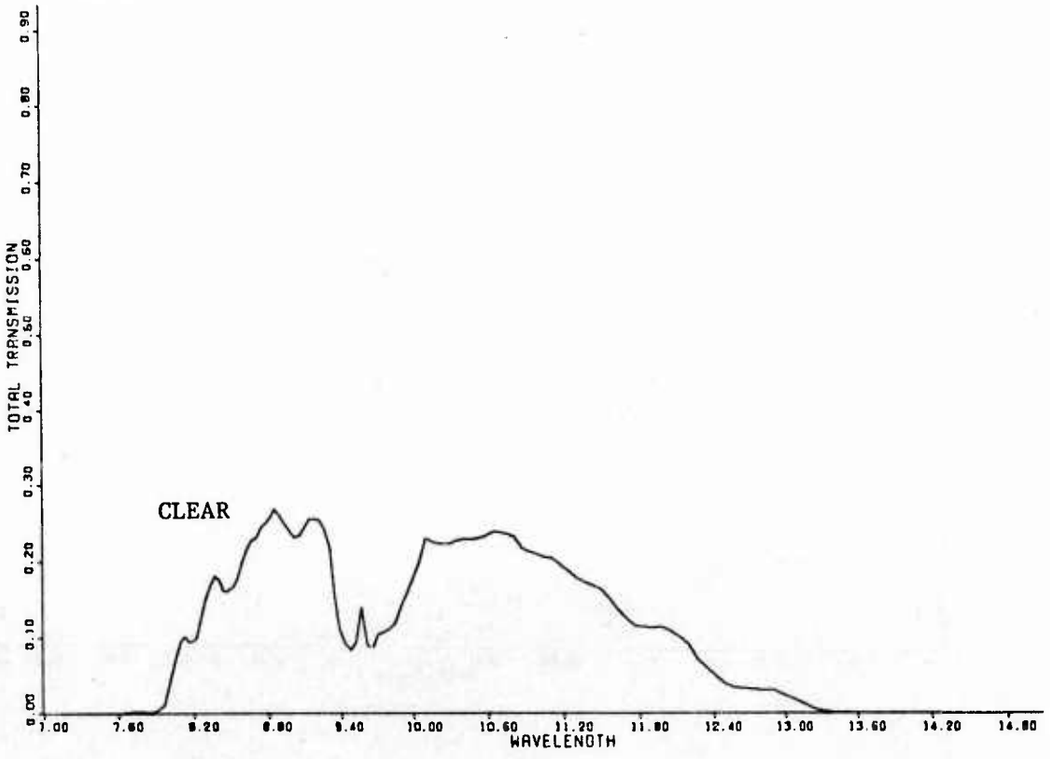

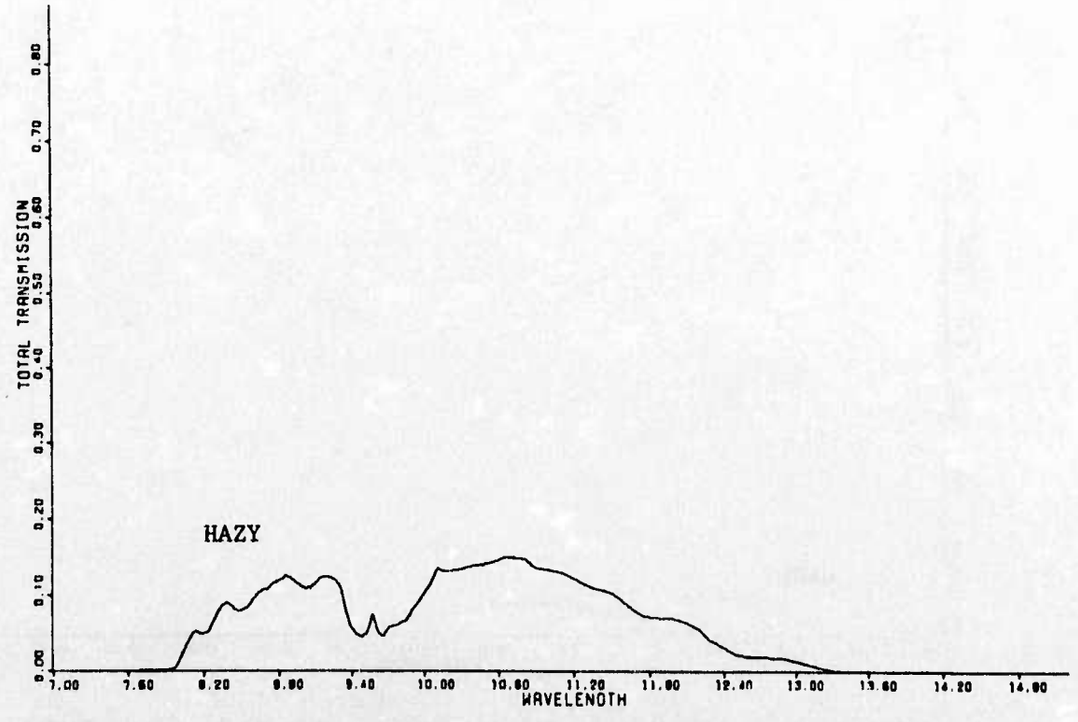

Long-Wave IR Computer-Calculated Band Transmittance over 66-km Slant Path, Mid-Latitude Summer Model, Estimated Marine Aerosol Model.

Set VI (cont.)

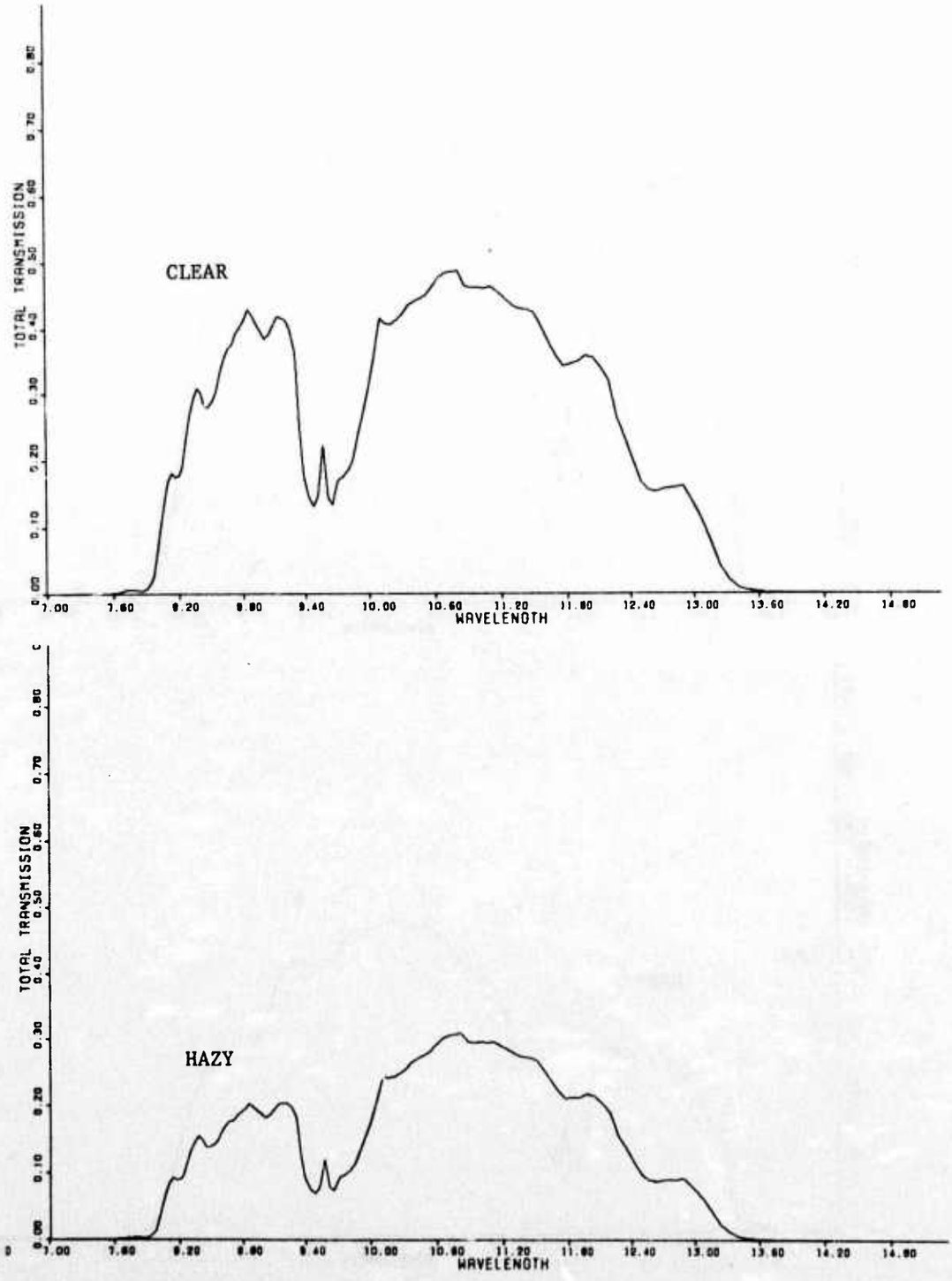

Long-Wave IR Computer-Calculated Band Transmittance over 66-km Slant Path, Sub-Arctic Summer Model, Estimated Marine Aerosol Model.

Set VI (cont.)

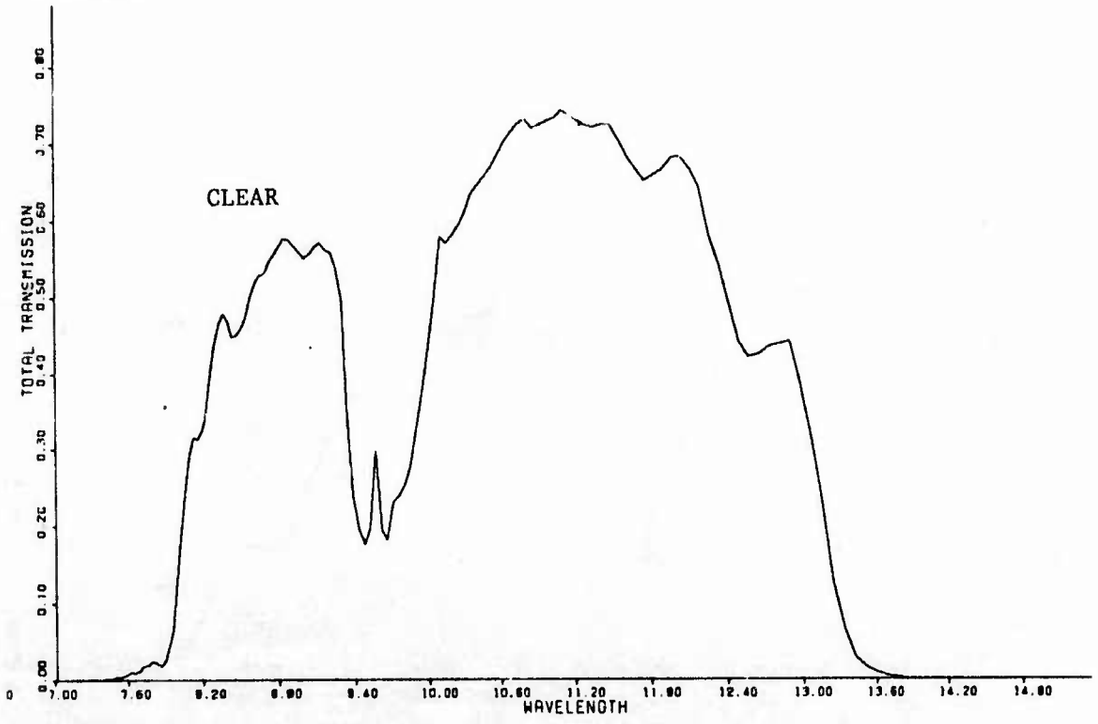

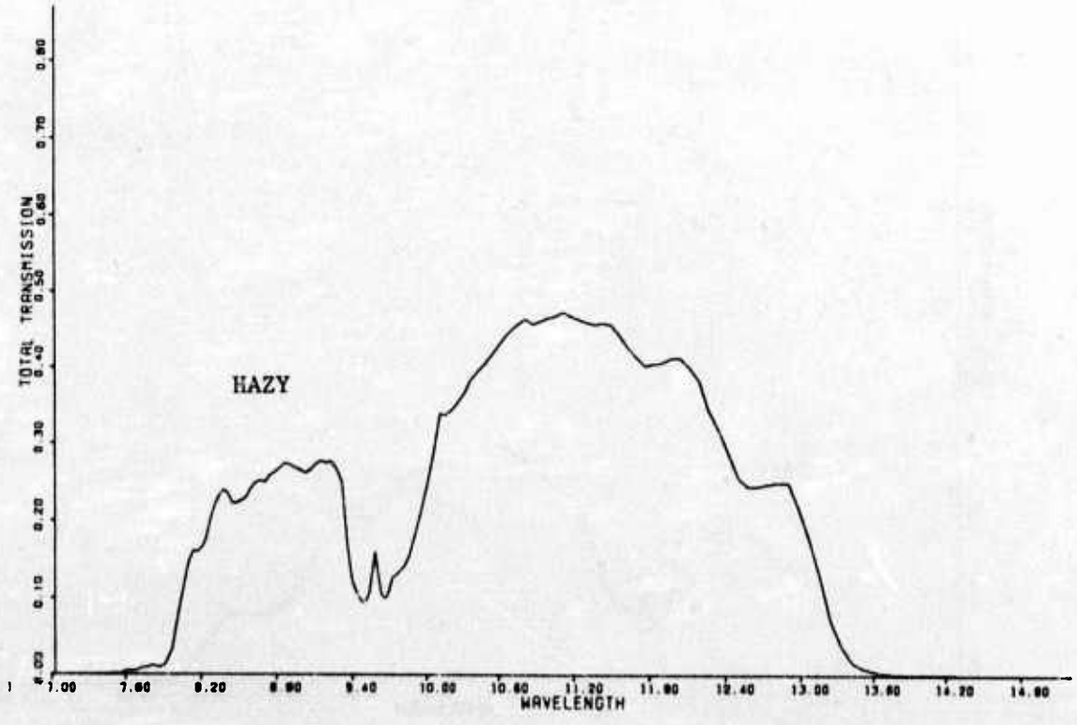

Long-Wave IR Computer-Calculated Band Transmittance over 66-km Slant Path, Mid-Latitude Winter Model, Estimated Marine Aerosol Model.

Set VI (cont.)

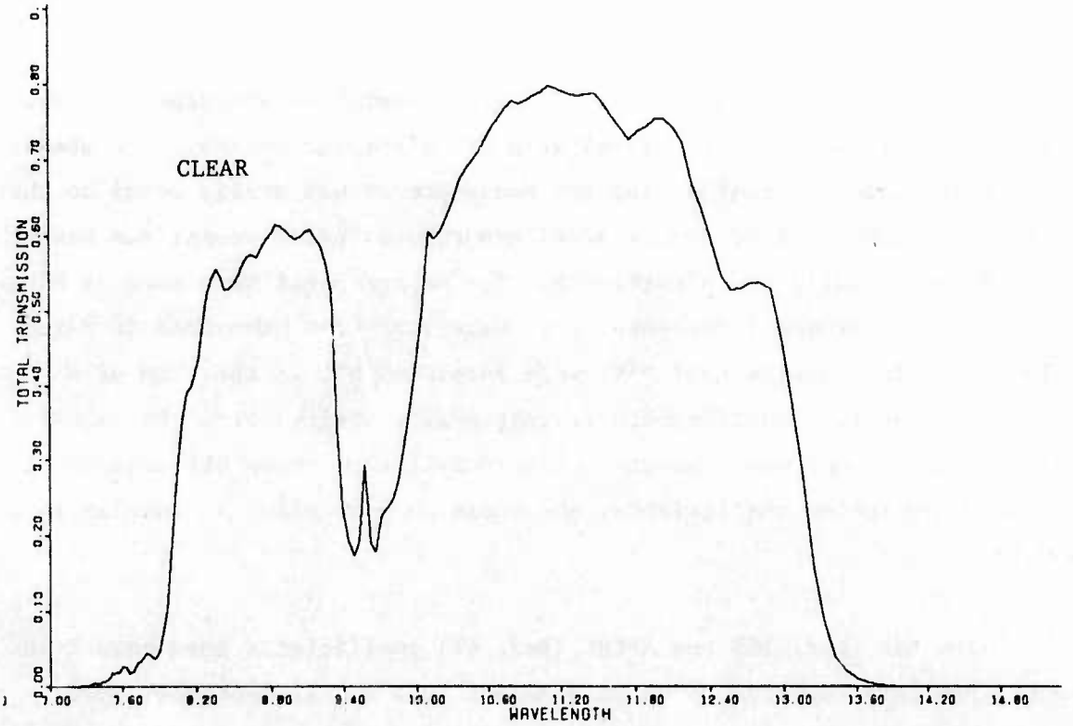

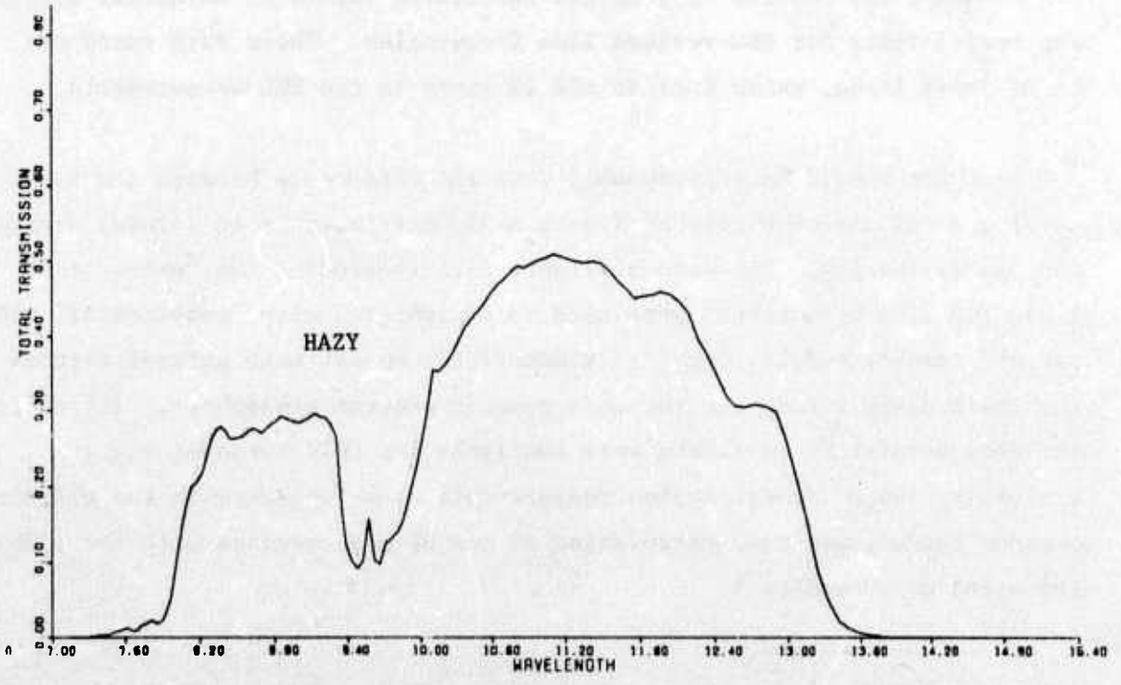

Long-Wave IR Computer-Calculated Band Transmittance over 66-km Slant Path, Sub-Arctic Winter Model, Estimated Marine Aerosol Model.

Section A-7

COMPARISON OF MEASURED AND CALCULATED DF LASER LINE TRANSMITTANCES

INTRODUCTION

Comparisons were made of a set of DF laser line atmospheric transmittance measurements, with several sets of calculated values. The atmospheric water vapor content during the measurements was nearly equal to that of the AFCRL mid-latitude summer model atmosphere; hence comparison with that model should be valid and significant. The measurements were made by NRL over a 5-kilometer sea level path (over water) at Cape Canaveral in March of 1975, and the results (Ref. 40) were furnished SRL in the form of a graph of attenuation coefficients (Figure A-21), derived from the experimental transmittance measurements. Figure A-21 also shows NRL-calculated molecular absorption coefficients, and these were supplied in tabular form as well.

The OSU (Ref. 16) and AFCRL (Ref. 41) coefficients used were from unpublished data supplied to us on 8 August 1975 and 11 September 1975, respectively, and consist of computer-calculated values of molecular absorption coefficients for OSU-revised line frequencies. These data encompass 36* DF laser lines, which include the 22 lines in the NRL measurements.

There should be a reasonably constant difference between the experimental and calculated curves of Figure A-21, attributable to aerosol absorption and scattering. The data of Figure A-21 (including the "extinction" values for 1.06 micrometer) were used in conjunction with "continental" and "marine" aerosol models (previously described) to estimate aerosol attenuation coefficient values for the measurements program atmosphere. (It would have been helpful if more data were available for this purpose; e.g., "visibility range" or extinction measurements at a frequency in the visible spectrum region, and time correlation of the DF measurements with the 1.06 micrometer measurements.)

---

*The AFCRL table for the DF laser 1-0 P(9) is erroneous; hence valic data cover 35 lines.

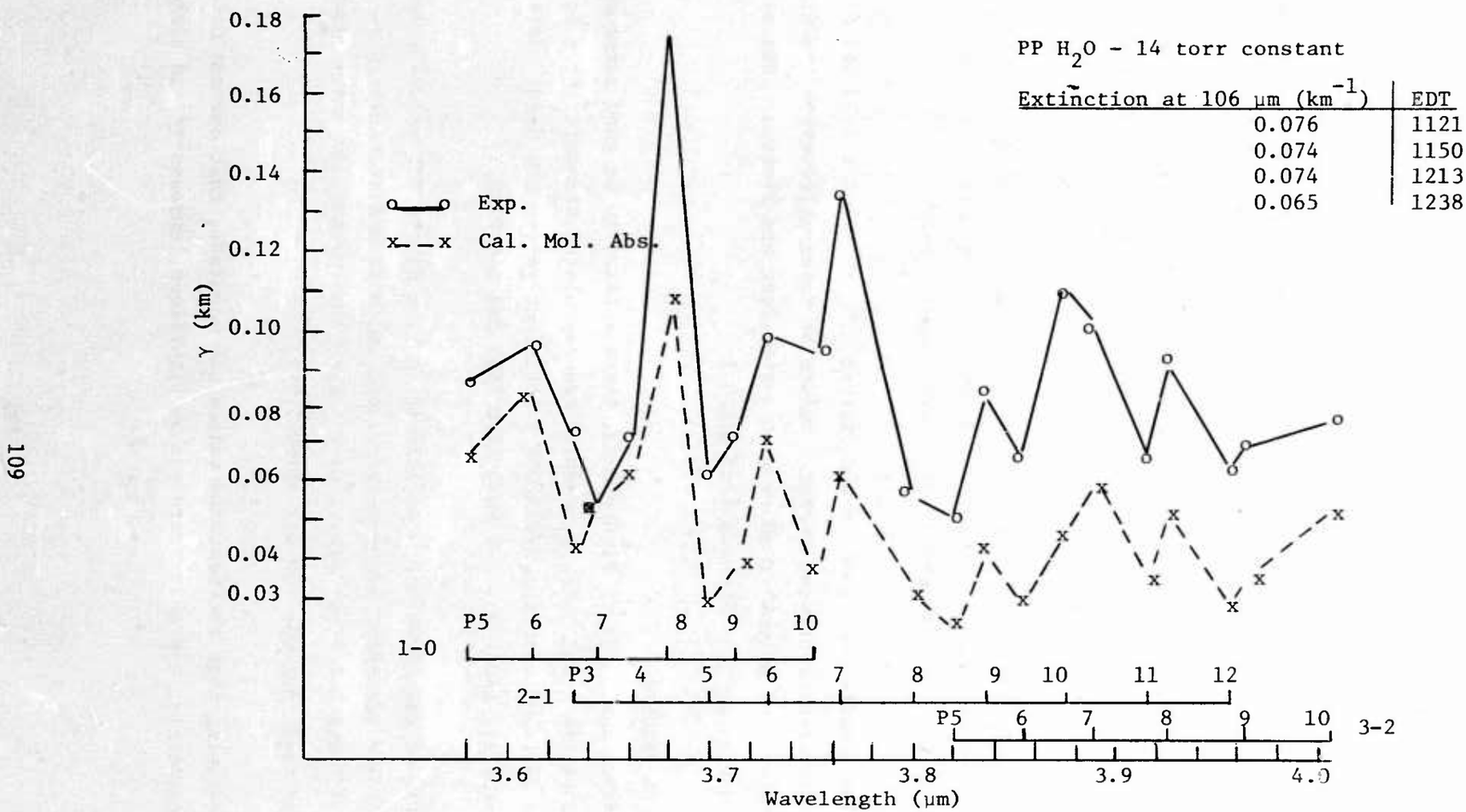

Figure A-21. Preliminary DF Extinction Data, CCAFS, 5.08 km

RESULTS

Perhaps the most meaningful comparison of measured and calculated values is that of Figure A-22. This bar graph shows the following values, respectively, for each of the 22 DF laser lines:

1. The NRL-measured transmittance for their 5-kilometer sea level path, as derived from coefficient values scaled from Figure A-21.

2. A transmittance value based upon NRL-calculated molecular absorption coefficients, together with the estimate of the aerosol attenuation coefficient (γ_a) for the test path.

3. A transmittance value based upon AFCRL-calculated molecular absorption coefficients for the revised OSU line frequencies, together with the SRL estimate of aerosol attenuation coefficient.

The results are shown in a different form in Figures A-23 and A-24, in which differences between measured values of total attenuation coefficient (γ) and calculated molecular absorption coefficient are plotted. Figure A-23 was copied from an NRL-supplied graph.)

COMMENTS ON RESULTS

Referring again to Figure A-22, there appears to be good agreement (T values within 0.05) between measured and calculated transmittances for 17 of the 22 lines when the AFCRL/OSU coefficient values are used. [All except 1-0 P(6), 1-0 P(7), 2-1 P(4), 1-0 P(8) and 1-0 P(10).]

Use of the AFCRL/OSU coefficients in lieu of the NRL values results in much closer agreement between calculated and measured transmittances for the 2-1 P(7) and 2-1 P(10) lines, with lesser improvement for three other lines, and small degradation for three lines.

Assuming that the measured values are accurate, that our estimate of γ_a is reasonable, and that there was no significant unmeasured and unknown

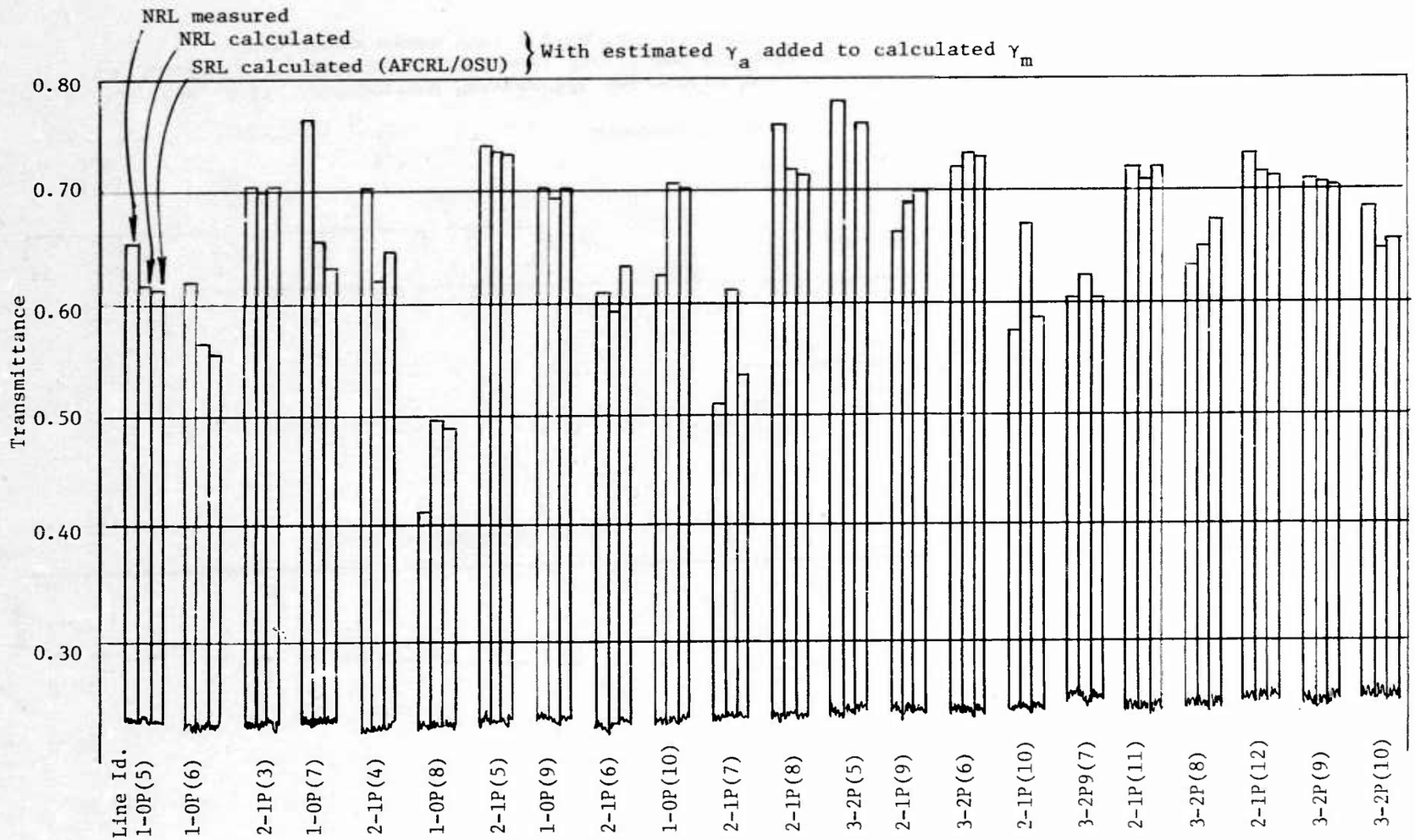

Figure A-22. Measured and Calculated Transmittances of 22 DF Laser Lines Over 5-Kilometer Sea Level Path

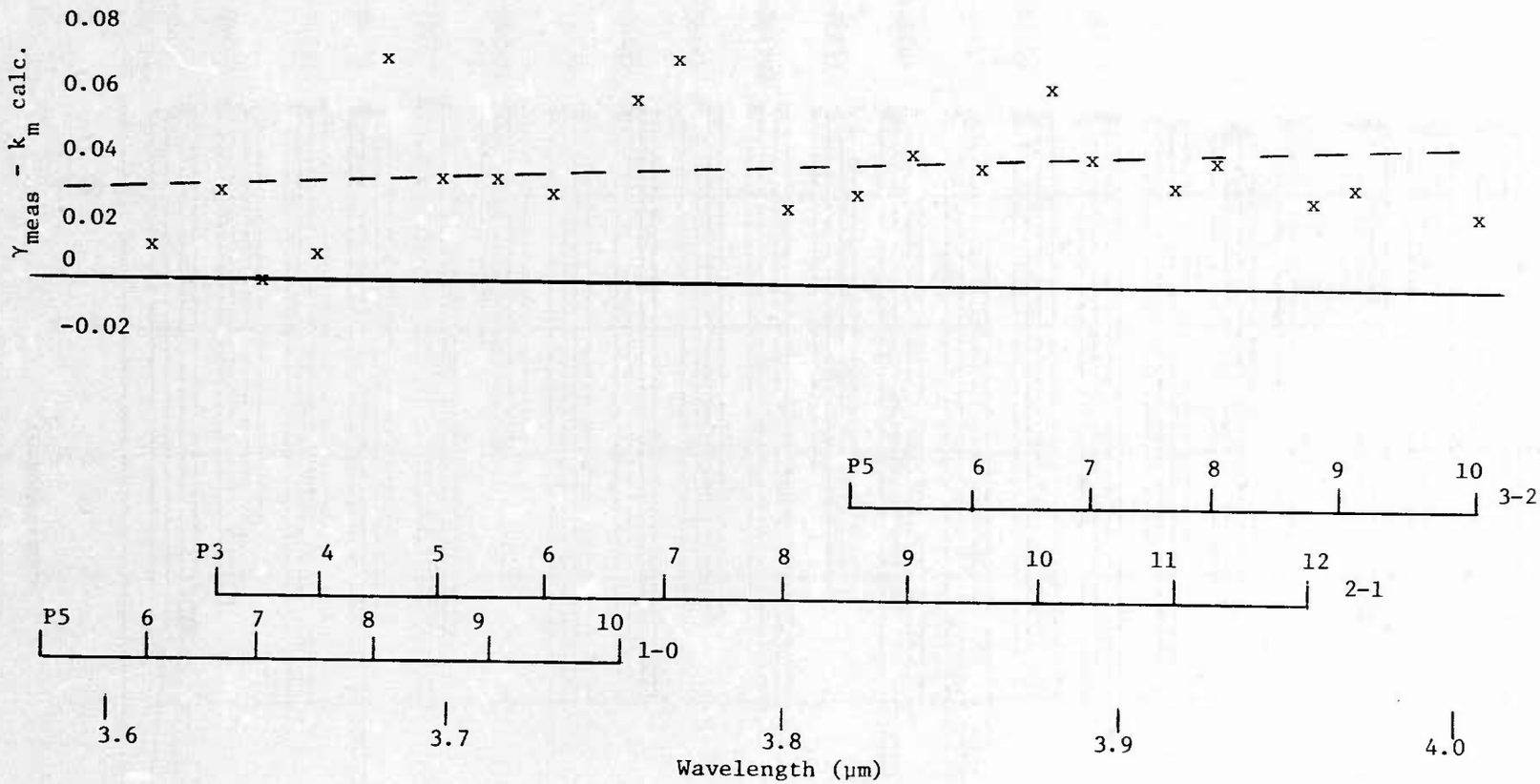

Figure A-23. Differences Between NRL Calculated Sea Level Molecular Absorption Coefficients (Mid-Latitude Summer Model) and Attenuation Coefficients Derived From Measurements Over a 5-km Path at CCAFS (22 DF Laser Lines)

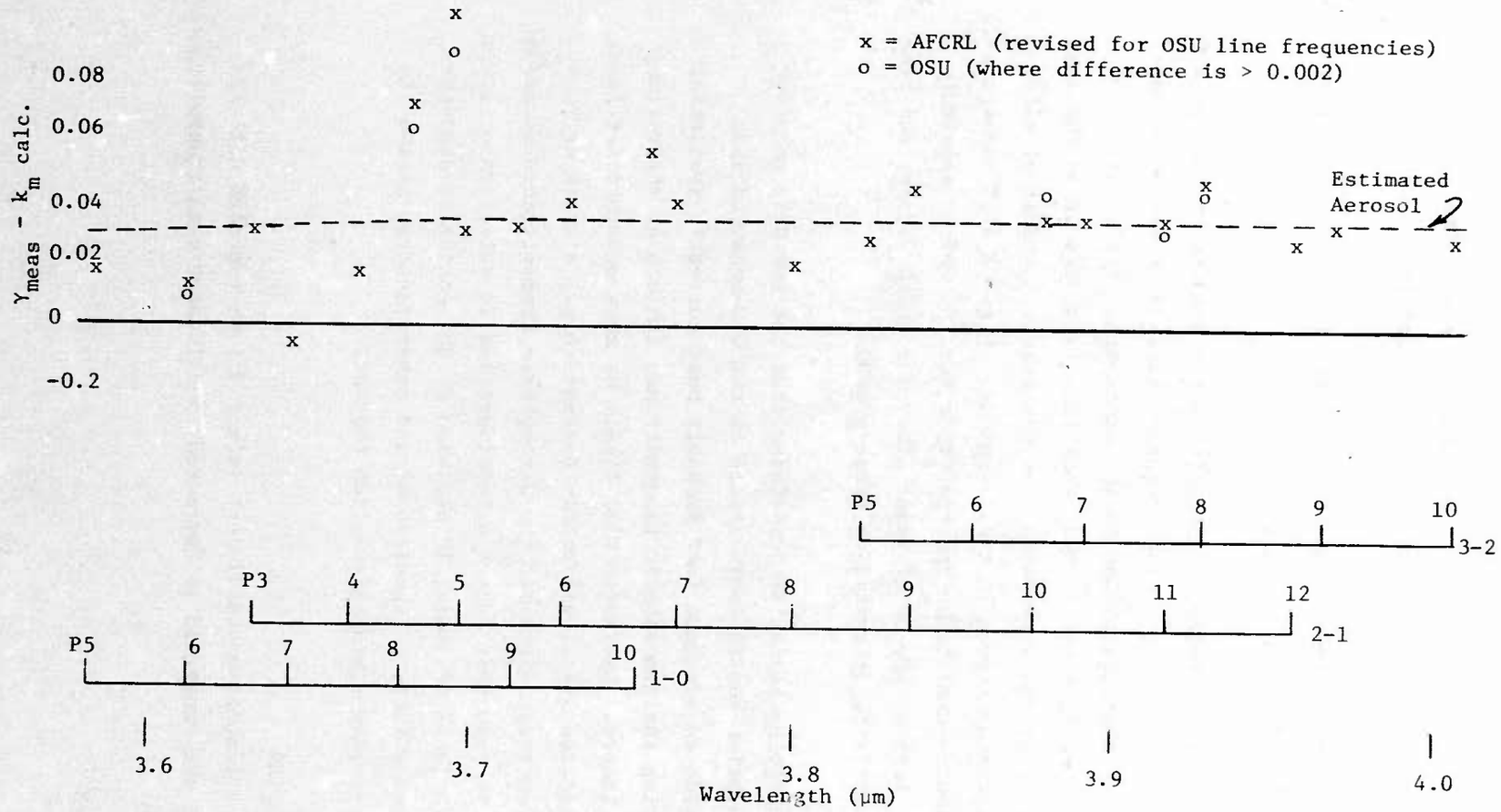

Figure A-24. Differences Between AFCRL/OSU Calculated Sea Level Molecular Absorption Coefficients (Mid-Latitude Summer Model) and Attenuation Coefficients Derived from NRL Measurements Over a 5-km Path at CCAFS (22 DF Laser Lines)

disparity between the test atmosphere and the mid-latitude summer model, the following conclusions are postulated with regard to calculations of DF laser atmospheric transmittance using the AFCRL/OSU coefficients.

1. Calculated transmittances for 1-0 P(8) and 1-0 P(10) may be significantly high.

2. Calculated transmittances for 1-0 P(6), 1-0 P(7), and 2-1 P(4) may be significantly low.

In each case where there is a significant disparity between measured and calculated values, the laser line frequency lies on or near a steep slope of a molecular absorption line in the atmospheric transmission spectrum. Hence a very small error in the laser line frequency or in the spectral characteristics of the absorption line can make a significant difference in the calculated transmittance in these regions. Figures A-25 through A-29 are high resolution transmittance spectra (from Ref. 3) which illustrate this phenomenon. Each of the 36 DF laser lines for which OSU-revised line frequencies are available is marked on these graphs.

On the foregoing basis, SRL concludes that the recently computed OSU or AFCRL absorption coefficients (based on the OSU-measured line frequencies) provide an adequate (and probably best currently available) basis for estimating the atmospheric transmittance (molecular absorption component) of DF lasers. Estimates will likely be more accurate for laser lines whose frequencies are significantly distant (e.g., a tenth or so of a wave number) from steep slopes in the atmospheric transmittance spectrum. It would be well to make this factor a consideration in selection of laser lines for an operational DF laser, in addition to the estimated atmospheric transmittance (over a range of conditions) and other factors involved in overall system performance and calculation thereof.

METHOD OF CALCULATION

Measured attenuation coefficient values (γ) were scaled directly from Figure A-21, and converted to "measured" 5-kilometer path transmittances by the expression

$$T = e^{-\gamma R}$$

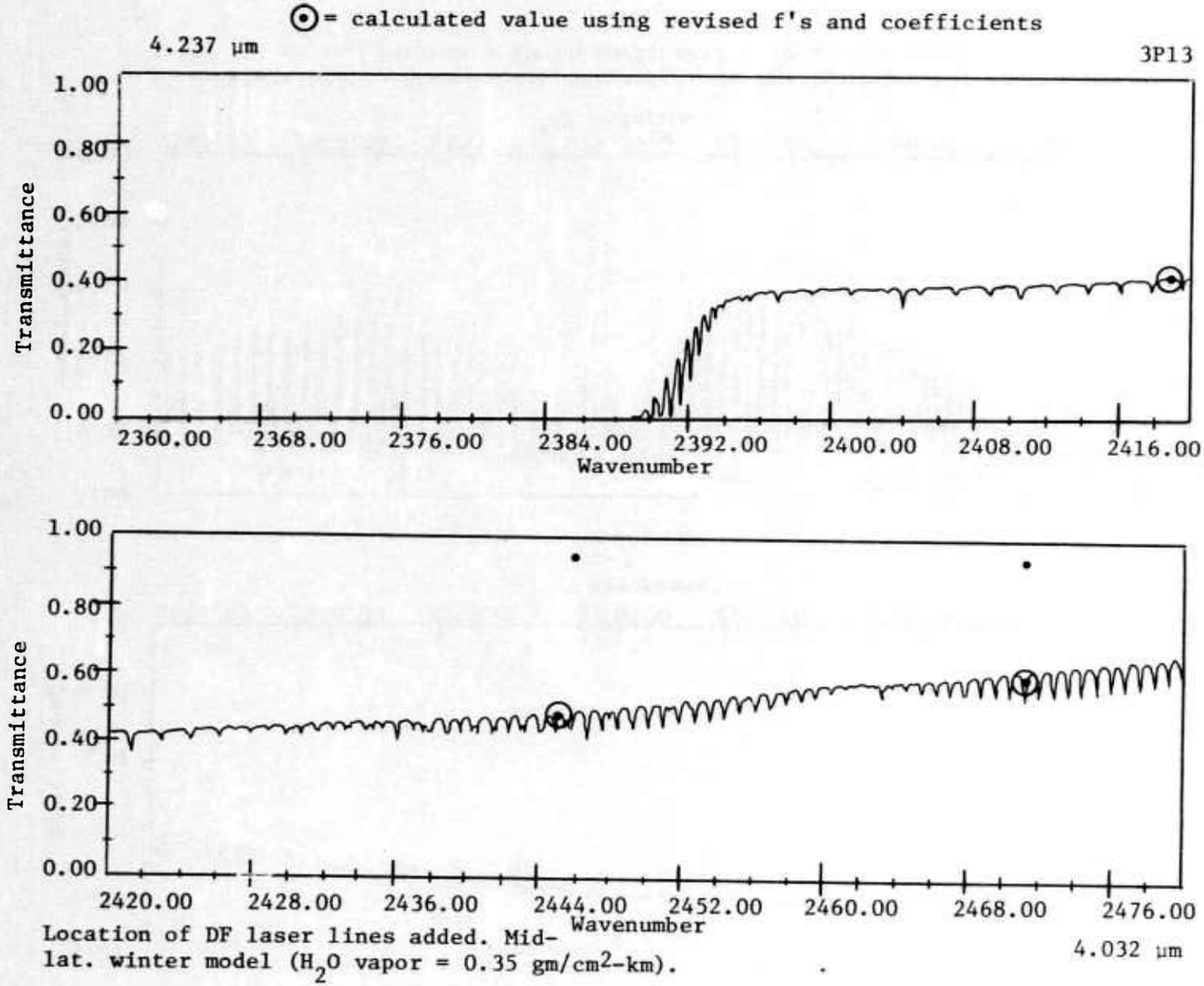

Location of DF laser lines added. Mid-lat. winter model (H_2O vapor = 0.35 gm/cm^2-km).

Figure A-25. Atmospheric Transmittance Due to Molecular Absorption Through a 10-km Horizontal Path at Sea Level

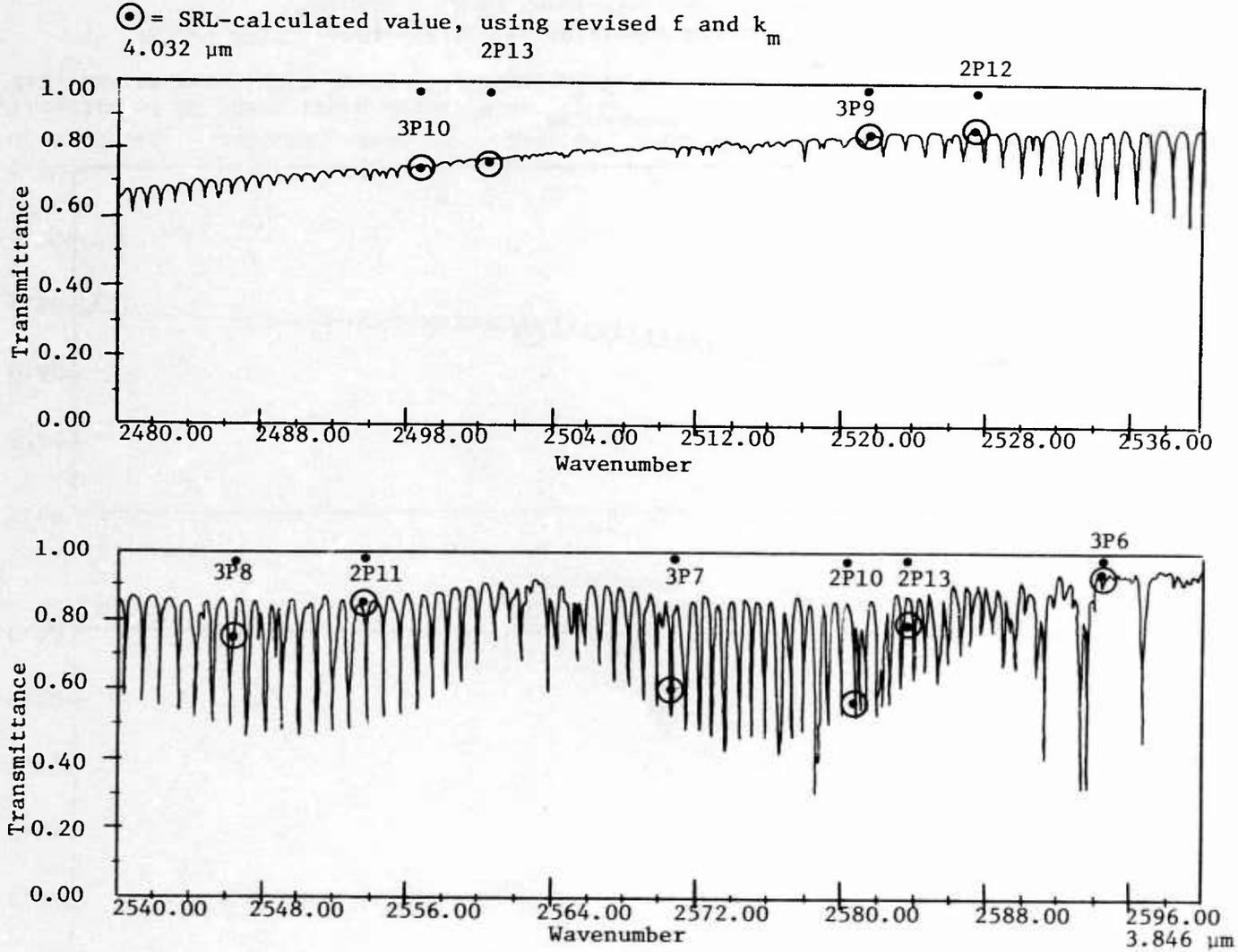

Figure A-26. Atmospheric Transmittance Due to Molecular Absorption Through a 10-km Horizontal Path at Sea Level

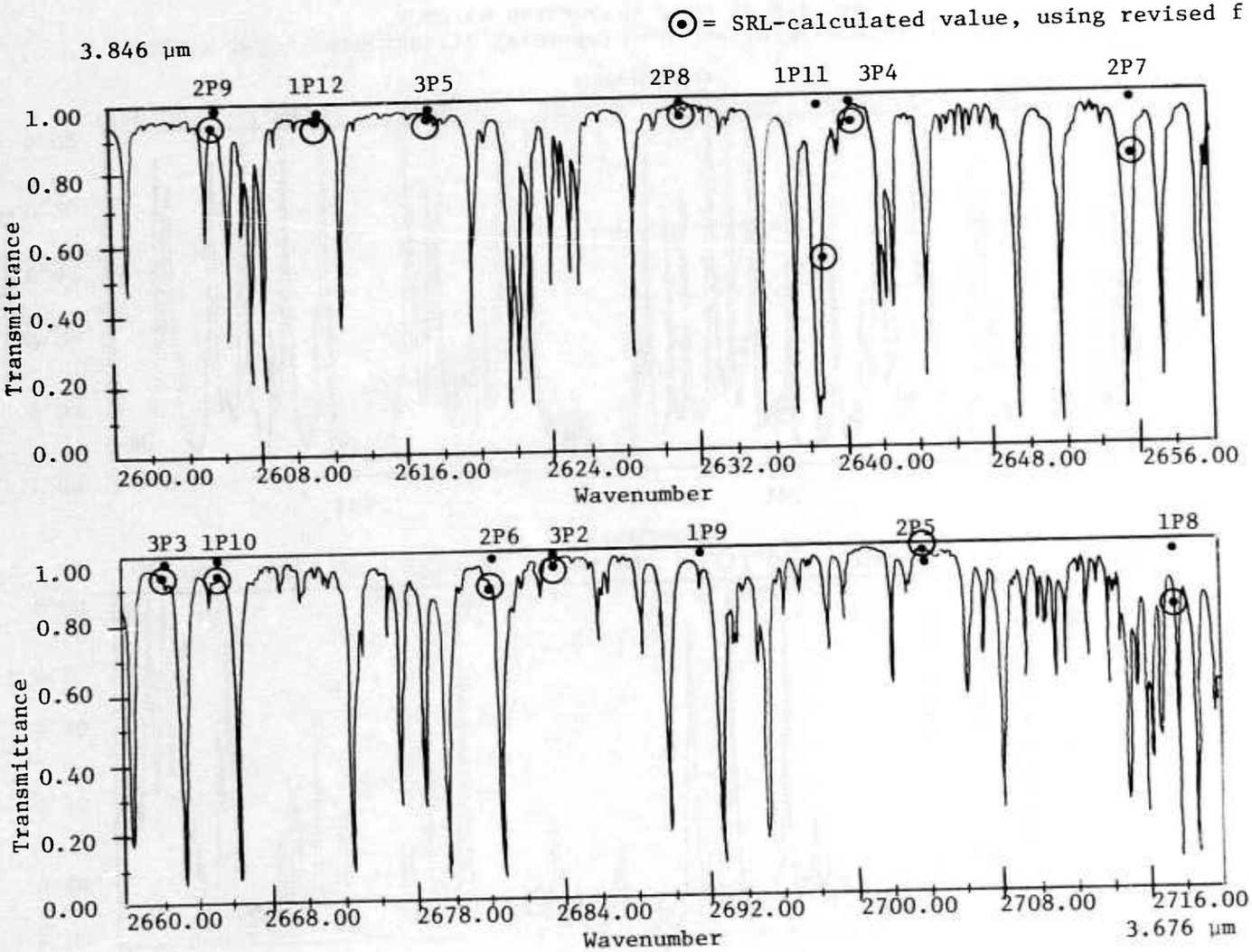

Figure A-27. Atmospheric Transmittance Due to Molecular Absorption Through a 10-km Horizontal Path at Sea Level

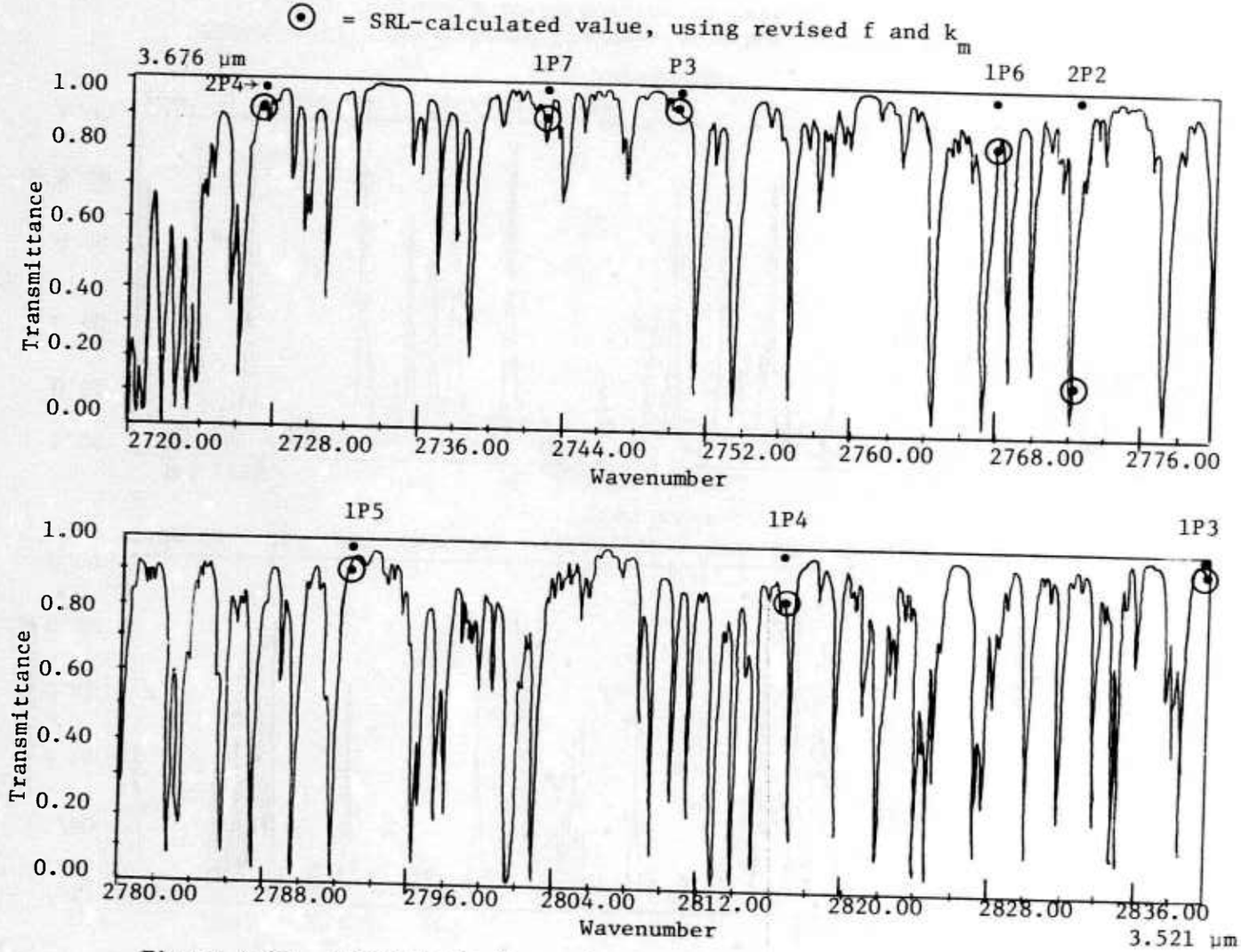

Figure A-28. Atmospheric Transmittance Due to Molecular Absorption Through a 10-km Horizontal Path at Sea Level

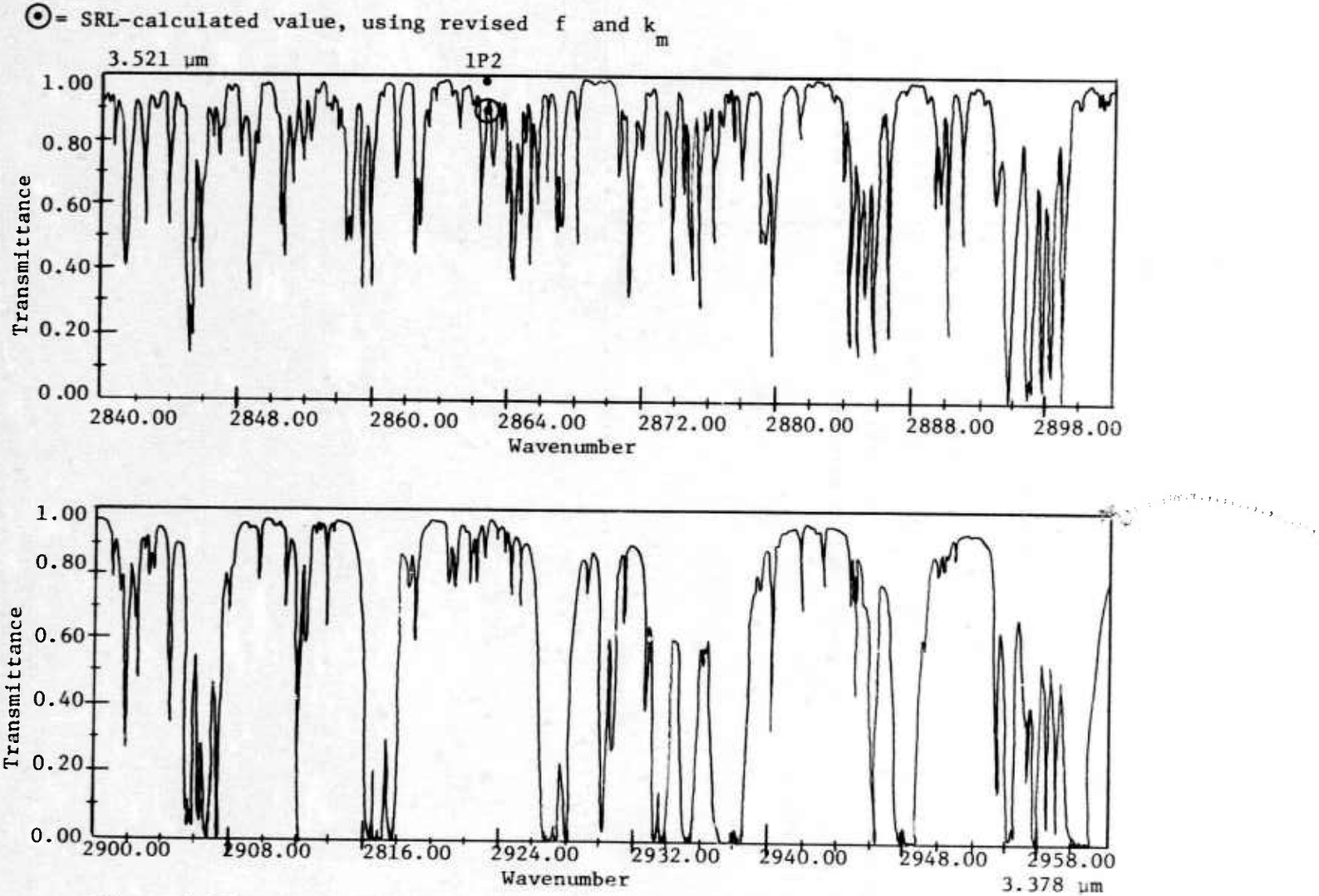

Figure A-29. Atmospheric Transmittance Due to Molecular Absorption Through a 10-km Horizontal Path at Sea Level

OSU-calculated and NRL-calculated values of molecular absorption coefficients were taken directly from tabled values supplied by OSU (Ref. 16) and NRL (Ref 40). Since the AFCRL values did not include water vapor continuum, OSU-reported values of this coefficient were added to the AFCRL molecular absorption coefficients.

Tables A-15 and A-16 summarize the calculations supporting the graphical presentation of results. Table A-17 is a copy of the OSU laser line frequencies and coefficients compilation. Table A-18 is a tabulation of molecular absorption coefficients by altitude layers, for the 2-1 P(7) DF laser line. This is one of 36 such tables furnished by AFCRL (Ref. 41). These data replace the corresponding molecular absorption coefficient data of Reference 7.

Table A-15. Measured Attenuation Coefficients and Three Calculated Molecular Absorption Coefficients of 22 DF Laser Lines over 5-km SL Path

Line Id	γ NRL (meas'd)	γ* NRL (calc'd)	$\Delta\gamma$ NRL	γ* OSU (calc'd)	$\Delta\gamma$ OSU	γ** AFCRL* Revised (calc'd)	$\Delta\gamma$ AFCRL
3-2 P(10)	0.076	0.0532	0.0228	0.0491	0.0269	0.0503	0.0257
3-2 P(9)	0.069	0.0354	0.0336	0.0357	0.0333	0.0359	0.0331
2-1 P(12)	0.063	0.0337	0.0293	0.0351	0.0279	0.0340	0.0290
3-2 P(8)	0.091	0.0514	0.0396	0.0504	0.0406	0.0450	0.0460
2-1 P(11)	0.066	0.0351	0.0309	0.0365	0.0295	0.0323	0.0337
3-2 P(7)	0.101	0.0604	0.0406	0.0646	0.0364	0.0665	0.0345
2-1 P(10)	0.110	0.0468	0.0632	0.0693	0.0407	0.0727	0.0373
3-2 P(6)	0.066	0.0288	0.0372	0.0292	0.0368	0.0289	0.0371
2-1 P(9)	0.083	0.0415	0.0415	0.0397	0.0433	0.0383	0.0447
3-2 P(5)	0.050	0.0222	0.0278	0.0216	0.0284	0.0216	0.0284
2-1 P(8)	0.056	0.0327	0.0233	0.0344	0.0216	0.0345	0.0215
2-1 P(7)	0.134	0.0645	0.0695	0.0935	0.0405	0.0907	0.0433
1-0 P(10)	0.094	0.0366	0.0574	0.0371	0.0569	0.0370	0.0570
2-1 P(6)	0.099	0.0707	0.0283	0.0596	0.0394	0.0580	0.0410
1-0 P(9)	0.072	0.0403	0.0317	0.0377	0.0343		
2-1 P(5)	0.061	0.0282	0.0328	0.0286	0.0324	0.0288	0.0322
1-0 P(8)	0.178	0.1074	0.0706	0.115	0.0630	0.1102	0.0678
2-1 P(4)	0.071	0.0632	0.0078	0.0552	0.0158	0.0546	0.0164
1-0 P(7)	0.054	0.0533	0.0007	0.0604	-0.0064	0.0603	-0.0063
2-1 P(3)	0.071	0.0409	0.0301	0.0407	0.0303	0.0402	0.0308
1-0 P(6)	0.096	0.0849	0.0111	0.0874	0.0086	0.0833	0.0127
1-0 P(5)	0.086	0.0679	0.0181	0.0716	0.0144	0.0691	0.0169

*: All mid-latitude summer, sea level.

**: OSU values for H_2O continuum added.

$\Delta\gamma$'s are NRL-measured (-) calculated.

Table A-16. Measured Transmittances and Two Calculated Transmittances of 22 DF Laser Lines over 5-km SL Path (Mid-latitude Summer)

Line Id	T NRL** (meas'd)	Est'd γ_a	T NRL (calc'd)	T SRL* (calc'd)
3-2 P(10)	0.684	0.034	0.647	0.656
3-2 P(9)	0.708	0.034	0.707	0.705
3-1 P(12)	0.730	0.034	0.713	0.712
3-2 P(8)	0.634	0.034	0.652	0.674
2-1 P(11)	0.719	0.034	0.708	0.718
3-2 P(7)	0.604	0.034	0.624	0.605
2-1 P(10)	0.577	0.034	0.668	0.587
3-2 P(6)	0.719	0.034	0.731	0.730
2-1 P(9)	0.660	0.034	0.686	0.697
3-2 P(5)	0.779	0.034	0.755	0.757
2-1 P(8)	0.756	0.034	0.716	0.710
2-1 P(7)	0.512	0.034	0.611	0.536
1-0 P(10)	0.625	0.034	0.703	0.701
2-1 P(6)	0.610	0.034	0.592	0.631
1-0 P(9)	0.700	0.034	0.690	0.699
2-1 P(5)	0.737	0.034	0.733	0.731
1-0 P(8)	0.411	0.033	0.496	0.489
2-1 P(4)	0.701	0.033	0.618	0.645
1-0 P(7)	0.763	0.032	0.653	0.630
2-1 P(3)	0.701	0.031	0.698	0.700
1-0 P(6)	0.619	0.030	0.563	0.556
1-0 P(5)	0.651	0.029	0.616	0.612

*: Using revised OSU line frequencies and revised AFCRL coefficients (11 September 1975).

**: Based upon NRL graph of measured γ's.

Table A-17. Mid-Latitude Summer Sea Level Absorption Coeffients Calculated from AFCRL Line Data*

*OSU compilation

(cm^{-1})(a)	Id	N_2O (km^{-1})	CH_4 (km^{-1})	CO_2 (km^{-1})	HDO (km^{-1})	H_2O (km^{-1})	H_2O & HDO (km^{-1})	H_2O Cont(b) (km^{-1})	N_2(b) (km^{-1})	Total (km^{-1})
2419.070	3-2 P(13)	8.36E-5	1.79E-9	3.75E-4	2.64E-5	6.54E-5	9.17E-5	3.26E-2	8.1 E-2	1.14E-1
2445.356	3-2 P(12)	1.98E-3	4.26E-9	3.17E-3	2.72E-6	2.64E-5	2.90E-5	2.85E-2	6.6 E-2	1.02E-1
2471.245	3-2 P(11)	5.32E-3	1.96E-8	4.73E-5	6.07E-5	4.28E-3	4.34E-3	2.52E-2	4.6 E-2	8.09E-2
2496.721	3-2 P(10)	5.13E-4	1.17E-5	3.57E-8	3.95E-5	8.80E-4	9.20E-4	2.27E-2	2.5 E-2	4.91E-2
2500.428	2-1 P(13)	4.83E-4	2.85E-6	1.34E-8	6.43E-5	6.26E-5	1.27E-4	2.25E-2	2.5 E-2	4.81E-2
2521.769	3-2 P(9)	4.86E-4	2.69E-6	2.62E-7	1.66E-4	4.55E-5	2.12E-4	2.05E-2	1.5 E-2	3.57E-2
2527.391	2-1 P(12)	7.92E-4	1.82E-5	2.29E-7	2.89E-4	3.78E-6	2.92E-4	2.00E-2	1.4 E-2	3.51E-2
2546.375	3-2 P(8)	2.15E-2	1.11E-3	1.55E-7	1.13E-3	4.44E-5	1.18E-3	1.86E-2	8.0 E-3	5.04E-2
2553.953	2-1 P(11)	1.06E-2	7.67E-5	1.35E-7	5.07E-4	4.70E-6	5.12E-4	1.82E-2	7.1 E-2	3.65E-2
2570.522	3-2 P(7)	3.76E-2	3.20E-5	1.03E-7	4.53E-3	4.69E-5	4.58E-3	1.74E-2	5.0 E-3	6.46E-2
2580.097	2-1 P(10)	4.60E-2	2.50E-6	9.00E-8	2.65E-3	5.52E-6	2.66E-3	1.70E-2	3.6 E-3	6.93E-2
2583.486	1-0 P(13)	2.17E-2	4.88E-6	8.59E-8	3.77E-3	1.92E-4	3.79E-3	1.69E-2	3.45E-3	4.58E-2
2594.198	3-2 P(6)	2.26E-3	2.10E-5	7.46E-8	7.18E-3	3.54E-4	7.53E-3	1.68E-2	2.6 E-3	2.92E-2
2605.807	2-1 P(9)	5.02E-4	1.81E-4	6.47E-8	1.99E-2	6.75E-6	1.99E-2	1.68E-2	2.3 E-3	3.97E-2
2611.142	1-0 P(12)	8.89E-5	3.70E-6	6.08E-8	5.87E-3	2.53E-5	5.90E-3	1.70E-2	2.1 E-3	2.51E-2
2617.386	3-2 P(5)	1.11E-5	1.41E-5	5.67E-8	2.37E-3	3.98E-5	2.41E-3	1.72E-2	2.0 E-3	2.16E-2
2631.068	2-1 P(8)	4.65E-8	8.46E-4	4.90E-8	9.12E-3	4.73E-3	1.39E-2	1.78E-2	1.9 E-3	3.44E-2
2638.392	1-0 P(11)	2.04E-9	6.16E-4	4.56E-8	2.51E-1	7.63E-4	2.51E-1	1.82E-2	1.6 E-3	2.71E-1
2640.074	3-2 P(4)	5.73E-10	1.20E-4	4.48E-8	2.92E-2	4.64E-5	2.93E-2	1.83E-2		4.77E-2
2655.863	2-1 P(7)	1.11E-11	7.15E-4	3.86E-8	7.35E-2	4.42E-6	7.35E-2	1.93E-2		9.35E-2
2662.246	3-2 P(3)	1.31E-11	1.25E-5	3.65E-8	1.94E-2	3.13E-5	1.94E-2	1.98E-2		3.92E-2
2665.219	1-0 P(10)	1.42E-11	1.98E-3	3.56E-8	1.51E-2	9.80E-6	1.5 E-2	2.00E-2		3.71E-2
2680.179	2-1 P(6)	2.30E-11	3.06E-4	3.14E-8	3.79E-2	2.34E-4	3.81E-2	2.12E-2		5.96E-2
2683.890	3-2 P(2)	2.64E-11	4.80E-4	3.04E-8	3.12E-3	5.66E-5	3.18E-3	2.15E-2		2.52E-2
2691.607	1-0 P(9)	3.66E-11	3.24E-3	2.86E-8	1.21E-2	3.72E-4	1.25E-2	2.20E-2		3.77E-2
2703.999	2-1 P(5)	7.12E-11	1.82E-6	2.61E-8	5.61E-3	1.12E-5	5.62E-3	2.30E-2		2.86E-2
2717.539	1-0 P(8)	9.34E-10	2.12E-6	2.36E-8	9.10E-2	7.56E-5	9.11E-2	2.41E-2		1.15E-1
2727.309	2-1 P(4)	1.60E-8	1.42E-4	2.21E-8	2.99E-2	1.27E-4	3.00E-2	2.51E-2		5.52E-2
2742.998	1-0 P(7)	4.31E-6	2.88E-4	1.99E-8	3.32E-2	4.75E-5	3.32E-2	2.69E-2		6.04E-2
2750.094	2-1 P(3)	4.13E-5	9.54E-4	1.90E-8	1.22E-2	4.66E-5	1.22E-2	2.75E-2		4.07E-2
2767.968	1-0 P(6)	1.02E-4	5.00E-3	1.70E-8	5.14E-2	6.87E-5	5.15E-2	3.08E-2		8.74E-2
2772.340	2-1 P(2)	1.05E-3	1.25E-3	1.66E-8	6.93E-1	1.04E-3	6.94E-1	3.14E-2		7.29E-1
2792.434	1-0 P(5)	8.03E-4	6.18E-4	1.48E-8	3.50E-2	1.55E-4	3.52E-2	3.50E-2		7.16E-2
2816.380	1-0 P(4)	1.16E-3	2.85E-3	1.30E-8	5.84E-2	1.60E-3	6.00E-2	4.00E-2		1.04E-1
2839.791	1-0 P(3)	3.24E-7	8.05E-4	1.15E-8	2.74E-2	2.44E-4	2.76E-2	4.50E-2		7.34E-2
2862.653	1-0 P(2)	7.60E-7	2.28E-3	1.03E-8	3.85E-2	1.59E-3	4.01E-2	5.00E-2		9.24E-2

Table A-18. Molecular Absorption Coefficients by Altitude Layers, for DF Laser 2-1 P(7) Line

Wavelength = 3.765254 micrometers; Frequency = 2655.863 wave numbers.

Ht (km)	Tropical $k_m(km^{-1})$	Mid-latitude Summer $k_m(km^{-1})$	Mid-latitude Winter $k_m(km^{-1})$	Sub-arctic Summer $k_m(km^{-1})$	Sub-arctic Winter $k_m(km^{-1})$
0	9.47E-02	7.14E-02	2.06E-02	4.80E-02	8.62E-03
0 - 1	7.62E-02	5.67E-02	1.69E-02	3.80E-02	7.93E-03
1 - 2	4.99E-02	3.44E-02	1.13E-02	2.41E-02	6.33E-03
2 - 3	2.84E-02	1.94E-02	7.35E-03	1.52E-02	4.44E-03
3 - 4	1.32E-02	1.04E-02	4.30E-03	9.05E-03	2.83E-03
4 - 5	6.96E-03	5.50E-03	2.39E-03	5.20E-03	1.60E-03
5 - 6	4.13E-03	3.00E-03	1.37E-03	2.85E-03	8.75E-04
6 - 7	2.24Ej03	1.76E-03	7.40E-04	1.51E-03	5.20E-04
7 - 8	1.22E-03	1.03E-03	3.96E-04	7.85E-04	2.94E-04
8 - 9	6.31E-04	5.96E-04	2.41E-04	3.86E-04	1.85E-04
9 - 10	3.40E-04	3.53E-04	1.60E-04	2.02E-04	1.32E-04
10 - 11	1.87E-04	1.96E-04	1.12E-04	1.32E-04	9.47E-05
11 - 12	1.11E-04	1.11E-04	8.24E-05	9.31E-05	6.85E-05
12 - 13	7.49E-05	7.02E-05	5.79E-05	6.49E-05	4.93E-05
13 - 14	4.90E-05	4.95E-05	4.02E-05	4.66E-05	3.56E-05
14 - 15	3.62E-05	3.68E-05	2.94E-05	3.46E-05	2.59E-05
15 - 16	2.52E-05	2.60E-05	2.13E-05	2.42E-05	1.87E-05
16 - 17	1.58E-05	1.86E-05	1.56E-05	1.85E-05	1.37E-05
17 - 18	1.23E-05	1.37E-05	1.14E-05	1.37E-05	9.98E-06
18 - 19	8.93E-06	1.01E-05	8.25E-06	1.02E-05	7.29E-05
19 - 20	6.47E-06	7.45E-06	6.03E-06	7.59E-06	5.31E-06
20 - 21	4.81E-06	5.51E-06	4.51E-06	5.56E-06	3.88E-06
21 - 22	3.57E-06	4.13E-06	3.25E-06	4.16E-06	2.85E-06
22 - 23	2.62E-06	2.98E-06	2.44E-06	3.12E-06	2.09E-06
23 - 24	1.97E-06	2.38E-06	1.76E-06	2.34E-06	1.54E-06
24 - 25	1.50E-06	1.71E-06	1.38E-06	1.74E-06	1.14E-06
25 - 30	0.	0.	0.	0.	0.
30 - 35	0.	0.	0.	0.	0.
35 - 40	0.	0.	0.	0.	0.
40 - 45	0.	0.	0.	0.	0.
45 - 50	0.	0.	0.	0.	0.
50 - 70	0.	0.	0.	0.	0.
70 - 100	0.	0.	0.	0.	0.

Section A-8

COMPARISON OF MEASURED AND CALCULATED CO_2 LASER LINE TRANSMITTANCES

INTRODUCTION

Comparisons were made of a set of CO_2 laser line atmospheric transmittance measurements (Ref. 42), with several sets of calculated values. The measurements were made by NRL over a 5-kilometer sea level path (over water) at Cape Canaveral, and the results of the measurements were supplied to SRL in the form of a graph of attenuation coefficients derived from the experimental transmittance values. Calculated values for part of the lines were also included on the graph.

It was desired to compare the NRL-supplied data with estimated transmittances for the same path calculated for AFCRL model atmospheres. The NRL graph indicates measured path water vapor partial pressure and CO_2 concentration of 15.8 torr and 350 ppm, respectively, while NRL calculations were accomplished for 17 torr and 350 ppm. The AFCRL mid-latitude summer model has 14 gm/m^3 H_2O water vapor and the tropical model has 19 gm/m^3 H_2O vapor. The CO_2 concentration is fixed at 330 ppm in the AFCRL models. A partial pressure of one torr is approximately equivalent to 1 gm/m^3 H_2O at 20^o C, and departs but little from that value over a fairly wide temperature range. Then, since these two constituents are the principal absorbers in this wavelength region, the transmittance of the test path could be expected to be about midway between that of the mid-latitude summer and tropical model atmospheres.

Model atmosphere molecular absorption coefficient data (Ref. 4) were available for 12 of the CO_2 lines for which NRL measurements were made; hence comparisons were possible at those corresponding wavelengths. A nominal value of aerosol attenuation coefficient (0.013 per km) for a normalized clear atmosphere was added to each tabled value of molecular absorption coefficient, based upon AFCRL's "average continental aerosol model" (1974), to arrive at a total attenuation coefficient. Transmittances for the 5-km path were calculated from the resulting values of attenuation coefficient.

RESULTS

The results are graphed on Figure A-30. The first bar for each wavelength shows the NRL-measured transmittance, and the second bar (where given) shows the corresponding NRL-calculated transmittance, both derived from the NRL graph of attenuation coefficients. Then, where given, the two horizontal marks adjacent to the second bar give the SRL-calculated transmittances for the AFCRL mid-latitude summer model (upper mark) and AFCRL tropical model (lower mark).

Table A-19 summarizes the calculations and tabulated results supporting the graphical presentation.

COMMENTS ON RESULTS

Computed estimates of transmittance for the P-40 line are greatly in error in comparison to the measured value. A possible explanation may lie in the close proximity of a strong water vapor absorption line to the P40 frequency. (See Figure A-31, adapted from Ref. 4.) A small error in the estimated frequency of either line could result in near superposition of the two attenuation spikes shown at wave numbers of 925 and 925.4 per centimeter on Figure A-31, and could account for a much greater attenuation of the P40 line than is accounted for by the available (AFCRL-computed) attenuation coefficients.

It also appears, from Figure A-30, that the SRL-calculated "bounds" (based upon the AFCRL tropical and mid-latitude summer models) are somewhat optimistic for the P28 line, somewhat pessimistic for the P10, P14, and P18 lines, and "about right" for the remaining lines for which attenuation coefficients were available.

The following observations are made comparing these results and comparable results for a group of DF laser wavelengths in the neighborhood of 3.8 micrometer, reported in Section A-7 of this appendix.

1. The "limiting" transmittance (i.e., the envelope of peak transmittance values over the wavelength region of interest) is much lower in the CO_2 laser wavelength region than it is in the DF laser wavelength region, mainly because of the much higher water vapor continuum absorption in the CO_2 wavelength region.

2. CO_2 laser wavelengths are at CO_2 absorption line frequencies (see Figure A-31); hence the transmittance of most CO_2 laser lines is poorer than the average "band transmittance" for the adjoining wavelength region.

3. The wavelengths of DF laser lines having "good" or better atmospheric transmittance do not coincide with atmospheric absorption lines; hence the transmittance of such lines is better than the average "band transmittance" for the adjoining wavelength region.

4. The following brief summary of NRL measured transmittances for the 5-kilometer overwater path at Cape Canaveral shows one comparison of DF laser and CO_2 laser atmospheric transmittances, for roughly comparable atmospheric conditions:

a. For all 22 DF lines employed, measured transmittances fell between 0.41 and 0.79. Twenty were above 0.6

b. For all 16 CO_2 lines employed, measured transmittances fell between 0.0002 and 0.25. The 10.591 micrometer value was 0.11 and 11 of 13 lines between 10.2 micrometer and 10.9 micrometer were between 0.095 and 0.15.

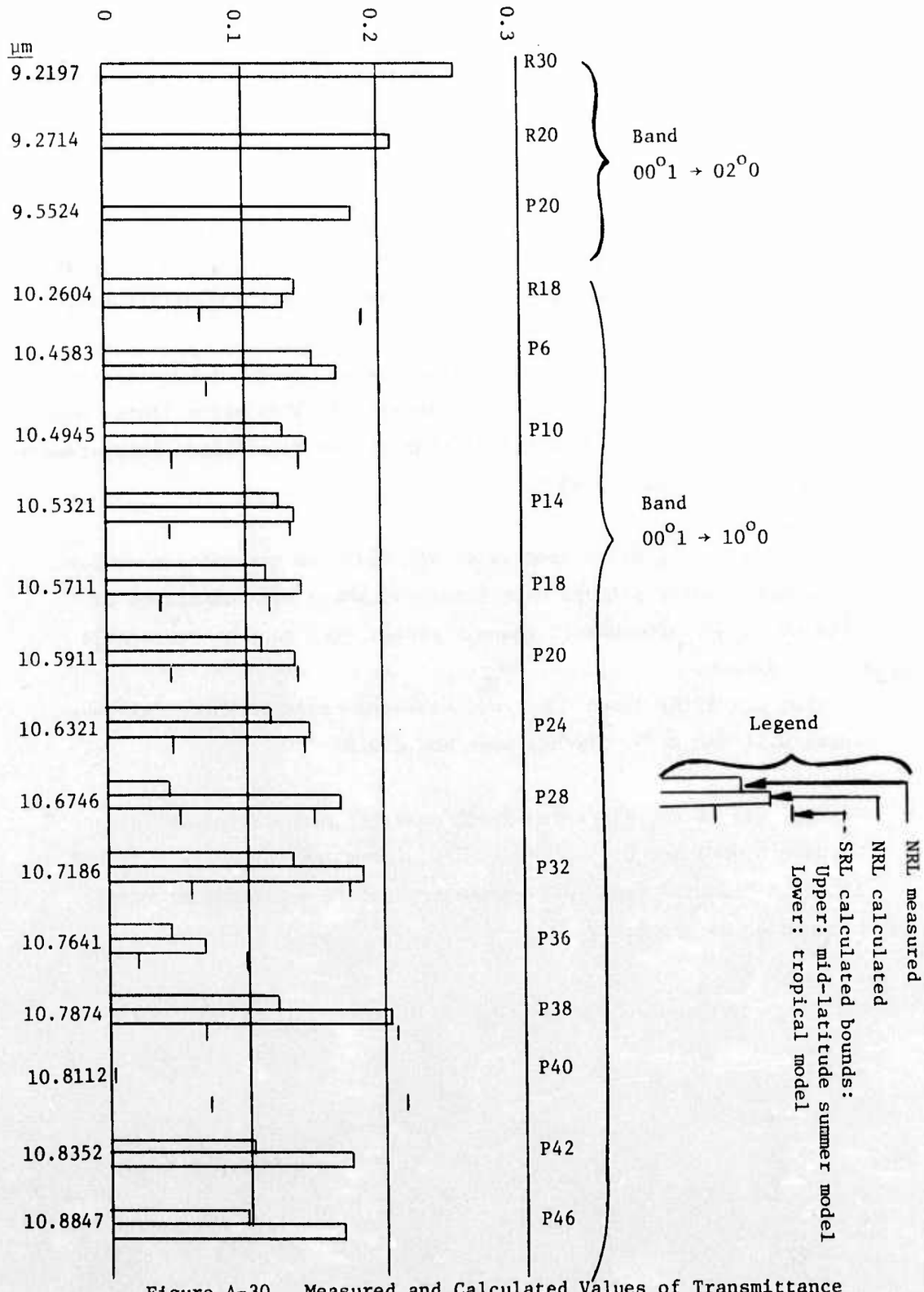

Figure A-30. Measured and Calculated Values of Transmittance Over a 5-km Over-Water Path for a Group of CO_2 Laser Lines

Location of CO_2 laser lines added. Mid-latitude winter model (H_2O vapor = 0.35 gm/cm^2-km)

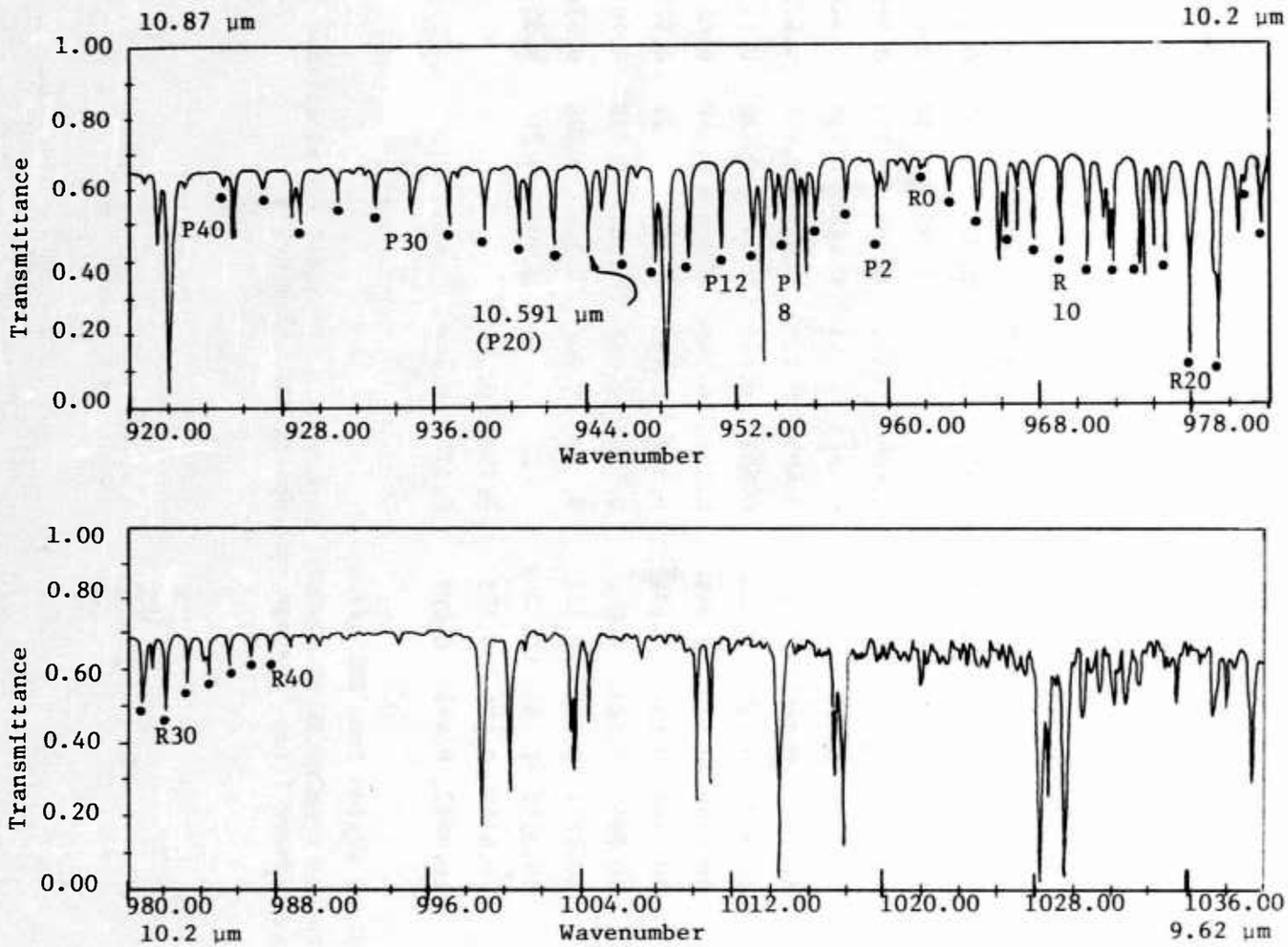

Figure A-31. Atmospheric Transmittance Due to Molecular Absorption Through a 10-km Horizontal Path at Sea Level

Table A-19. Measured and Calculated Values of Attenuation Coefficient and Transmittance over 5-km Over-Water Path, for a Group of CO_2 Laser Lines

CO_2 Laser Line	λ (μm)	Attenuation Coefficient, γ, and Transmittance, T							
		NRL Measured		NRL Calc'd		SRL Calc'd (Mid-lat summer)		SRL Calc'd (Tropical)	
		γ*	T	γ*	T	γ**	T	γ*	T
R30	9.2197	0.275	0.253						
R20	9.2714	0.315	0.207						
P20	9.5524	0.345	0.178						
R18	10.2604	0.395	0.139	0.410	0.129	0.338	0.185	0.535	0.069
P6	10.4583	0.380	0.150	0.358	0.167	0.323	0.199	0.526	0.072
P10	10.4945	0.410	0.129	0.386	0.145	0.393	0.140	0.609	0.048
P14	10.5321	0.417	0.124	0.400	0.135	0.404	0.133	0.620	0.045
P18	10.5711	0.432	0.115	0.392	0.141	0.428	0.118	0.648	0.039
P20	10.5911	0.440	0.111	0.400	0.135	0.398	0.137	0.622	0.045
P24	10.6321	0.430	0.116	0.385	0.146	0.395	0.139	0.616	0.046
P28	10.6746	0.640	0.041	0.355	0.169	0.380	0.150	0.601	0.050
P32	10.7186	0.402	0.134	0.340	0.183	0.350	0.174	0.570	0.058
P36	10.7641	0.625	0.044	0.538	0.068	0.464	0.098	0.787	0.020
P38	10.7874	0.420	0.122	0.320	0.202	0.316	0.206	0.534	0.069
P40	10.8112	>1.66	<0.0003			0.308	0.214	0.527	0.072
P42	10.8352	0.455	0.103	0.350	0.174				
P46	10.8847	0.463	0.099	0.357	0.168				

*: Values scaled from NRL graph.

**: Values from AFCRL-TR-72-0611, with γ_a = 0.013 added for normalized "clear" atmosphere (from "average continental aerosol model").

Section A-9

TRANSMITTANCE OF 0.6525 MICROMETER LASER BEAM OVER 66-KILOMETER SLANT PATH

In Section A-5 the following equivalent sea level path lengths (ESLP's) are determined for atmospheric aerosol partial transmittances:

1. Normalized "clear" atmosphere (sea level visibility = 23 km):
   ESLP, 0-1 km vertical, = 0.664 γ_a
   ESLP, 1-12 km vertical, = 0.656 γ_a
   } sum = 1.32 γ_a

2. Normalized "hazy" atmosphere (sea level visibility = 5 km):
   ESLP, 0-1 km vertical, = 0.604 $\gamma_{a(h)}$
   ESLP, 1-12 km vertical, = 0.373 $\gamma_{a(h)}$
   } sum = 0.977 $\gamma_{a(h)}$

   Also, γ_a (hazy) = 4.87 γ_a (clear).

The following values of γ_a at 0.6525 micrometer were determined by linear interpolation between tabled values for 0.63 micrometer and 0.69 micrometer, from data supplied by AFCRL for their "average continental aerosol model" (1974) and "estimated average marine aerosol model" (1975) in private communications of 3 March 1975 (Ref. 19) and 25 March 1975 (Ref.20), respectively:

γ_a (continental, "clear") = 0.1415 per km
γ_a (marine, "clear") = 0.1471 per km
} sea level values

The "optical depth" (OD) of scattering due to atmospheric gases from 0 to 12 km altitude (vertical) was determined from Ref. 1, at 0.6328 micrometer and 0.6943 micrometer, for the tropical, mid-latitude summer, and mid-latitude winter atmospheric models. Interpolation to 0.6525 micrometer was accomplished using the λ^{-4} dependence of molecular scattering, with the following results:

OD, 0-12 km, tropical:	0.0390
OD, 0-12 km, mid-latitude summer:	0.0392
OD, 0-12 km, mid-latitude winter	0.0402

The foregoing values and relationships were used to develop Tables A-20 and A-21, and the results are graphed in Figure A-32.

Table A-20. Continental Aerosols

Latitude /Season Model	Aerosol Condition	$\Sigma h\sigma_m$ 0-12 km	$\Sigma h\gamma_a$ 0-12 km (= $b\gamma_a$)*	$\Sigma h\gamma_t$ 0-12 km	OD = $5.41\Sigma h\gamma_t$	T= e^{-OD}
T	Clear	0.0390	0.1868	0.2258	1.2216	0.295
MS		0.0392		0.2260	1.223	0.294
MW		0.0402		0.2270	1.228	0.293
T	Lt.Haze		0.3547#	0.3937	2.130	0.119
MS				0.3939	2.131	0.119
MW				0.3949	2.136	0.118
T	Hazy		0.6735	0.7125	3.855	0.021
MS				0.7127	3.856	0.021
MW				0.7137	3.861	0.021

*: b = 1.32 (clear), 4.76 (hazy).
#: Light haze $\Sigma h\gamma_a$ = geometric mean of clear and hazy values.

Table A-21. Composite Marine Aerosols

Latitude /Season Model	Aerosol Condition	$\Sigma h\sigma_m$ 0-12 km	$\Sigma h\gamma_a$** 0-1 km (marine)	$\Sigma h\gamma_a$** 1-12 km (continental)	$\Sigma h\gamma_t$ 0-12 km	OD = $5.41\Sigma h\gamma_t$	T= e^{-OD}
T	Clear	0.0390	0.0977	0.0928	0.2295	1.2416	0.289
MS		0.0392			0.2297	1.2427	0.289
MW		0.0402			0.2307	1.2481	0.287
T	Lt.Haze		0.2056	0.1544	0.3990	2.1586	0.115
MS					0.3992	2.1597	0.115
MW					0.4002	2.1651	0.115
T	Hazy		0.4327	0.2570	0.7287	3.9423	0.019
MS					0.7289	3.9433	0.019
MW					0.7299	3.9488	0.019

**: See text for conversion factors and sea level coefficients.

Clear: sea level visibility = 23 km
Light haze: sea level visibility = 10.8 km
Hazy: sea level visibility = 5 km
W = mid-latitude winter model
S = mid-latitude summer model
T = tropical model

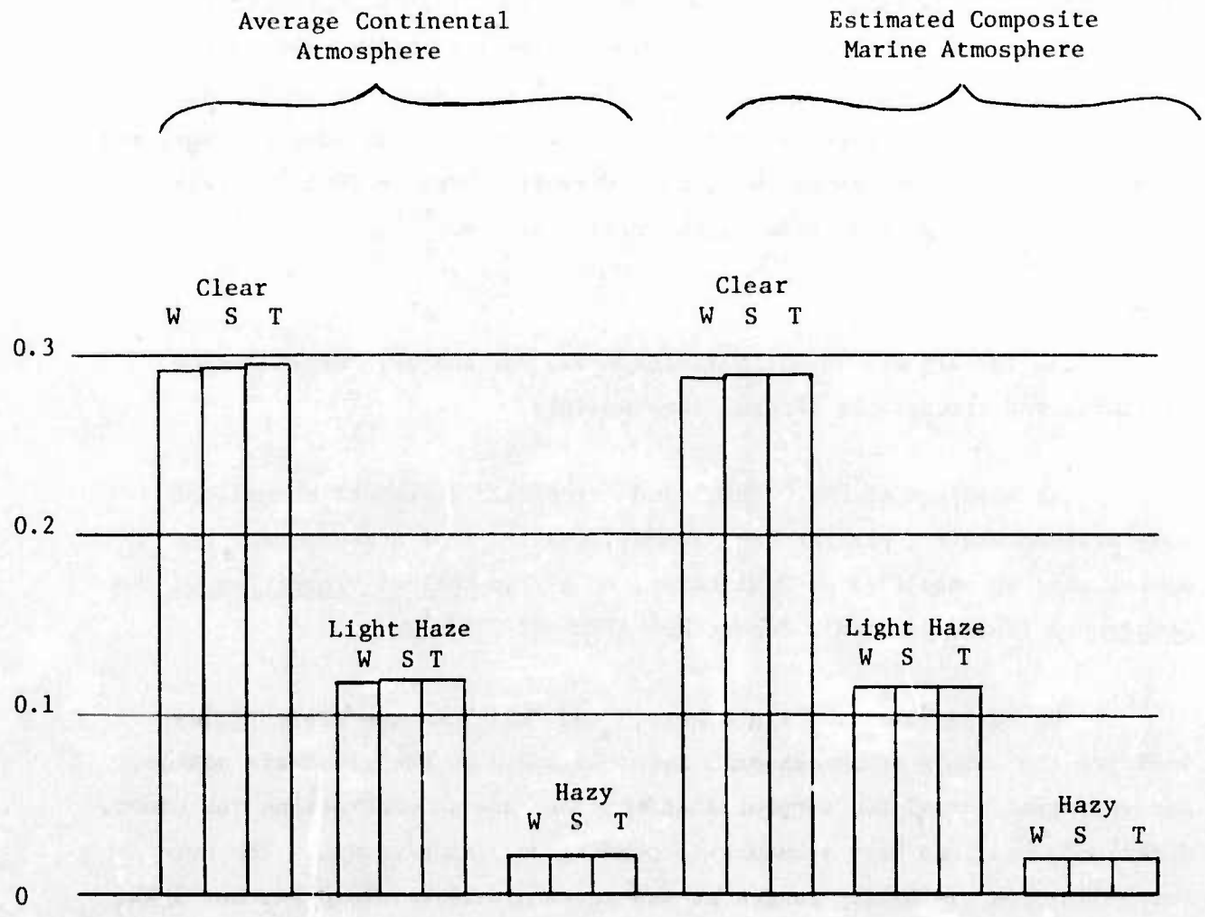

Figure A-32. Calculated Transmittance of 0.6525 μm Laser Over 66-Kilometer Slant Path

Section A-10

CALCULATED 66-KILOMETER SLANT PATH TRANSMITTANCES FOR 36 DF LASER LINES

INTRODUCTION

The atmospheric transmittance of a 66-kilometer slant path was calculated for 36 DF laser lines covering the frequency range from 2419.070 waves per centimeter to 2862.653 waves per centimeter. The corresponding wavelength range is from 3.493263 micrometers to 4.133820 micrometers. The specified slant path of interest is from sea level to 40,000 feet altitude, with a horizontal range of 35 nautical miles. Corresponding metric distances are 0 to 12.192 kilometers altitude, 64.82 kilometers horizontal range, and 65.96 kilometers slant range, with path elevation angle = 10.65^{o}. (All calculations were accomplished in the metric system.)

RESULTS

The results are shown in Tables A-22, 23, and 24, for 18 season, latitude, and atmospheric aerosol combinations.

The headings of "MW," "MS," and "tropical" represent normalized mid-latitude winter, mid-latitude summer, and tropical atmospheres, respectively, as specified by McClatchey, et al, in Optical Properties of the Atmosphere (Third Edition), Report No. AFCRL-72-0497 (Ref. 1).

The terms "clear," "light haze," and "hazy" in the table titles indicate the levels of atmospheric aerosols added to the clean air models, and represent normalized aerosol distributions and concentrations for clear, moderately hazy and hazy atmospheric conditions, respectively. The corresponding eye visibility ranges at sea level are 23 km, 10.8 km, and 5 km, respectively.

The headings of "continental aerosols" and "composite marine aerosols" indicate the source of the aerosol constituents. The composite marine

aerosol model incorporates a high concentration of sea spray in the first kilometer above sea level.

CALCULATION METHOD

1. Revised laser line frequencies were employed, per advance unpublished data (Ref. 16) received from Dr. Ron Long, OSU Electro-Science Laboratory on 8 August 1975. The stated accuracy of these revised frequencies is $\pm$ 0.003 waves per centimeter.

2. Revised tables of molecular absorption coefficients by altitude layers (for the OSU line frequencies) were used, per advance unpublished data (Ref. 41) received from AFCRL on 11 September 1975. Computer calculation of these tables was accomplished by AFCRL upon request of SRL via our letter of 11 August 1975 to Dr. John Selby, Optical Physics Laboratory of AFCRL.

3. Revised tables of aerosol absorption and scattering coefficients for an "average continental aerosom model" were employed, per unpublished data (Ref. 19) received from Dr. Selby by letter of 3 March 1975. SRL derived vertical "optical depth" values (for our nominal slant path) from these revised sea level tables per techniques deduced from AFCRL-72-0497 (Ref. 1).

4. Tables of estimated aerosol absorption and scattering coefficients for an "estimated marine aerosol model" were employed, per advance unpublished data (Ref. 20) received from Dr. Selby by letter of 25 March 1975. Again, SRL derived vertical optical depth values from these tables. The "estimated marine aerosol model" is composed of 60% sea spray and 40% continental aerosols.

5. SRL's "composite" marine atmosphere assumes that the AFCRL "estimated marine aerosol model" (60% sea spray) exists from sea level to one kilometer altitude, and continental aerosols exist above one

kilometer. Both are appropriately tapered with altitude, using factors derived from AFCRL-72-0497 (Ref. 1).

6. Values for H_2O continuum absorption (omitted from the AFCRL tables) were taken from revised OSU advance unpublished data (Ref. 15) attributed to Burch. These sea level values were converted to optical depth values for vertical paths by SRL, using the methods and data of AFCRL-72-0497 (Ref. 1).

7. The vertical optical depth (OD) values (0-12 km), computed for each class of contributor, were summed to determine a total vertical OD. The path OD was then taken as 5.41 times the total vertical OD, since sec (90^o - 10.65^o) is 5.41.

NOTE:

The AFCRL marine atmosphere aerosol model and the assumptions of SRL's composite aerosol model are estimates based upon the limitations of currently available data. An extensive at-sea measurements program would be needed to improve these estimates significantly.

Table A-22. Calculated 66-Kilometer Slant Path Transmittances for 36 DF Laser Lines, Clear Atmosphere

Line ID	Frequency (cm^{-1})	Continental Aerosols			Composite Marine Aerosols		
		MW	MS	Tropical	MW	MS	Tropical
3-2 P(13)	2419.070	0.173	0.132	0.109	0.143	0.109	0.090
3-2 P(12)	2445.356	0.223	0.172	0.145	0.184	0.142	0.120
3-2 P(11)	2471.245	0.321	0.257	0.218	0.265	0.212	0.180
3-2 P(10)	2496.721	0.507	0.429	0.377	0.417	0.353	0.310
2-1 P(13)	2500.428	0.531	0.453	0.400	0.437	0.373	0.329
3-2 P(9)	2521.769	0.638	0.556	0.497	0.525	0.457	0.409
2-1 P(12)	2527.391	0.656	0.574	0.515	0.539	0.472	0.423
3-2 P(8)	2546.375	0.448	0.404	0.365	0.368	0.332	0.300
2-1 P(11)	2553.953	0.625	0.563	0.510	0.513	0.462	0.419
3-2 P(7)	2570.522	0.184	0.180	0.165	0.151	0.148	0.135
2-1 P(10)	2580.097	0.154	0.142	0.130	0.126	0.116	0.106
1-0 P(13)	2583.486	0.511	0.448	0.403	0.419	0.367	0.330
3-2 P(6)	2594.198	0.768	0.658	0.584	0.629	0.539	0.478
2-1 P(9)	2605.807	0.772	0.616	0.524	0.631	0.504	0.429
1-0 P(12)	2611.142	0.807	0.699	0.623	0.660	0.571	0.509
3-2 P(5)	2617.386	0.816	0.726	0.657	0.667	0.593	0.537
2-1 P(8)	2631.068	0.752	0.601	0.509	0.614	0.491	0.415
1-0 P(11)	2638.392	0.403	0.067	0.023	0.329	0.055	0.019
3-2 P(4)	2640.074	0.761	0.549	0.438	0.621	0.448	0.358
2-1 P(7)	2655.863	0.669	0.371	0.255	0.546	0.302	0.208
3-2 P(3)	2662.246	0.793	0.625	0.525	0.647	0.509	0.428
1-0 P(10)	2665.219	0.760	0.614	0.523	0.619	0.500	0.427
2-1 P(6)	2680.179	0.747	0.521	0.407	0.608	0.424	0.332
3-2 P(2)	2683.890	0.821	0.709	0.625	0.668	0.577	0.509
1-0 P(9)	2691.607						
2-1 P(5)	2703.999	0.827	0.698	0.605	0.612	0.567	0.492
1-0 P(8)	2717.539	0.675	0.328	0.205	0.548	0.266	0.167
2-1 P(4)	2727.309	0.771	0.541	0.419	0.625	0.439	0.340
1-0 P(7)	2742.998	0.741	0.498	0.309	0.601	0.403	0.250
2-1 P(3)	2750.094	0.781	0.617	0.511	0.633	0.500	0.414
1-0 P(6)	2767.968	0.517	0.323	0.231	0.419	0.261	0.187
2-1 P(2)	2772.340	0.0563	0.00016	<.00001	0.046	0.00013	<.00001
1-0 P(5)	2792.434	0.728	0.479	0.352	0.588	0.387	0.284
1-0 P(4)	2816.380	0.607	0.311	0.194	0.489	0.250	0.156
1-0 P(3)	2839.791	0.742	0.445	0.305	0.596	0.358	0.245
1-0 P(2)	2862.653	0.715	0.407	0.268	0.574	0.326	0.215

Note: Calculated values are omitted for the 1-0 P(9) line because an erroneous frequency value was employed by AFCRL in the computer calculation of coefficients for this line, making the results meaningless. Dr. Selby reported (Ref.43) (Ref. 43) that he is checking H_2O line strengths throughout this spectral region and will supply a complete set of new tables eventually, in lieu of re-running 1-0 P(9).

Table A-23. Calculated 66-Kilometer Slant Path Transmittances for 36 DF Laser Lines, Light Haze Atmosphere

Line ID	Frequency (cm^{-1})	Continental Aerosols			Composite Marine Aerosols		
		MW	MS	Tropical	MW	MS	Tropical
3-2 P(13)	2419.070	0.154	0.118	0.097	0.104	0.079	0.065
3-2 P(12)	2445.356	0.199	0.153	0.130	0.133	0.102	0.087
3-2 P(11)	2471.245	0.286	0.229	0.194	0.191	0.153	0.130
3-2 P(10)	2496.721	0.451	0.382	0.335	0.300	0.254	0.223
2-1 P(13)	2500.428	0.472	0.403	0.356	0.314	0.268	0.236
3-2 P(9)	2521.769	0.567	0.494	0.442	0.376	0.328	0.293
2-1 P(12)	2527.391	0.583	0.510	0.457	0.386	0.338	0.303
3-2 P(8)	2546.375	0.398	0.358	0.324	0.263	0.237	0.214
2-1 P(11)	2553.953	0.555	0.500	0.453	0.366	0.330	0.299
3-2 P(7)	2570.522	0.163	0.160	0.146	0.108	0.105	0.096
2-1 P(10)	2580.097	0.137	0.126	0.115	0.090	0.083	0.076
1-0 P(13)	2583.486	0.453	0.397	0.357	0.298	0.261	0.235
3-2 P(6)	2594.198	0.680	0.583	0.517	0.447	0.383	0.340
2-1 P(9)	2605.807	0.683	0.545	0.464	0.448	0.358	0.304
1-0 P(12)	2611.142	0.714	0.618	0.551	0.468	0.405	0.361
3-2 P(5)	2617.386	0.722	0.642	0.581	0.473	0.420	0.380
2-1 P(8)	2631.068	0.665	0.532	0.450	0.434	0.347	0.294
1-0 P(11)	2638.392	0.357	0.060	0.020	0.232	0.039	0.013
3-2 P(4)	2640.074	0.672	0.485	0.387	0.439	0.316	0.253
2-1 P(7)	2655.863	0.591	0.327	0.225	0.385	0.213	0.147
3-2 P(3)	2662.246	0.700	0.551	0.463	0.456	0.359	0.302
1-0 P(10)	2665.219	0.670	0.542	0.462	0.436	0.352	0.300
2-1 P(6)	2680.179	0.658	0.459	0.359	0.427	0.298	0.233
3-2 P(2)	2683.890	0.723	0.625	0.551	0.469	0.405	0.358
1-0 P(9)	2691.607						
2-1 P(5)	2703.999	0.728	0.615	0.533	0.471	0.398	0.345
1-0 P(8)	2717.539	0.594	0.289	0.181	0.383	0.186	0.117
2-1 P(4)	2727.309	0.680	0.476	0.369	0.437	0.307	0.238
1-0 P(7)	2742.998	0.652	0.437	0.272	0.419	0.281	0.175
2-1 P(3)	2750.094	0.686	0.542	0.449	0.441	0.348	0.289
1-0 P(6)	2767.968	0.454	0.284	0.203	0.291	0.182	0.130
2-1 P(2)	2772.340	0.049	0.00014	<.00001	0.032	0.00009	<.00001
1-0 P(5)	2792.434	0.639	0.420	0.309	0.407	0.268	0.197
1-0 P(4)	2816.380	0.512	0.272	0.170	0.338	0.173	0.108
1-0 P(3)	2839.791	0.648	0.389	0.267	0.410	0.246	0.169
1-0 P(2)	2862.653	0.625	0.356	0.234	0.393	0.223	0.147

See Note for Table A-22.

Table A-24. Calculated 66-Kilometer Slant Path Transmittances for 36 DF Laser Lines, Hazy Atmosphere

Line ID	Frequency (cm^{-1})	Continental Aerosols			Composite Marine Aerosols		
		MW	MS	Tropical	MW	MS	Tropical
3-2 P(13)	2419.070	0.125	0.095	0.078	0.054	0.041	0.034
3-2 P(12)	2445.356	0.160	0.124	0.105	0.069	0.053	0.045
3-2 P(11)	2471.245	0.230	0.184	0.156	0.098	0.078	0.067
3-2 P(10)	2496.721	0.362	0.306	0.269	0.153	0.130	0.114
2-1 P(13)	2500.428	0.379	0.323	0.285	0.160	0.137	0.121
3-2 P(9)	2521.769	0.454	0.396	0.353	0.191	0.166	0.149
2-1 P(12)	2527.391	0.466	0.408	0.366	0.196	0.171	0.154
3-2 P(8)	2546.375	0.317	0.286	0.259	0.133	0.119	0.108
2-1 P(11)	2553.953	0.442	0.398	0.361	0.184	0.166	0.150
3-2 P(7)	2570.522	0.130	0.127	0.116	0.054	0.053	0.048
2-1 P(10)	2580.097	0.109	0.100	0.091	0.045	0.042	0.038
1-0 P(13)	2583.486	0.360	0.315	0.284	0.149	0.130	0.118
3-2 P(6)	2594.198	0.541	0.463	0.411	0.223	0.191	0.169
2-1 P(9)	2605.807	0.542	0.433	0.368	0.223	0.178	0.151
1-0 P(12)	2611.142	0.566	0.490	0.437	0.232	0.201	0.179
3-2 P(5)	2617.386	0.572	0.509	0.460	0.234	0.208	0.189
2-1 P(8)	2631.068	0.527	0.421	0.356	0.215	0.172	0.145
1-0 P(11)	2638.392	0.282	0.047	0.016	0.115	0.019	0.007
3-2 P(4)	2640.074	0.532	0.383	0.306	0.217	0.156	0.125
2-1 P(7)	2655.863	0.467	0.259	0.178	0.189	0.105	0.072
3-2 P(3)	2662.246	0.553	0.435	0.366	0.233	0.178	0.148
1-0 P(10)	2665.219	0.529	0.427	0.365	0.214	0.173	0.147
2-1 P(6)	2680.179	0.519	0.362	0.282	0.209	0.146	0.115
3-2 P(2)	2683.890	0.570	0.492	0.434	0.229	0.198	0.174
1-0 P(9)	2691.607						
2-1 P(5)	2703.999	0.572	0.483	0.419	0.228	0.193	0.167
1-0 P(8)	2717.539	0.466	0.227	0.142	0.185	0.090	0.056
2-1 P(4)	2727.309	0.532	0.373	0.289	0.211	0.148	0.115
1-0 P(7)	2742.998	0.511	0.344	0.213	0.201	0.135	0.084
2-1 P(3)	2750.094	0.537	0.425	0.352	0.211	0.167	0.138
1-0 P(6)	2767.968	0.355	0.222	0.158	0.139	0.087	0.062
2-1 P(2)	2772.340	0.039	0.00011	<.00001	0.015	<.00001	<.00001
1-0 P(5)	2792.434	0.498	0.327	0.241	0.193	0.127	0.093
1-0 P(4)	2816.380	0.414	0.212	0.132	0.159	0.081	0.051
1-0 P(3)	2839.791	0.503	0.302	0.207	0.191	0.115	0.079
1-0 P(2)	2862.653	0.484	0.275	0.181	0.182	0.103	0.068

See Note for Table A-22.

Section A-11

CALCULATED AVERAGE TRANSMITTANCE OF A 500-WATT DF LASER OVER 66-KILOMETER SLANT PATH

The attached Tables A-25, 26, 27 and 28, and Figure A-33 show the results of calculations of the transmittance of the output beam of the 500-watt HAC/AFAL laser. The power distribution of that laser was obtained from a data sheet (Ref. 44) supplied by Dr. Ron Paulson, AFAL.

Revised laser line frequencies were employed, per advance unpublished data (Ref. 16) received from Dr. Ron Long, OSU Electro-Science Laboratory on 8 August 1975.

Revised tables of molecular absorption coefficients versus altitude (for the OSU line frequencies) were used, per advance unpublished data (Ref. 41) received from AFCRL on 11 September 1975.

Revised tables of aerosol absorption and scattering coefficients for an "average continental aerosol model" were employed, per unpublished data (Ref. 19) received from Dr. Selby by letter of 3 March 1975. SRL derived vertical "optical depth" values (for our nominal slant path) from these revised tables per techniques deduced from AFCRL-72-0497 (Ref. 1).

Tables of estimated aerosol absorption and scattering coefficients for an "estimated marine aerosol model" were employed, per advance unpublished data (Ref. 20) received from Dr. Selby by letter of 25 March 1975. Again, vertical optical depth values were derived from these tables. The "estimated marine aerosol model" is composed of 60% sea spray and 40% continental aerosols.

SRL's "composite" marine atmosphere assumes that the AFCRL "estimated marine aerosol model" (60% sea spray) exists from sea level to one kilometer altitude, and continental aerosols exist above one kilometer. Both are appropriately tapered with altitude, using factors derived from AFCRL-72-0497 (Ref. 1).

"Clear" and "hazy" on the tables and graph refer to a normalized clear atmosphere (visibility = 23 kilometers) and normalized hazy atmosphere (visibility = 5 kilometers), respectively, at sea level. "W" and "MW" represent McClatchey's mid-latitude winter atmosphere model, "S" and "MS" represent the mid-latitude summer model, and "T" represents the tropical model, all per AFCRL-72-0497 (Ref. 1).

The "average" or "total" transmittance values calculated are weighted averages: the calculated total transmittance at each laser line frequency is weighted by the transmitted power percentage at that line. Hence the resulting values represent the fraction of the total transmitted power surviving at the end of the path.

A word of caution: The AFCRL marine atmosphere aerosol model and the assumptions of SRL's composite aerosol model are estimates based upon the limitations of currently available data. An extensive at-sea measurements program would be needed to improve these estimates significantly.

Table A-25. Average Transmittance Calculation for 500-Watt DF Laser over 66-Kilometer Slant Path: Clear Atmosphere, Continental Aerosols

Line Id	%* P_T	Model Atmosphere: MW - Clear T	MW - Clear % P_R*	MS - Clear T	MS - Clear % P_R*	T - Clear T	T - Clear % P_R*
1-0 P(4)	0.3	0.607	0.18	0.311	0.09	0.194	0.06
1-0 P(5)	8.38	0.728	6.10	0.479	4.01	0.352	2.95
1-0 P(6)	9.68	0.517	5.00	0.323	3.13	0.231	2.24
1-0 P(7)	8.58	0.741	6.36	0.498	4.27	0.309	2.65
2-1 P(4)	0.70	0.771	0.54	0.541	0.38	0.419	0.29
1-0 P(8)	3.99	0.675	2.69	0.328	1.31	0.205	0.82
2-1 P(5)	8.68	0.827	7.18	0.698	6.06	0.605	5.25
2-1 P(6)	9.98	0.747	7.46	0.521	5.20	0.407	4.06
2-1 P(7)	9.48	0.669	6.34	0.371	3.52	0.255	2.42
2-1 P(8)	8.68	0.752	6.53	0.601	5.22	0.509	4.42
3-2 P(5)	8.08	0.816	6.59	0.726	5.87	0.657	5.31
2-1 P(9)	1.0	0.772	0.77	0.616	0.62	0.524	0.52
3-2 P(6)	9.08	0.768	6.97	0.658	5.97	0.584	5.30
3-2 P(7)	8.48	0.184	1.56	0.180	1.53	0.165	1.40
3-2 P(8)	4.69	0.448	2.10	0.404	1.89	0.365	1.71
3-2 P(9)	0.2	0.638	0.13	0.556	0.11	0.497	0.10
Totals:	100.0%		66.5%		49.2%		39.5%

*: P_T and P_R expressed as % of total power transmitted. P_T is transmitted power; P_R is beam power at end of path.

Table A-26. Average Transmittance Calculation for 500-Watt DF Laser over 66-Kilometer Slant Path: Hazy Atmosphere, Continental Aerosols

Line Id	%* P_T	Model Atmosphere: MW - Hazy T	MW - Hazy % P_R*	MS - Hazy T	MS - Hazy % P_R*	T - Hazy T	T - Hazy % P_R*
1-0 P(4)	0.3	0.414	0.12	0.212	0.06	0.132	0.04
1-0 P(5)	8.38	0.498	4.17	0.327	2.74	0.241	2.02
1-0 P(6)	9.68	0.355	3.44	0.222	2.15	0.158	1.53
1-0 P(7)	8.58	0.511	4.38	0.344	2.95	0.213	1.83
2-1 P(4)	0.70	0.532	0.37	0.373	0.26	0.289	0.20
1-0 P(8)	3.99	0.466	1.86	0.227	0.91	0.142	0.57
2-1 P(5)	8.68	0.572	4.96	0.483	4.19	0.419	3.64
2-1 P(6)	9.98	0.519	5.18	0.362	3.61	0.283	2.82
2-1 P(7)	9.48	0.467	4.43	0.259	2.46	0.178	1.69
2-1 P(8)	8.68	0.527	4.57	0.421	3.65	0.356	3.09
3-2 P(5)	8.08	0.572	4.62	0.509	4.11	0.460	3.72
2-1 P(9)	1.0	0.542	0.54	0.433	0.43	0.368	0.37
3-2 P(6)	9.08	0.541	4.91	0.463	4.20	0.411	3.73
3-2 P(7)	8.48	0.130	1.10	0.127	1.08	0.116	0.98
3-2 P(8)	4.69	0.317	1.49	0.286	1.34	0.259	1.21
3-2 P(9)	0.2	0.454	0.09	0.396	0.08	0.353	0.07
Totals:	100.0%		46.3%		34.2%		27.5%

*: P_T and P_R expressed as % of total power transmitted. P_T is transmitted power; P_R is beam power at end of path.

Table A-27. Average Transmittance Calculation for 500-Watt DF Laser over 66-Kilometer Slant Path: Clear Atmosphere, Composite Aerosols

Line Id	%* P	Model Atmosphere: MW - Clear T	MW - Clear % P_R*	MS - Clear T	MS - Clear % P_R*	T - Clear T	T - Clear % P_R*
1-0 P(4)	0.3	0.489	0.15	0.250	0.08	0.156	0.05
1-0 P(5)	8.38	0.588	4.93	0.387	3.24	0.284	2.38
1-0 P(6)	9.68	0.419	4.06	0.261	2.53	0.187	1.81
1-0 P(7)	8.58	0.601	5.16	0.403	3.46	0.250	2.15
2-1 P(4)	0.70	0.625	0.44	0.439	0.31	0.340	0.24
1-0 P(8)	3.99	0.548	2.19	0.266	1.06	0.167	0.67
2-1 P(5)	8.68	0.612	5.31	0.567	4.92	0.492	4.27
2-1 P(6)	9.98	0.608	6.07	0.424	4.23	0.332	3.31
2-1 P(7)	9.48	0.546	5.18	0.302	2.86	0.208	1.97
2-1 P(8)	8.68	0.614	5.33	0.491	4.26	0.415	3.60
3-2 P(5)	8.08	0.667	5.39	0.593	4.79	0.537	4.34
2-1 P(9)	1.0	0.631	0.63	0.504	0.50	0.429	0.43
3-2 P(6)	9.08	0.629	5.71	0.539	4.89	0.478	4.34
3-2 P(7)	8.48	0.151	1.28	0.148	1.26	0.135	1.14
3-2 P(8)	4.69	0.368	1.73	0.332	1.56	0.300	1.40
3-2 P(9)	0.2	0.525	0.11	0.457	0.09	0.409	0.08
Totals:	100.0%		53.6%		40.0%		32.1%

*: P_T and P_R expressed as % of total power transmitted. P_T is transmitted power; P_R is beam power at end of path.

Table A-28. Average Transmittance Calculation for 500-Watt DF Laser over 66-Kilometer Slant Path: Hazy Atmosphere, Composite Aerosols

Line ID	%* P_T	Model Atmosphere: MW - Hazy T	MW - Hazy % P_R*	MS - Hazy T	MS - Hazy % P_R*	T - Hazy T	T - Hazy % P_R*
1-0 P(4)	0.3	0.159	0.05	0.081	0.02	0.051	0.02
1-0 P(5)	8.38	0.193	1.62	0.127	1.06	0.093	0.78
1-0 P(6)	9.68	0.139	1.35	0.087	0.84	0.062	0.60
1-0 P(7)	8.58	0.201	1.72	0.220	1.89	0.084	0.070
2-1 P(4)	0.70	0.211	0.15	0.148	0.10	0.115	0.08
1-0 P(8)	3.99	0.185	0.74	0.090	0.36	0.056	0.22
2-1 P(5)	8.68	0.228	1.98	0.193	1.68	0.167	1.45
2-1 P(6)	9.98	0.209	2.09	0.146	1.46	0.115	1.15
2-1 P(7)	9.48	0.189	1.79	0.105	1.00	0.072	0.68
2-1 P(8)	8.68	0.215	1.87	0.172	1.49	0.145	1.26
3-2 P(5)	8.08	0.234	1.89	0.208	1.68	0.189	1.53
2-1 P(9)	1.0	0.223	0.22	0.178	0.18	0.151	0.15
3-2 P(6)	9.08	0.223	2.02	0.191	1.73	0.169	1.53
3-2 P(7)	8.48	0.54	0.46	0.053	0.45	0.048	0.41
3-2 P(8)	4.69	0.133	0.62	0.119	0.56	0.108	0.51
3-2 P(9)	0.2	0.191	0.04	0.166	0.03	0.149	0.03
Totals:	100.0%		18.6%		14.5%		11.1%

*: P_T and P_R expressed as % of total power transmitted. P_T is transmitted power; P_R is beam power at end of path.

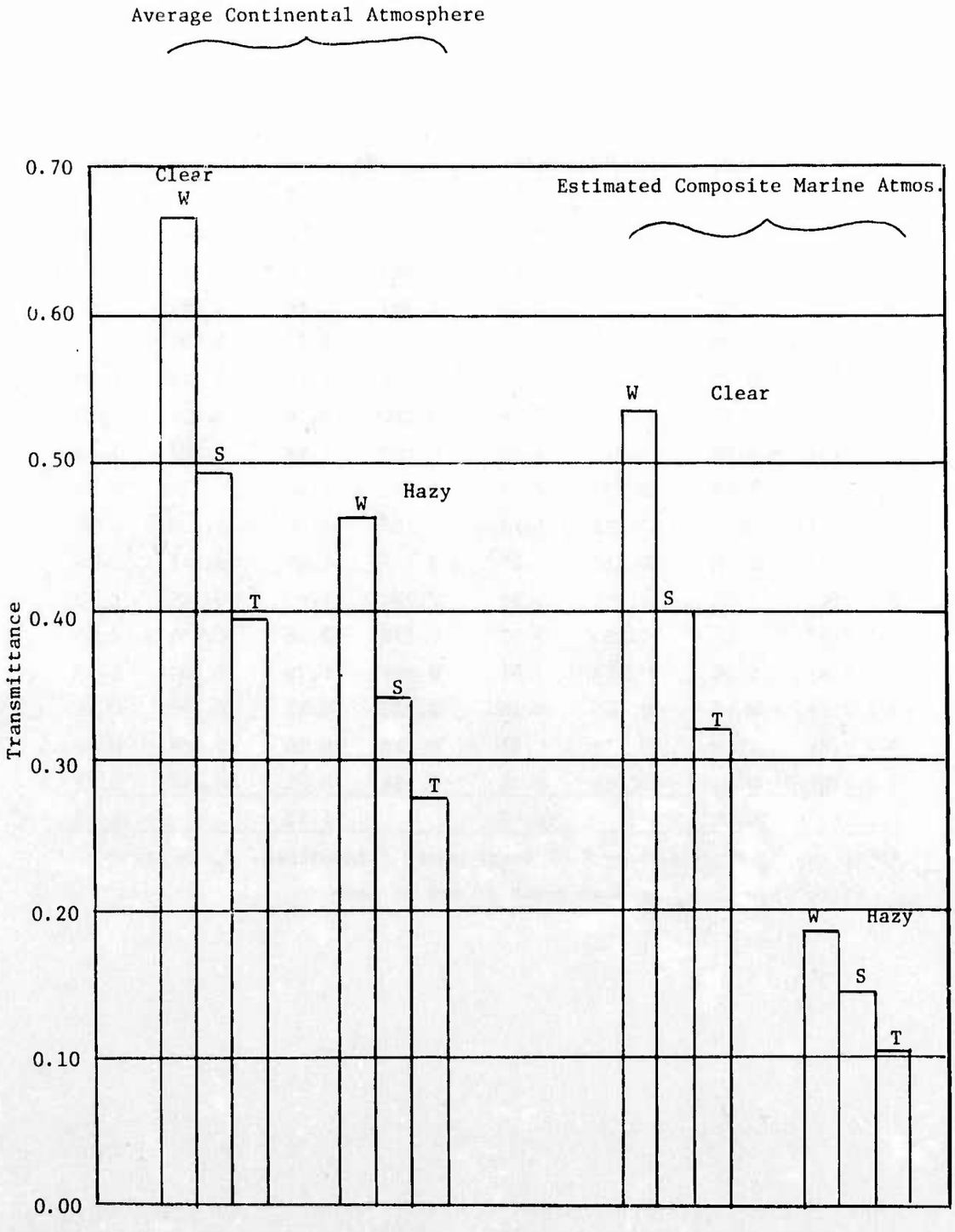

Figure A-33. Calculated Average Transmittance of 500 Watt DF Laser Over 66-Kilometer Slant Path

Section A-12

DF LASER LINE-SCANNER ATMOSPHERIC BACKSCATTER PRELIMINARY ANALYSIS

INTRODUCTION

A rigorous analytical treatment of the atmospheric backscatter problem for an active system is difficult. For a vertical or slant path the problem is compounded by variation in atmospheric scattering and attenuation coefficients with altitude.

Problem simplification, including introduction of a layer-by-layer evaluation and summation approach as employed in Section A-3 for path thermal radiance, offers a method for making engineering estimates. This section describes such a method and gives the results of a preliminary "quick look" analysis whose purpose was to determine whether atmospheric backscatter needs to be considered in design analysis for a DF laser line scanner.

APPROACH (see Figure A-34)

Divide the air-to-ground path into layers for which the average scattering coefficients and attenuation coefficients can be estimated. The most convenient layering is by one-kilometer altitude increments for which coefficient tables are available.

Then for layers other than the first (nearest the transmitter-receiver) the backscattered radiance of the layer is given approximately by the product of the incident power, the path length in the layer, and the normalized scattering phase function for 180^{o} (at the wavelength of interest), divided by the nominal beam area at the top of the layer. This radiance value is attenuated by the intervening atmospheric path between the layer and the receiver. That is, the backscattered radiance from the i^{th} layer is given approximately by

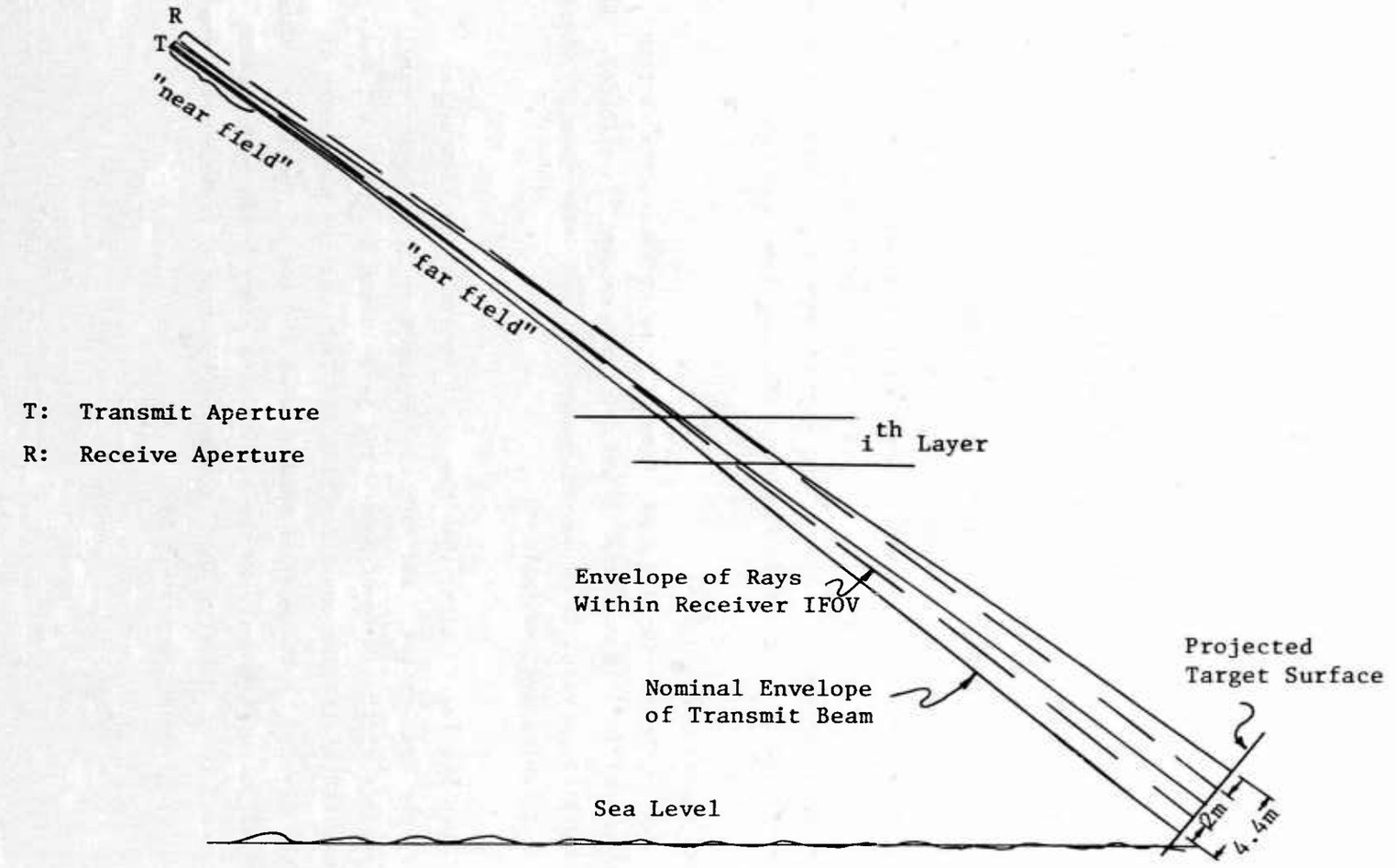

Figure A-34. Schematic Representation of Approximate Beam/IFOV Overlap

$$N_{s(\Delta r_i)} \simeq \frac{P\ (\Delta r_i)\ \sigma_i\ F_{(180^o)}}{\frac{\pi}{4}\ r^2\theta^2} \left[e^{-\Sigma\gamma_i(\Delta r_i)}\right]^2 \quad W/m^2\text{-ster.} \qquad (A\text{-}32)$$

where P is transmitted power, Δr_i is the path length in the i^{th} layer, σ_i and γ_i are the scattering and attenuation coefficients of the i^{th} layer, r is the total path length to the i^{th} layer, θ is the nominal beam diameter, and $F_{(180^o)}$ is the backscatter normalized scattering phase function. The exponential factor is squared, to account for two-way atmospheric attenuation.

Equation (A-32) becomes increasingly inaccurate for atmospheric layers close to the source, and fails completely at close ranges. Hence another approach was employed to approximate the atmospheric backscatter from the top atmospheric layer. The analytical basis for that approximation follows.

Assume, for the case of a CW laser illuminator, that separate receiving and transmitting apertures are employed (as would likely be necessary), separated by a small amount so that the receiver FOV and transmitter beam path do not intersect for at least the first few tens of meters, say to range R_1. Assume complete overlap beyond R_1, to the bottom of the layer, at range R_2. Then, in terms of the illustration below, the problem is to write an expression for the scattered power level $P_b dr$ from an elemental length of path dr (expressed in aperture irradiance terms), then integrate that expression between limits R_1 and R_2. The differential expression is (see following page)

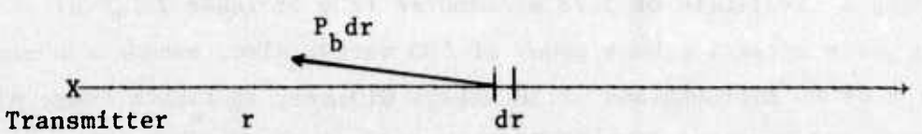

$$dH \simeq \frac{P_b dr}{r^2} \quad \text{watts/meter}^2 \text{ (of aperture)}$$

where $P_B = P\sigma_{(r)}F_{(180^o)}(e^{-\gamma r})^2$ = backscattered power per unit length of beam path

The scattering coefficient $\sigma_{(r)}$ may be assumed constant for the layer, and the attenuation negligible. Then Equation (A-32), with the simplified expression for P_b inserted, reduces to

$$dH \simeq P\sigma F_{(180^o)} \frac{dr}{r^2} \text{ watts/m}^2$$

Integrating, and inserting the cited limits

$$H = P\sigma F_{(180^o)} \left(\frac{1}{R_1} - \frac{1}{R_2} \right) \quad \text{watts/m}^2 \text{ of aperture,} \qquad \text{(A-33)}$$

where σ is in units of m^{-1} and R_1 and R_2 are in meters.

The above formula is undoubtedly pessimistic in that it assumes maximum overlap of the receiver IFOV and the transmit beam occurs abruptly rather than gradually. On the other hand, it ignores backscattered energy from port scattering and the beam sidelobes and/or skirts. Because transmitted energy from these sources can intersect the receiver IFOV very close to the apertures, it appears possible that these could be the strongest sources of backscattered irradiance of the receiving aperture.

EXAMPLE APPLICATION

Assumptions

Assume a wavelength of 3.73 micrometer (the DF laser 2-1 P(6) line) and a laser effective beam power of 500 watts. Also, assume a nominal beam diameter of 66 microradians (4.36 meters diameter at target range of 66 kilometers), and receiver IFOV of 30 microradians (1.98 meters diameter at target).

Example applicable coefficients, derived from AFCRL's "average continental aerosol model" and AFCRL-72-0497 (Ref. 1), are as follows:

	Continental Aerosols	Est. Marine Aerosols
σ_a (0 - 1 km, clear)	0.0120/km	0.049/km
σ_a (0 - 1 km, hazy)	0.0533	0.218
σ_a (11 - 12 km, clear or hazy)	0.000348	0.0014
σ_m (0 - 1 km)	4.8×10^{-6}	
σ_m (11 - 12 km)	1.47×10^{-6}	

Aerosol scattering: F (180^o, 3.73 micrometer) ≈ 0.014

Molecular scattering: F (180^o, 3.73 micrometer) = 0.12

It is clear from the above that molecular scattering is negligible compared to aerosol scattering, so it will be ignored in the following examples (for 66-km slant path.

Near Scattering (from top 1-km layer)

Assume R_1 = 100 meters, and marine aerosols, using Equation (A-33):

$$H \approx 500\,(0.0014 \times 10^{-3})(0.014)\left(\frac{1}{100} - \frac{1}{5410}\right)$$

$$= 9.8 \times 10^{-8} \text{ watts/meter}^2 \text{ (of aperture)}$$

This is about two orders of magnitude higher than the expected aperture irradiance from target reflected energy; hence it appears that backscatter from regions close to the source/receiver must be dealt with in system design.

Far Scattering [from bottom 1-km layer, for example, with marine aerosols and a "hazy" atmosphere, using Equation A-32)]:

$$N_s \simeq \frac{500(5.41)(0.218)(0.014)(0.5)^2}{\frac{\pi}{4}(4.4)^2}$$

$$= 0.136 \text{ watts/m}^2\text{-ster.}$$

This produces an aperture irradiance of

$$H \simeq \frac{0.136}{(60 \times 10^3)^2} = 3.8 \times 10^{-11} \text{ watts/m}^2$$

This value is somewhat smaller than expected signal irradiance of the aperture, but large enough to warrant consideration in detailed system analysis.

Intervening layers will contribute lesser amounts to the total backscattered irradiance of the receiver, and should be considered in a more detailed and comprehensive system analysis.

CONCLUSION

A preliminary conclusion to be drawn from this very sketchy analysis is that backscatter from regions near the transmitter/receiver is apt to be most troublesome to a CW active scanning system. However, the signal will be largely ac and the backscatter largely dc, and this is one factor that can be used to discriminate against the backscatter. (Atmospheric turbulence could alter this discriminant considerably.)

Projecting the analysis to a pulse system, it appears that range gating, to discard scattered energy from most of the path length, would be necessary or desirable. The ac/dc discrimination cited above is, of course, not applicable.

REFERENCES

1. R. A. McClatchey, R. W. Fenn, J. E. A. Selby, F. E. Volz, and J. S. Garing, Optical Properties of the Atmosphere (Third Edition), AFCRL-72-0497, 24 August 1972, Environmental Research Papers No. 411.

2. J. E. A. Selby and R. A. McClatchey, Atmoshperic Transmittance from 0.25 to 28.5 μm: Computer Code LOWTRAN 2, AFCRL-72-0745, 29 December 1972, Environmental Research Papers No. 427.

3. R. A. McClatchey and J. E. A. Selby, Atmospheric Attenuation of Laser Radiation from 0.76 to 31.25 μm, AFCRL-TR-74-0003, 3 January 1974, Environmental Research Papers No. 460.

4. R. A. McClatchey and J. E. A. Selby, Atmospheric Transmittance, 7-30 μm: Attenuation of CO_2 Laser Radiation, AFCRL-72-0611, 12 October 1972, Environmental Research Papers No. 419.

5. R. A. McClatchey, Atmospheric Attenuation of CO Laser Radiation, AFCRL-71-0370, 1 July 1971, Environmental Research Papers No. 359.

6. R. A. McClatchey, et al, AFCRL Atmospheric Absorption Line Parameters Compilation, AFCRL-TR-73-0096, 26 January 1973, Environmental Research Papers No. 434.

7. R. A. McClatchey and J. E. A. Selby, Atmospheric Attenuation of HF and DF Laser Radiation, AFCRL-72-0312, 23 May 1972, Environmental Research Papers No. 400.

8. J. E. A. Selby and R. A. McClatchey, Atmospheric Transmittance from 0.25 to 28.5 μm: Computer Code LOWTRAN 3, AFCRL-TR-75-0255, 7 May 1975, Environmental Research Papers No. 513.

9. R. K. Long, F. S. Mills, G. L. Trusty, Calculated Absorption Coefficients for DF Laser Frequencies, RADC-TR-73-389, November 1973.

10. J. H. McCoy, Atmospheric Absorption of Carbon Dioxide Laser Radiation Near 10 Microns, OSU Electro Science Laboratory Technical Report 2476-2, 10 September 1968.

11. C. C. Chen, A Correction for Middleton's Visible and Infrared Radiation Extinction Coefficients Due to Rain, Rand Corporation Report R-1523-PR, August 1974.

12. W. E. K. Middleton, Vision Through the Atmosphere, University of Toronto Press, 1952.

13. R. F. Lutomirski, R. E. Huschke, W. C. Meecham, and H. T. Yura, Degradation of Laser Systems by Atmospheric Turbulence, The Rand Corporation, R-1171-ARPHA/RC, June 1973.

14. V. I. Tatarski, The Effects of the Turbulent Atmosphere on Wave Propagation, translated from the Russian (originally published in 1967) (National Technical Information Service, Springfield, Virginia, 1971).

15. R. E. Meredith, D. R. Woods, F. G. Smith, and T. W. Tuer, High Resolution Spectral Survey of Molecular Absorption in the DF Laser Region: Measurements and Calculations, SAI-75-002-AA, May 1975. (Advance draft of proposed RADC TR)

16. R. Long, Electro Science Laboratory of OSU, private communication enclosing advance data on revised DF laser line frequency measurements and constituent absorption coefficient, 8 August 1975.

17. A. J. LaRocca, "Methods of Calculating Atmospheric Transmittance in the Infrared," Proceedings of the IEEE, January 1975.

18. A. R. Boileau, "Atmospheric Properties," Applied Optics Vol. 3, No. 5, May 1964, p. 570.

19. J. E. A. Selby, AFCRL, private communication on continental aerosol extinction and absorption coefficient, 3 March 1975.

20. J. E. A. Selby, AFCRL, private communication on maritime aerosol extinction and absorption coefficients, 25 March 1975.

21. R. S. Lawrence and J. W. Strohbehn, "A Survey of Clear-Air Propagation Effects Relevant to Optical Communications," Proceedings of the IEEE 58, 152 (1970).

22. C. A. Friehe and J. C. LaRue, Digest of Technical Papers from Topical Meeting on Optical Propagation Through Turbulence, University of Colorado (July 1974).

23. W. B. Johnson, W. E. Evans, and E. E. Uthe, Atmospheric Effects on Laser Eye Safety, Part I, Stanford Research Institute (April 1970).

24. G. E. Homstad, J. W. Strohbehn, R. H. Berger, and J. M. Heneghan, "Aperture-Averaging Effects for Weak Scintillations," JOSA 64, 162 (1974).

25. S. F. Clifford, G. R. Ochs, and R. S. Lawrence, "Saturation of Optical Scintillation by Strong Turbulence," JOSA 64, 148 (1974).

26. T. Chiba, "Spot Dancing of the Laser Beam Propagated Through the Turbulent Atmosphere," Appl. Opt. 10, 2456 (1971).

27. R. F. Lutomirski and H. T. Yura, "Imaging of Extended Objects Through a Turbulent Atmosphere," Appl. Opt. 13, 431 (1974).

28. Capt. Louis Pape, AFWL, private communication.

29. J. L. Blufton, "Measurement of Atmospheric Turbulence Strength at High Altitude with Balloon-Borne Temperature Sensors," Paper WA3, Digest of Technical Papers from Topical Meeting on Optical Propagation Through Turbulence, University of Colorado, July 1974.

30. G. L. Dryden, "Determination of C_n^2 Profiles via Point Source Aperture Averaged Scintillation," Paper WA4, Digest of Technical Papers from Topical Meeting on Optical Propagation Through Turbulence, University of Colorado, July 1974.

31. R. E. Hufnagel, "Variations of Atmospheric Turbulence," Paper WA1, Digest of Technical Papers from Topical Meeting on Optical Propagation Through Tur Turbulence, University of Colorado, July 1974.

32. A. W. Cooper, E. C. Crittenden, Jr., and A. F. Schroeder, "Height Dependence of Optical Scintillation over the Ocean," Paper WB4, Digest of Technical Papers from Topical Meeting on Optical Propagation Through Turbulence, University of Colorado, July 1974.

33. J. A. Dowling and P. M. Livingston, "Behavior of Focused Beams in Atmospheric Turbulence: Measurements and Comments on Theory," JOSA 63, 846 (1973).

34. R. E. Hufnagel, "A Theory for the Image-Degrading Effect of Turbulent Boundary Layers," Perkin-Elmer Engineering Report No. 7677, May 1964.

35. R. V. Shack, "The Effective Transfer Function of a Turbulent Boundary Layer," Perkin-Elmer Engineering Report No. 7673, May 1964.

36. Capt. James Negro, AFWL, private communication (enclosing SECRET data tabulation).

37. Maj. Keith Gilbert, AFWL, private communication.

38. Private discussions with R. W. Fenn, F. E. Volz, and E. P. Shettle regarding the status of atmospheric aerosol measurement, theory, and models. Visit to AFCRL, 28 April 1975.

39. R. E. Roberts, J. E. A. Selby, and L. M. Biberman, Infrared Continuum Absorption by Atmospheric Water Vapor in the 8-12 μm Window, AFCRL and IDA paper presented at IRIS St. Louis meeting on 3 February 1976.

40. J. A. Dowling, Appendix: Naval Research Laboratory Low Power DF Laser Propagation Measurements, advance draft obtained in a 16 July 1975 visit to NRL.

41. J. E. A. Selby, AFCRL, private communication enclosing tables of molecular absorption coefficients versus altitude for OSU-measured frequencies of 36 DF laser lines, 11 September 1975.

42. J. A. Dowling, graph of measured and calculated CO_2 laser line attenuation coefficients, obtained in 16 July 1975 visit to NRL.

43. J. E. A. Selby, AFCRL, private communication on LOWTRAN 3 revisions and DF laser line coefficients.

44. Private communication from R. Paulson, AFAL, "Table 2-27, Spectral Distribution of DF and HF Laser Output," July 1975.

BIBLIOGRAPHY

McCoy, J. H., D. B. Rensch, and R. K. Long, "Water Vapor Continuum Absorption of Carbon Dioxide Laser Radiation Near 10 μ, Applied Optics 8, 1471 (1969).

Rensch, D. B., and R. K. Long, Comparative Studies of Extinction and Backscattering by Aerosols, Fog, and Rain at 10.6 μ and 0.63 μ, OSU Electro Science Laboratory, September 1969.

Spencer, D. J. G. C. Denault, and H. H. Takimoto, "Atmospheric Gas Absorption at DF Laser Wavelengths," Applied Optics 12, 2855 (1974).

☆ U. S. GOVERNMENT PRINTING OFFICE: 1977 — 757-001/223